Norwegian University of Life Sciences
Faculty of Science and Technology
Department of Geomatics

Philosophiae Doctor (PhD)
Thesis 2019:56

Environmental monitoring with ground-based interferometric radar systems

Miljøovervåkning med bakkebaserte interferometriske radarsystemer

Rune Gundersen

Environmental Monitoring with Ground-based Interferometric Radar Systems

Miljøovervåkning med bakkebaserte interferometriske radarsystemer

Philosophiae Doctor (PhD) Thesis

Rune Gundersen

Norwegian University of Life Sciences
Faculty of Sciences and Technology
Department of Geomatics

Ås 2019

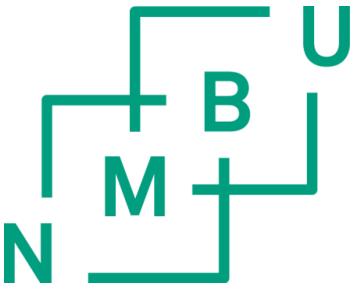

Thesis number 2019:56
ISSN 1894-6402
ISBN 978-82-575-1615-4

Series of dissertations submitted to the Faculty of Science and Technology, Norwegian University of Life Sciences

No. 56

ISSN 1894-6402

The person who says it cannot be done should not interrupt the person doing it.

–Chinese Proverb

Acknowledgements

The work presented in this thesis was carried out in the department of Science and technology at the Norwegian University of Life Sciences and at the company ISPAS AS, Moss, Norway. The Research Council of Norway and ISPAS AS, Moss, Norway gave the financial support for my doctorate. The funding from the Norwegian Research Council was given under their industrial Ph.D. program which aim is to fund and boost research activity in Norwegian companies.

I would like to thank my supervisor professor Cecilie Rolstad Denby at the Norwegian University of Life Sciences and my co-supervisor Richard Norland of ISPAS AS for their support and guidance through my Ph.D.

The campaign measuring Kronebreen glacier at Ny-Ålesund Svalbard was made possible through Svalbard Science Forum, the Norwegian Polar Institute, and Kings Bay AS.

I would also like to thank my colleagues at ISPAS AS for their support and help during the project.

Finally, I thank my family for their continued love, support and patience. Without their support, this work would not have been possible.

Ås, 11 Mai 2019

Rune Gundersen

Table of Contents

Abstract

The need for environmental monitoring is increasing with climate changes and natural resources exploitation, but the monitoring possibilities are also improving with the technological development enabling high spatial and temporal resolution. In this thesis, we address the accuracy and use of interferometric ground-based radar for detecting and monitoring of sub-millimetre surface displacements for geotechnical applications. We have focused on monitoring of rock slope failures, and glacier flow and calving events. We have used two different radar-systems in these two applications. The radar used to monitor rock slopes has a real aperture antenna, while the radar used for glacier flow monitoring has an electronically steered phased-array antenna. The latter makes it possible to scan the surface of the glacier with high temporal and spatial resolution. Both radars are designed and implemented by the radar company ISPAS AS. The radar used for mountain monitoring was developed and installed before this Ph.D.-project was undertaken, but the electronic scanning radar was built during this thesis. The design and development of the radar is not addressed this thesis.

The focus of this work can be divided in two parts; first the analysis of the accuracy and error sources in interferometric ground-based radar systems, and secondly the analysis and processing of the data acquired from measurements with ground-based interferometric radar systems. The measurements analysed in the thesis are from Mount Hegguraksla, Møre og Romsdal, and Kronebreen glacier, Ny-Ålesund. At Mount Hegguraksla, we monitor two unstable mountain crags while at Kronebreen we monitor the 3.5 km wide front of the glacier. The magnitude of the measured displacement is different for the two sites; at Hegguraksla at millimetres per year, while at Kronebreen up to five metres per day. At mount Hegguraksla, we have access to eight years of consecutive data giving long time-series, while at Kronebreen we have two series of 14 hours of continuous data. From previous measurements of Kronebreen, we have access to 92 hours of continuous data. This industrial Ph.D.-project funded by the Norwegian Research Counsel is based on the company ISPAS 12 years' experience with mountain monitoring and five campaigns measuring the Kronebreen glacier at Ny-Ålesund Svalbard.

Measurements in field and laboratory have shown that an interferometric radar system can achieve accuracy comparable to a differential radar system, and that displacement monitoring with sub-millimetre precision is possible with knowledge of the measurement

geometry, the radar hardware, and meteorological data. Computer simulations based on a theoretical radar model were used to validate the measurements. The measurements showed that interference between reflectors resulted in oscillations in the measured displacement. The laboratory experiment showed that in some cases stationary objects could mask the motion of the moving object depending on their mutual size and the measuring frequency. We find that differential interferometry is unaffected by variations in the radio refractivity but vulnerable for inter-reflector interference. We have shown that differential interferometric radar can be used for real-time monitoring of unstable mountain blocks in a costal environment achieving a precision comparable to results achieved with on-site geotechnical instruments e.g. extensometers and tilt meters.

The results from the monitoring of Mount Hegguraksla shows annual cycles in the time series of the measured distances, and these cycles are consistent with data from the geotechnical instruments. Most measurement discontinuities occurred during the winter and were due to snow build-up in the radar reflectors or heavy snowfall. Analysis of the amplitude data showed that the reflections from the radar reflectors are Rayleigh distributed whilst the clutter from the mountains are normally distributed. The eight years of accumulated motion of the two unstable crags are between 1.2 and 6.3 mm.

Measurement results from Kronebreen show that the radar system with an electronically steered antenna can map the flow of a fast-flowing glacier with a high temporal and spatial resolution. The radar system could map the glacier flow five times a minute with a special resolution of 3°. Measurements were made from two locations, at ~6 km and at ~15.5 km from the glacier front, which gave a minimum uniquely observable area of 628 m^2 and 3,927 m^2 respectively. Stable reflection points on the mountains surrounding the glacier were used to correct the measurements for variations in the radio refractivity across the fjord and the uncertainty of the glacier flow is estimated to 1.2% of the measured flow. Calving onsets or rotation of large blocks of ice were detected in the data measured from both locations. The flow-speed of the glacier varied across the glacier with the highest speed in the central part slowing toward the edges. The maximum instantaneous flow recorded was 141 μm/s, or ~12.2 m/day, and are believed to come from a calving event or rotational motion of large blocks of ice. The flow in the intersection between Kronebreen and Kongsvegen and along Colletthøgda was measured to be approximately 0.4 m/day. The accuracy of the flow measurements is estimated to be within 1.3% of the

measured flow. The mean flow of the first 300 m of the glacier varied from 0.4 m/day at the edges to 3 m/day in the central part of the glacier, which gives a total mean glacier flow of approximately 1.7 m/day. Based on the mean flow of the glacier, the estimated area of ice lost in calving is approximately 1.6 km^2/day during the measurements in September month. The study showed that Ny-Ålesund is a well-suited location for a permanent installation of a real-time terrestrial glacier monitoring radar. The project has shown the potential for real-time monitoring of glacier calving, which will be useful for ship traffic and glaciological climate studies.

Sammendrag

Vi vil i fremtiden se et økende behov for miljøovervåkning som en følge av klimaforandringer og utvinning av naturressurser. Samtidig vil den teknologiske utviklingen gi oss sensorer med høyere kapasitet og bedre oppløsning i tid og rom. I denne oppgaven har fokus vært å analysere målenøyaktigheten til bakkebasert interferometrisk radar med hensyn til deteksjon og overvåkning av submillimeter bevegelser for geologisk overvåkning. Vi har gjort målinger og analysert data fra overvåkning av en ustabil fjellside, og vi har gjort målinger av strømningshastighet på en isbre. Til disse målingene har vi brukt to forskjellige radarsystemer. Radaren som er brukt til overvåkning av den ustabile fjellsiden har en antenne med fast åpning, mens radaren brukt til målingene av strømningshastighet på isbreen har en antenne som styres elektronisk. Den elektronisk styrte antennen gjør det mulig å avbilde isbreens overflate med en høy oppløsning i tid og rom. Begge radarene er utviklet av radarfirmaet ISPAS AS. Radaren som er brukt til overvåkning av den ustabile fjellsiden er utviklet og installert før denne oppgaven ble påbegynt, mens radaren som ble brukt til isbremålingene er utviklet i tiden denne oppgaven er gjennomført.

Arbeidet utført i denne oppgaven kan deles i to: Del en er en studie av målegeometri, nøyaktighet og feilkilder i bakkebasert interferometriske radarmålinger. Del to er analyse og prosessering av radardata fra målinger med bakkebasert interferometrisk radar. Måledataene som er analysert i denne oppgaven er fra en ustabil fjellside i Møre og Romsdal, som heter Hegguraksla. Isbreen som vi har målt på er Kronebreen som ligger i nærheten av Ny-Ålesund på Svalbard. På Hegguraksla overvåket vi to ustabile fjellpartier mens på Kronebreen avbildet vi hele fronten av isbreen samt noen kilometer innover isen. Bevegelsen på de to stedene er veldig forskjellig; på Hegguraksla har vi en bevegelse som er på millimeternivå pr. år, mens isstrømmen på Kronebreen er på flere meter pr. dag. Fra Hegguraksla har vi kontinuerlig overvåkningsdata siden mars 2010, hvilket åpner for langtidsanalyse av bevegelsesdata. Fra Kronebreen har vi to tidsserier på ca. 14 timer tilgjengelig for analyse. Fra tidligere målinger på Kronebreen har vi 92 timer med kontinuerlig måledata. Dataanalysen bygger på erfaringer opparbeidet gjennom 12 år med målinger på Hegguraksla og til sammen fem målekampanjer på Kronebreen.

Målinger utført i felt og i laboratoriet viser at et interferometrisk radarsystem kan oppnå samme målenøyaktighet som et differensielt interferometrisk radarsystem, når det

kompenseres for målegeometri, variasjon i radarmaskinvaren og kompenserer for atmosfæriske variasjoner. En numerisk simuleringsmodell av radarsystemet ble utviklet og brukt til å verifisere radarmålingene. Radarmålingene viste at gjensidig påvirkning mellom radarreflektorer førte til amplitudesvingninger på mottatt signal. Laboratoriemålingene viste at bevegelsen til et objekt i noen tilfeller ble maskert av andre nærliggende objekter, avhengig av deres innbyrdes størrelse. Videre viste resultatene at de differensielle målingene var nærmest upåvirket av atmosfæriske variasjoner, men sårbare for interferens mellom radarreflektorene.

Vi har vist at et differensielt interferometrisk radarsystem kan brukes for sanntidsovervåkning av ustabile fjellpartier i kystnære strøk, og oppnå resultater med en nøyaktighet som er sammenlignbar med lokalt plasserte geotekniske instrumenter.

Resultatene fra overvåkningen av Hegguraksla viser årstidssvingninger i avstanden til radarreflektorene. De målte årstidssvingningene er konsistente med resultatene fra de geotekniske instrumentene som viser de samme årstidssvingningene. Flesteparten av driftsavbruddene opptrer i vinterhalvåret og kommer av oppbygning av snø i radarreflektorene og kraftig snøfall gjerne i tilfeller med våt snø. Analyse av amplitudedata fra mottatt radarsignal viser at refleksjonene fra radarreflektorene følger en Rayleigh-fordeling, mens radarrefleksjonene fra fjellet er normalfordelt. Den akkumulerte bevegelsen gjennom åtte år er for de to ustabile fjellpartiene 1,2 mm og 6,3 mm.

Resultater fra målinger på Kronebreen viser at et radarsystem med en elektronisk styrbar antenne er godt egnet til å måle raske forflytninger av isbreen med en høy oppløsning i tid og rom. Den anvendte radaren leverte fem avbildninger av brebevegelsen pr minutt med en romlig oppløsning i side på 3°. Målingene ble utført fra to steder, på ~6,0 km og ~15,5 km fra brefronten, som ga minste romlige oppløsning på henholdsvis 628 m^2 og 3927 m^2. To stabile refleksjonspunkter på fjellene som omgir Kronebreen ble brukt for korreksjon av variasjon i radiorefraktiviteten. Fra begge målesteder observerte og geolokaliserte vi begynnelsen av kalvinger eller rotasjon av store isblokker. Brebevegelsen til Kronebreen varierte med tverravstanden. Størst hastighet ble målt i den sentrale delen av isbreen med avtagende hastighet ut mot kantene. Maksimal målt brebevegelse var 141,0 μm/s eller ~12,2 m/dag. Dette er sannsynligvis starten på en kalving eller rotasjon av store mengder is. Brebevegelsen langs Colletthøgda og i

grenseområdet mot Kongsvegen ble målt til ca. 0,4 m/dag. Usikkerhet i målt bevegelseshastighet ble beregnet til å være ca. 1,2% av bevegelsen til isbreen. Den midlere brebevegelsen til de første 300 m av isbrefronten varierte fra 0,4 m/dag langs kantene, til ca. 3 m/dag i det sentrale området. Dette ga en snitthastighet på ca. 1,7 m/dag for hele den 3,5 km brede isbrefronten. Totalt gir dette et midlere kalvingstap på 1,6 km^2 is pr dag for målingene utført i september. Målingene viste at Ny-Ålesund er et velegnet sted for permanent sanntidsovervåkning av isbreer med bakkebasert radar. Målingene har vist hvilke muligheter som ligger i sanntidsovervåkning av isbreer og resultatene kan være nyttige i klimastudier av isbreer og for båttrafikk i arktiske områder.

1. Introduction

The Earth has experienced several natural climate cycles, which for the past million years has had a cyclic interval of approximately 100,000 years. This cycle is divided in 80-90,000 years of ice age and 10-20,000 years of warming. For the last 250 years, anthropogenic activity has increased, and the natural balance of the cycle is disturbed through excess release of CO_2 to the atmosphere. In the natural cycle, referred to as the Milankovitch cycle, the concentration of CO_2 in the atmosphere lags the heating but due to human activity the CO_2 release now leads the warming. This deviation is believed to be one of the main causes of the temperature increase observed during the last century. Since 1880 the average global temperature has increased with 0.8°C and about two-thirds of this increase has occurred since 1975 [1].

Rockslides can be trigged by high precipitation, erosion, and temperature variation or extreme stresses from earthquakes [2]. In Norway, global warming is leading to increased precipitation and wind, and a higher frequency of extreme weather conditions. It is reasonable to expect that a wetter climate with more frequent events of high precipitation will decrease rock stability. The west coast of Norway is susceptible to rockslides due to the topography with high mountains overlooking deep fjords. Unlike rockslides ending on solid ground beneath the mountain, rockslides ending in fjords have a wider impact area as they may result in flood-waves following the fjord, which can lead to life threatening situations and cause major damage to infrastructure. The Norwegian Water Resource and Energy Directorate (NVE) is the national body responsible for flood and landslide warnings in Norway, and they have identified seven high-risk areas of failure where early warning systems are needed [3]. Since 2006 ISPAS has monitored in one of these areas, Mount Hegguraksla, using a ground-based interferometric radar. In Paper II, we analyse and present the results from these measurements based on data acquired between 2011 and 2018.

Glaciers cover approximately 10% of the surface of the Earth and combined they hold approximately 75% of the Earths fresh water [4]. If the average temperature of the Earth continues to rise it is likely that large quantities of the glaciers will melt and lead to a rise of the global sea level [5] [6] [7]. As a large portion of the habitable part of the Earth is close to the sea, a rise in the global sea level could have a dramatic socio-economic effect.

The worst-case scenario of glacier melting, which includes the Antarctic ice sheet, would lead to approximately 60 m raise in the global sea level. In addition comes the rise in sea level from thermal expansion of the seawater. Monitoring is instrumental for gaining insight into the dynamic of the glaciers and in the mechanism controlling the mass balance of the glacier. There are numerous ways to monitor the ablation, flow, and calving activities of glaciers and studies have been published including visual observations, tracking by satellite-borne sensors, and ground penetrating radar. In Paper III, we present high temporal resolution results from measuring Kronebreen glacier in Ny-Ålesund with ground based radar.

Remote sensing is the art of collecting information about an object without being in physical contact with the object. In its broadest sense, observing an object by your eye is remote sensing. Today, the term remote sensing is often associated with observations made from a distance by active or passive sensors like sonar, radar, lidar, photography, etc. The sensors can be stationary or carried on moving platforms like land-, sea-, air-, or space- vehicles. The sensors all have their advantages and disadvantages, and in the following we are focusing on the use of radar as the information-gathering sensor. The all-weather capability of the radar makes it a versatile sensor well suited for continues operation. A radar is an active sensor, which emits an electromagnetic signal and receives the reflected echo from an object. The temporal and spatial resolution of the radar depends on the physical properties of the sensor and the distance between the sensor and the monitored object or area. For a satellite-borne radar, the repeat cycle of the satellite gives the temporal resolution, while the spatial resolution is given by the size of the radar antenna, orbit elevation, and the operational frequency of the radar. Terrestrial radar has the advantage of shorter radar-target distance, potentially yielding higher spatial resolution, and higher temporal resolution. Satellite-borne radar systems have the advantage of wide area coverage of hundreds of square kilometres, while terrestrial radar systems typically cover a small area of a few square kilometres. Satellite and terrestrial radar systems can complement each other; satellite-borne systems are used for wide area coverage and the high-resolution terrestrial system covers selected areas/objects of special interest. The terrestrial radar offers real-time monitoring capabilities, which is crucial in geophysical monitoring of fast-moving objects or surfaces. For high-precision monitoring interferometry is the preferred measurement technique. Interferometric radar measurements utilising the phase of the received radar signal to detect and track

displacements is an established remote sensing technique in geosciences for measuring surface deformations.

Interferometric radar instruments offer sub millimetre precision in displacement monitoring applications. However, in real-life applications the precision is usually limited by the measurement geometry, variation in the radar hardware and variation in the radio refractivity. Variation in the radio refractivity is the most important factor limiting the precision. The radio refractivity varies with the air humidity, temperature, and pressure. Based on meteorological data the variation in radio refractivity can be estimated and compensated for by using empirical formulas or by measuring the variation in distance to a known fixed point. Both space-borne and ground-based radars provide a powerful tool for weather independent remote sensing of geological events with an ever-improving quality, which opens for a range of new applications.

To avoid range ambiguities in the measured data due to temporal and geometrical decorrelation and variations in radio refractivity a high temporal measurement rate is essential. The temporal resolution of satellite-borne sensors is limited by the orbital pattern or revisit time of the satellite. For ground-based remote sensing systems, the temporal resolution is given by the measurement interval of the sensor. For satellite systems the revisit time spans from days to weeks while ground-based systems can measure up to a few thousand times per second. This is obviously an advantage for the ground-based monitoring system. When it comes to spatial coverage, it is the other way around, the satellite-borne sensor can potentially cover the earth while the ground-based system is bound to a fixed location or area.

Ground-based remote sensing systems can be divided into two categories; object surveillance with staring radars and area surveillance with mapping radars. The mapping systems can be rotational, moving, or stationary. The rotational and moving systems are based on mechanical motion of the antennas, while the stationary system has electronic steering of the antennas' look direction. The temporal resolution of the electronic system is generally higher than the mechanical counterpart. This is because no mechanical motion is involved in the electronic system, only electronic phase shifting which takes no more the a few microseconds. For decades, electronic steered antennas have been used in high-performance military and space radars. The civilian use has been limited due to the cost, however over the last ten years, the availability of integrated microwave circuits has

increased making it possible to develop electronically steered antennas for remote sensing applications. A low-cost high-performance radar system with an electronically steered antenna has been developed during this thesis and the results from the first measurements of glacier flow have been published. We have used a staring radar system and a radar system with an electronic steered antenna for point monitoring. The radar with the electronic steered antenna was used for area mapping.

1.1. Organization of the thesis

Chapter 2 contains an introduction to radar theory and interferometric radar measurements and covers some basic topics of radar data processing and techniques used in the thesis. In chapter 3, we present some results from the measurements that are not discussed in the published papers, while chapter 4 and 5 contain the conclusion and future research directions.

1.2. Experimental measurement studies

Three experimental measurement studies have been conducted; the first is a basic study of interferometric radar measurements looking at the performance, accuracy, and error sources of radar measurements. The second study presents eight years of continuous measurements of an unstable mountain on the western coast of Norway. The third study is a high-temporal and spatial resolution measurement of the Kronebreen glacier Ny-Ålesund, Svalbard. The reason for choosing these two areas was the interesting geophysical phenomena in combination with the availability of data. We have monitored Mount Hegguraksla since 2006 and long-time series of data were available. As a part of the GLACIODYN project NMBU and ISPAS have measured Kronebreen glacier on five occasions, and the Ny-Ålesund research facilities have enabled numerous studies of glaciers in the past.

1.2.1. Assessment of error sources of ground-based interferometric radar (Paper I)

Several effects affect electromagnetic waves and limit the measurement accuracy, and a careful analysis of the setup of the deployed radar system in field is essential to achieve adequate results. Several measurements were conducted both in the field and in the laboratory to assess the factors limiting the accuracy of interferometric measurements. The focus was on measurement geometry, radar hardware and environmental effects on

interferometric and differential interferometric measurements. A theoretical model was implemented to assess deviations between theory and measurements. The results are published in Paper I.

1.2.2. Monitoring of unstable mountain blocks (Paper Ⅱ)

Mount Hegguraksla is in Møre og Romsdal County on the western coast of Norway. Geologist have identified two unstable areas in this mountainside. The unstable areas are located at an elevation of 600 to 800 m above the fjord. A mountain slide is therefore likely to result in a flood wave in the fjord below. Depending on the volume of the mountain slide, it can have catastrophic results on the settlements along the fjord. In 1934, a part of the mountain fell into the fjord and created a wave, which raised to approximately 64 m and followed the fjord in both directions destroying everything in its path and killing about 40 people. In the fall of 2006, ISPAS installed six triangular corner reflectors in the mountainside. Two reflectors are located at the unstable crags and two close to the crags serving as references. The last two reflectors were located on top of the mountain serving as a reference for the four reflectors in the mountainside. Paper II deals with the analysis of eight years of continuous radar monitoring of unstable areas of Mount Hegguraksla. The results are published in Paper II.

1.2.3. Monitoring of glacier calving fronts (Paper Ⅲ)

Kronebreen, 78°53 N, 12°30 E, Ny-Ålesund, Svalbard is a fast-flowing tidewater glacier terminating in Kongsfjorden. Kronebreen is relatively easily accessible using the research facilities in Ny-Ålesund approximately 15 km from the glacier. The ease of access is one of the reasons why it is one of the most studied glaciers at Svalbard. The average flow-speed of the front of Kronebreen is in the order of 1.6 to 3.5 m/day. However, it varies with time of year reaching its maximum in late summer. As a part of the GLACIODYN project NMBU in cooperation with ISPAS have measured Kronebreen glacier yearly from 2007 to 2010 and again in 2017. The front of Kronebreen has retreated more than 1.5 km from the first time we measured Kronebreen in 2007 to the last campaign in 2017. The retreat of Kronebreen is part of a general trend of glacier retreat and if it continues at the current rate glacier melting will be a major contributor to the global sea level rise. Monitoring of calving fronts is of interest for ice dynamic studies. Kronebreen is a tidewater glacier terminating in Kongsfjorden and due to the calving activity measurements close to the front are hazardous. A ground-based radar was therefore located at a safe distance from

the glacier front. The measurements made from 2007 to 2010 were executed with a real-aperture radar, hence only a small part of the glacier was monitored, however with a high temporal resolution. The acquired data gave insight into the glacier flow-speed; in addition, some calving events were detected [8]. In 2017, ISPAS developed a scanning radar with electronically steerable antenna enabling monitoring of the full width of the glacier. In paper III, we analyse and present the first results from a measurement campaign conducted in September 2017.

2. Radar theory, system, and processing

In this chapter, we outline radar theory and processing of radar data of relevance for this thesis.

2.1. Radar theory

The radar theory presented complements the theory outlined in the published papers.

2.1.1. The radar equation

The radar equation for received power is [9]

$$P_R = \frac{P_T G^2 \lambda^2 \sigma}{(4\pi)^3 R^4}, \tag{1}$$

where $\boldsymbol{P_R}$ is the received power at the receiver antenna, $\boldsymbol{P_T}$ is the transmitted power, $\boldsymbol{G}$ is the antenna gain, $\boldsymbol{\lambda}$ is the wavelength of the centre transmitting frequency, $\boldsymbol{\sigma}$ is the radar cross section of the object causing the echo, $\boldsymbol{R}$ is the radar-to-target distance. Note that the received power decreases with the fourth power of the radar-to-target distance.

2.1.2. Range resolution

The radar's ability to distinguish two targets in distance depends on the radars range resolution, $\Delta\boldsymbol{R}$, which is governed by the bandwidth $\boldsymbol{BW}$ of the transmitted radar signal [9]

$$\Delta R = \frac{c_0}{2BW}, \tag{2}$$

where $\boldsymbol{c_0}$ is the speed of light. The range resolution of the radar remains constant regardless of the distance from the radar see Figure 1. However, the area of the range-gates increases with distance. The radar cannot distinguish between two separate objects that fall within the same range-gate. The actual range-resolution depends on the measurement setup. If there is a difference in height between the radar and the object measured, the actual range-resolution must be corrected by a factor given by the vertical angel between the radar and the measured object [10] (p. 49)

$$\Delta R_d = \frac{\Delta R}{cos\,\theta}, \tag{3}$$

where θ is the vertical angle between the radar and the target often referred to as the angel of depression. If the displacement of an object is not radial to the radar, the displacement will be underestimated, and the result must be corrected.

$$\Delta r = \frac{\Delta r}{cos\ \theta_{EL}\ cos\ \theta_{AZ}}, \tag{4}$$

where $\boldsymbol{\theta_{EL}}$ and $\boldsymbol{\theta_{AZ}}$ is the angle between the radial direction of the radar and the true displacement direction in elevation and azimuth respectively.

2.1.3. Cross range resolution

The cross-range or azimuth resolution of the radar is determined by the physical dimension of the antenna $\boldsymbol{L}$ and the distance $\boldsymbol{R}$ between the radar and the target [9]

$$\Delta R_{cr} = \frac{\lambda}{L} R, \tag{5}$$

From Equation 2, we note that for a real aperture antenna the cross-range resolution declines linearly with the distance from the radar.

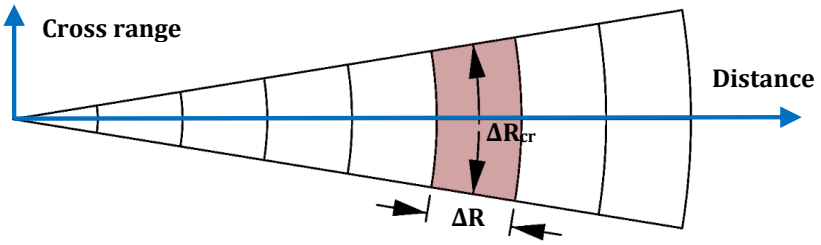

Figure 1. *An illustration of the range and cross-range resolution of the radar system. The concentric arcs indicate the range-resolution; note that the range resolution does not change with distance from the radar. The cross-range resolution, which decreases linearly with distance from the radar, is indicated by the red colored square.*

2.1.4. Radar cross section (RCS)

All objects within the illuminated area of the radar contribute to the backscattered power. To detect and possibly track an object it must have a dominant scatter within the range-gate. When conducting controlled measurements an artificial reflector is often introduced. This is to ensure that the target has higher amplitude than the other contributors within the same range-gate. The radar cross section is a measure of an

objects ability to reflect energy back to the radar. The radar cross section is defined as [11] (p. 11.3)

$$\sigma = \lim_{R\to\infty} 4\pi R^2 \frac{|E_s|^2}{|E_0|^2}, \tag{6}$$

where $\boldsymbol{E_0}$ and $\boldsymbol{E_s}$ are the incident and scattered electric field strength respectively. Analytical expressions exist for some simple shapes including spheres, flat plates, dihedral, and trihedral. Apart from the sphere, the radar cross section of an object depends on the frequency and the angle of the incident field. In our experiment, we use trihedral reflectors. The analytical expression for the maximum RCS of a triangular and square trihedral is [12] (p. 11.3)

$$\sigma_{triangular} = \frac{4\pi a^4}{3\lambda^2}, \tag{7}$$

$$\sigma_{square} = \frac{12\pi a^4}{\lambda^2}, \tag{8}$$

where **a** is the short-side of the triangle. The measured backscatter pattern from the triangular trihedral corner reflector is given in Figure 2.

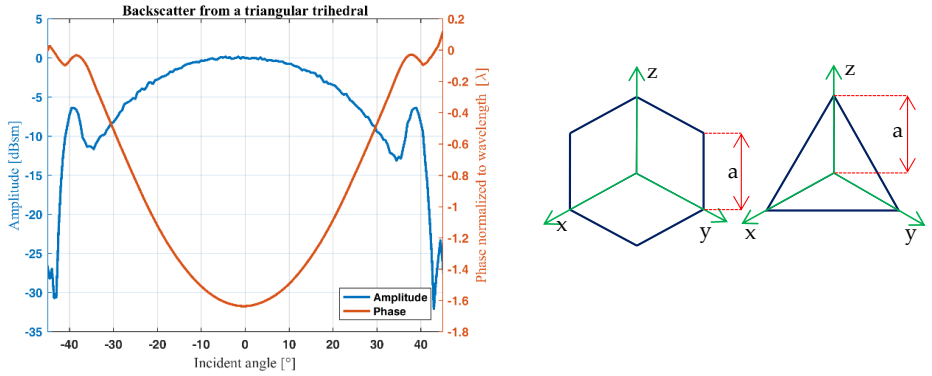

Figure 2. *(a) Measured backscatter of a triangular trihedral corner reflector as a function of the angle of the incident electromagnetic field. The reflection pattern shows that the triangular corner reflector has a backscatter within 3 dB of its maximum value for an angle of the incident field close to ±17°. The phase is normalized with the wavelength as shown with the phase variation of approximately 1.6 λ from ±38° to 0°. (b) Square trihedral corner reflector to the left and a triangular trihedral corner reflector to the right.*

The figure shows that the trihedral corner reflector has a backscatter within 3 dB of its maximum value over an angle of the incident field close to ±17°. The wide opening of the trihedral makes it the natural choice for use in monitoring systems involving movement as the reflector still has a predictable backscatter even when severely misaligned. Note that the phase of the backscattered energy changes with the angle of the incident field.

2.1.5. Multiple scatterers

The area bounded by the range and the cross-range resolution of the radar represents the minimum area resolvable by the radar. All objects within this confined area will contribute to the backscatter. All objects within a range-gate contribute to the backscattered energy, the total RCS of **M** scatterers within a range-gate is [9] (p.26)

$$\sigma = \left| \sum_{n=1}^{M} \sqrt{\sigma_n} e^{\left(\frac{j4\pi R_n}{\lambda}\right)} \right|^2 , \qquad (9)$$

where $\boldsymbol{\sigma_n}$, $\boldsymbol{R_n}$ are the radar cross-section, range, and phase of the $\boldsymbol{n}$-th individual targets. From Equation (9), we see that two equal targets at the same range will give a 6 dB raise in backscattered energy. The summation of the $\boldsymbol{n}$ scatterers within the range-gate will

result in constructive and destructive interference between the scatterers. Equation (9) do not consider shadowing or multiple reflections between the n scatterers. Shadowing will occur whenever one or more of the scattering objects shade the line-of-sight between the radar and scattering objects. This effect is strongly dependent on the aspect angle. Note that the object causing the shadowing effect does not have to be within the range-gate of the object it shades. In addition, we may get multiple reflections between the scatters and diffraction effects from the edges of the scattering object. This results in a complex, aspect angle dependent scattering pattern.

2.1.6. Interferometry

Radar interferometry is a well-established measurement technique used in remote sensing and geodesy. The concept of interferometry for Earth observations was first proposed in 1974 [13]. The method compares two or more measurements to determine if any displacement has occurred between the two measurements. Comparing the phase of the returned radar signals performs this. The method has the potential to measure sub-millimetre changes in distance. Remote sensing for geophysical applications include monitoring of natural hazards like landslides, rockslides, snow avalanches, volcanic eruption, earthquakes, subsidence, glacier flow, etc. Interferometry is applicable for structural monitoring like dams, buildings, bridges, vibration analysis, etc.

Interferometric radar measurements use the phase φ of the reflected electromagnetic wave to derive information from the reflecting object. The phase is a function of the distance from the radar to the target [14]

$$\varphi = \frac{4\pi}{\lambda} R, \tag{10}$$

where φ is the observed relative phase, which is ambiguous in the interval [$-\pi, \pi$]. Due to this ambiguity, the absolute distance R cannot be determined from φ. Hence, the maximum unambiguous range depends on the wavelength of the radar signal and is

$$|\Delta r_{max}| = \frac{\lambda}{4}, \tag{11}$$

Let the complex representation of the received radar signal be $z = ae^{i\varphi}$. If we have two reflections represented by the complex numbers z_1 and z_2, the interferogram is

$$z_1 z_2^* = a_1 a_2 e^{i(\varphi_1 - \varphi_2)} \tag{12}$$

where $\boldsymbol{z_2^*}$ is the complex conjugate of $\boldsymbol{z_2}$. If the two measurements $\boldsymbol{z_1}$ and $\boldsymbol{z_2}$ are of the same target, obtained at different times, any change in phase of the target equals any change in distance between the radar and the target.

The interferometric phase $\boldsymbol{\varphi}$ is the sum of multiple effects

$$\varphi = \varphi_d + \varphi_a + \varphi_n + 2\pi n, \tag{13}$$

where $\boldsymbol{\varphi_d}$ is the phase due to the displacement of the target, $\boldsymbol{\varphi_a}$ is the phase due to atmospheric delays, $\boldsymbol{\varphi_n}$ is the phase noise due to the radar hardware, and $\boldsymbol{2\pi n}$ is the integer phase ambiguity. To unambiguously unwrap the phase of the interferogram the right-hand sum in equation (13) must be less than $\lambda/4$ (Equation (11)). Apart from using a radar with a low internal noise factor, the only parameter we can control to keep the phase shift $\boldsymbol{\varphi}$ below $\lambda/4$ is the time between measurements or the pulse repetition interval (PRI) of the radar. As $\boldsymbol{\varphi_d}$ depends on the target's displacement between measurements, reducing the time between measurements linearly reduce the phase shift. Hence, a high PRI is desirable to avoid phase unwrapping ambiguities and make the radar system more noise tolerant.

2.1.7. Differential interferometry

To reduce the effect of the variations in the radio refractivity we can add a reference reflector. By introducing a reference reflector, we can perform differential interferometric measurements. The general setup for differential measurements is presented in Figure 3.

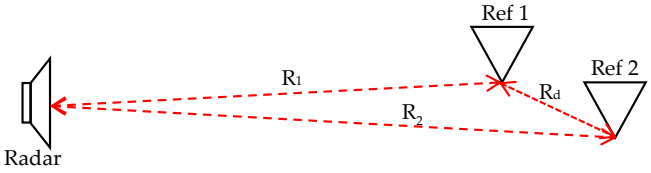

Figure 3. *Illustration of a general arrangement for differential interferometric radar measurements.*

The variation in path-length between the radar and the reflector due to radio refractivity, can be reduced by correlating the measured motion of the two reflectors. This reduces the variation in radio refractivity to the path between the two reflectors R_d. The differential

phase between two objects, R_1 and R_2, or between two measurements of the same object is

$$\varphi = \frac{4\pi}{\lambda}(\varphi_{R2} - \varphi_{R1}) = 2k\Delta\varphi, \tag{14}$$

where $\boldsymbol{\Delta\varphi} = \varphi_{R2} - \varphi_{R1}$.

2.1.8. Signal to noise

The signal to noise ratio is defined as the relation between the received power and noise. The noise consists of environmental noise and system noise, which are independent of each other. The environmental noise is everything affecting the radar signal between the transmitting and receiving antennas. Examples of environmental noise are atmosphere, rain, snow etc. System noise is the thermal noise of the radar system.

An illustration of the signal and noise problem is shown in Figure 4. The noise, ***N***, is assumed to have a complex circular Gaussian distribution and is indicated by the red circle. ***Y*** is the actual backscatter, while ***A*** is the measured backscatter corrupted by the noise vector ***N***. The measured angle $\boldsymbol{\phi_A}$ differs from the actual angle by the noise angle. The noise is composed of variation in the clutter within the range-gate, variations in the refractivity, thermal noise, and instrument noise.

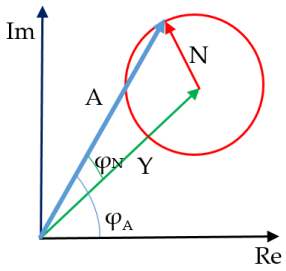

Figure 4. *Phasor plot illustrating the amplitude and phase contribution.* ***A*** *is the amplitude of the measured backscatter from one range-gate.* ***N*** *is the sum of the noise and* ***Y*** *the actual backscatter from the reflector.* $\boldsymbol{\phi_A}$ *is the measured angle and* $\boldsymbol{\phi_N}$ *the angle of the noise contribution. The red circle illustrates the circular sample space of the noise.*

By using radar reflectors, we increase the ratio between vector ***Y*** and ***N,*** hence reducing the influence the noise has on the phase of the backscatter. If the ratio ***Y:N*** decreases to a level at which the noise is larger than the signal, i.e. the noise space covers the origin, we

will have severe problems unwrapping the phase, since the amplitude A will randomly move from quadrant to quadrant.

2.1.9. Coherence

The amplitude stability of the reflection from an object can be used as a selection criterion for choosing points to track in the radar scene. The stability of reflection points in the interferogram can be viewed as a quality measure of the reflection. Interferograms are calculated per pixel for all data images pairs (Equation (12)). The temporal stability or coherence of the amplitude is used as the selection criterion. The coherency is estimated as a moving average of ***n*** observations per pixel as [15]

$$|\gamma| = \left| \frac{\sum_{i=1}^{n}(z_1 z_2^*)}{\sqrt{\sum_{i=1}^{n}|z_1|^2 \sum_{i=1}^{n}|z_2|^2}} \right|. \quad (15)$$

Only the pixels with a coherence above a cut-off value are used and their phase is tracked, and the displacement is cumulatively added image-by-image. Figure 5 shows a coherence plot from the measurements in Ny-Ålesund of the Kronebreen glacier.

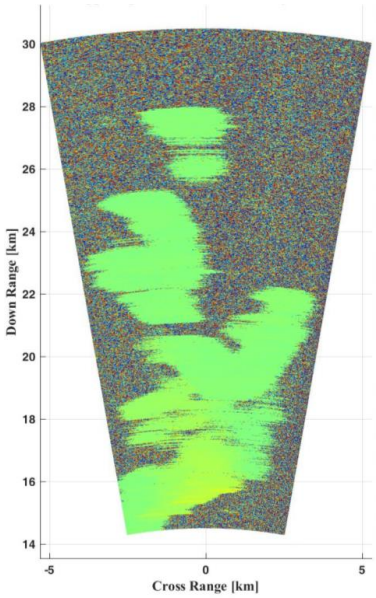

Figure 5. *Interferogram showing the wrapped phase of radar measurements from Kronebreen. The points with stable reflections are the continuous yellowish and greenish areas. The speckled areas are reflections from noisy points, which are temporally unstable. In the central part in the front, is the glacier and from 18 km, are stable reflections from the three mountains Garwoodtoppen, Pretender, and Dronningfjella.*

When the Signal-to-Noise Ratio (SNR) is high, the stability of the backscatter can be estimated with a method introduced by Ferratti et al. [16], originally intended as a way of identifying stable permanent scatterers in Synthetic Aperture Radar (SAR) data scenes. This is a measure for the phase stability called the dispersion index, defined as

$$D_A = \frac{\sigma_A}{m_A} = \frac{1}{2\overline{SNR}}, \tag{16}$$

where $\boldsymbol{m_A}$ is the mean value of the backscatter and $\boldsymbol{\sigma_A}$ is the standard deviation of the backscatter. This method is reported to give reliable results for high SNR ratios, but without specifying what a high SNR is. The method is reported in [9–11] to give stable results with a threshold value typically around 0.25. Some of the shortcomings of the method like its tendency to overestimate the stability of the phase are pointed out in Appendix B in [12].

2.1.10. Range-shift of range data

The amplitude of a radar echo, after processing, follows a cardinal sine-pattern and unless the reflecting object is centred in its range-gate the amplitude will vary with the object's location within the range-gate. This may result in a maximum of approximately -3.8 dB loss of backscattered energy due to the spill over to the neighbouring range-gate (see section 2.3.1). This can be corrected by applying the shift property of the Fourier transform, to shift the received data to the centre of the range-gate [17, 18]

$$\mathcal{F}\{g(t-a)\} = \int_{-\infty}^{\infty} g(t-a)e^{-i2\pi ft}\,dt = e^{-i2\pi ft}G(f) \qquad (17)$$

This gives us the maximum displacement span within the range gate per reflection. An example of range shifting of a reflected radar signal is given in Figure 6.

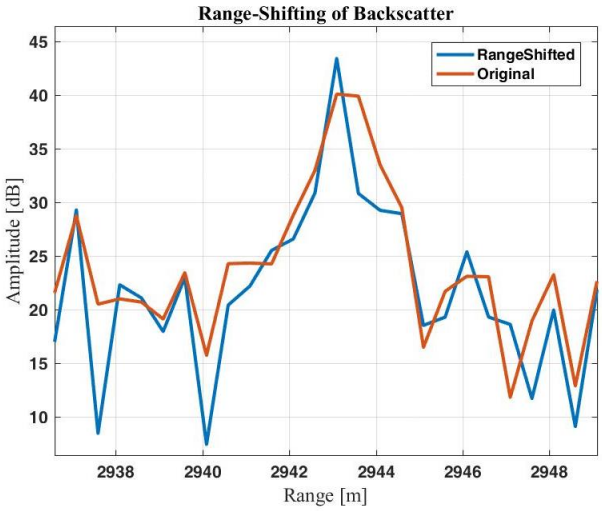

Figure 6. *Maximizing the backscattered energy by time-shifting the received signal. The signals shown are from measurements of reflector 2 at Site 2 at Mount Hegguraksla. The effect of rang-shifting the received signal to the centre of the range gate results in an increase in amplitude of almost 2.5 dB.*

2.1.11. Doppler Velocity

It is a well-known that a moving object alters the frequency of the electromagnetic wave by a frequency equal to the relative motion of the object i.e. the Doppler effect. The Doppler frequency f_D is:

$$f_D = \frac{2v}{\lambda}, \tag{18}$$

where v is the radial speed of the object. The maximum unambiguous Doppler velocity is

$$v_{max} = \frac{c_0}{4\ PRI\ f_0} = \frac{\lambda}{4\ PRI}, \tag{19}$$

where PRI is the Pulse Repetition Interval. By processing several measurements, assuming they are coherent, we can form a time series from the range-gates. By processing this time series, the phase variation of each range-gate can be tracked and the corresponding Doppler velocity per range-gate calculated. This gives us a Range-Doppler map of the measurement. This is used for instance in weather radars. The Doppler velocity is calculated from the change in the phase of the signal from sweep to sweep:

$$v_D = \frac{\Delta\varphi}{2\ PRI} \cdot \frac{\lambda}{2\pi} \tag{20}$$

The number of points, M, in the Fast Fourier Transform (FFT) of the Doppler-speed gives the velocity resolution.

$$\Delta v = \frac{2v_{max}}{M}, \tag{21}$$

2.2. Radar system

In this section, we give a brief description of the radars used in the experiments. We have used three different radars in the outdoor experiments all Frequency Modulated Continues Wave (FMCW) radars. The laboratory measurements were made with a vector network analyser (VNA) in stepped frequency mode.

2.2.1. Frequency modulated continuous wave (FMCW) radar

A FMCW-radar transmits a continuous electromagnetic wave. The modulation signal used is typically a linear frequency modulation with modulation time T_{sweep}. In a FMCW-radar, the frequency is changed as a function of time, where the difference in frequency between

the transmitted and the received signal is directly proportional to the distance of the target.

The time it takes for the electromagnetic wave to travel from the radar to the target and back is

$$\tau = \frac{2R}{c_0}. \tag{22}$$

The frequency difference between the transmitted and the received signal is referred to as the beat frequency, ***Δf***, see Figure 7.

$$\Delta f = \frac{(f_{max} - f_{min})}{T_{sweep}} \cdot \tau\,, \tag{23}$$

where f_{min} is the minimum frequency of the transmitted signal, f_{max} is the maximum frequency of the transmitted signal and T_{sweep} is the sweep time of the modulating signal. Substituting Equation *(22)* into Equation (23) the beat frequency becomes

$$\Delta f = \frac{BW}{T_{sweep}} \cdot \frac{2R}{c_0}. \tag{24}$$

This is the time-range relation for a FMCW-radar. An illustration of the FMCW signal is shown in Figure 7.

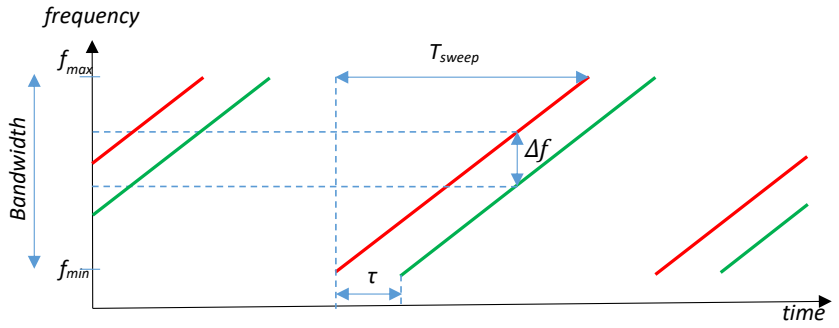

Figure 7. *Time-frequency illustration of the relationship between the transmitted signal (red line) and received signal (green line) in a FMCW radar.* ***τ*** *is the travel time of the echo, see Equation (1), and* ***Δf*** *is the beat frequency, see Equation (2) and (3).* ***T_{sweep}*** *is the sweep time of the modulation signal.*

2.2.2. Mathematical description of the radar system

For a target at a given range, an echo is received with a time delay $\boldsymbol{\tau}$ equal to the two-way propagation delay. The received signal is down converted with the transmitted signal. This transforms the time delay $\boldsymbol{\tau}$ to a constant frequency offset $\boldsymbol{\Delta f}$ unique for a given distance. The demodulated signal is low-pass filtered leaving only the difference part of the down converted signal. We use an I/Q-demodulator for de-ramping. The transmitted frequency chirp ***u(t)*** is given by:

$$u(t) = A_u \cos \varphi(t) = A_u \, cos(2\pi f_0 t + \alpha t^2 + \varphi_0) \tag{25}$$

where $\boldsymbol{A_u}$ is the amplitude of the transmitted signal, $\boldsymbol{f_0}$ is the centre frequency of the carrier and $\boldsymbol{\alpha}$ is the ramp rate of the modulating signal, $\alpha = \frac{BW}{T_{sweep}}$ and $\boldsymbol{\varphi_0}$ is the initial phase of the signal. The instantaneous frequency of the transmitted signal is:

$$f_{Tx}(t) = \frac{1}{2\pi}\frac{d}{dt}\varphi(t) = f_0 + \alpha t \tag{26}$$

The received signal ***z(t)*** from an echo located at a distance $\boldsymbol{R}$ is given by:

$$z(t) = A_z cos(\varphi(t - \tau) + \varphi_0) \tag{27}$$

where $\boldsymbol{\tau}$ is the propagation delay of the echo given by $\tau = 2R/c$. The received signal can then be written as:

$$z(t) = \; A_z cos(2\pi f_0 (t - \tau) + \alpha (t - \tau)^2 + \varphi_0) \tag{28}$$

where $\boldsymbol{A_z}$ is the amplitude of the received signal. The instantaneous frequency of the received signal is:

$$f_{Rx}(t - \tau) = \frac{1}{2\pi}\frac{d}{dt}\varphi(t - \tau) = f_o + \alpha(t - \tau) \tag{29}$$

The mixer multiplies the echo with the transmitted signal producing sum and difference frequencies. This is mathematically equal to multiplying the received signal with the transmitted chirp in-phase.

As the sum of the frequencies is twice the carrier frequency of the radar, it is suppressed, and we only deal with the difference frequencies. The down converted signal ***s(t)*** is:

$$s(t) = A_s cos[\varphi(t) - \varphi(t - \tau)] = A_s cos(2\pi\alpha\tau t + 2\pi f_0 \tau - \pi\alpha\tau^2 + \varphi_0) \tag{30}$$

The I/Q-demodulator consists of two down mixers shifted 90° giving in-phase (I) and quadrature-phase (Q) components of the received signal ***s(t)***.

$$I(t) = A_i cos(2\pi\alpha\tau t + 2\pi f_0 \tau - \pi\alpha\tau^2 + \varphi_0) \quad (31)$$

$$Q(t) = A_q sin(2\pi\alpha\tau t + 2\pi f_0 \tau - \pi\alpha\tau^2 + \varphi_0) \quad (32)$$

The beat frequency is obtained by differentiating:

$$f_{beat}(t) = \alpha\tau = \frac{BW}{T_{sweep}} \cdot \frac{2R}{c_0} \quad \text{[Hz]} \quad (33)$$

The beat frequency is dependent on the ramp rate of the modulating signal and is linearly dependent to the propagation delay. This result is valid when the echoes come from stationary reflection points.

2.2.3. Radar hardware

A FMCW radar transmits and receives simultaneously hence, it usually has separate transmit and receive antennas. A schematic view of the radar is presented in Figure 8.

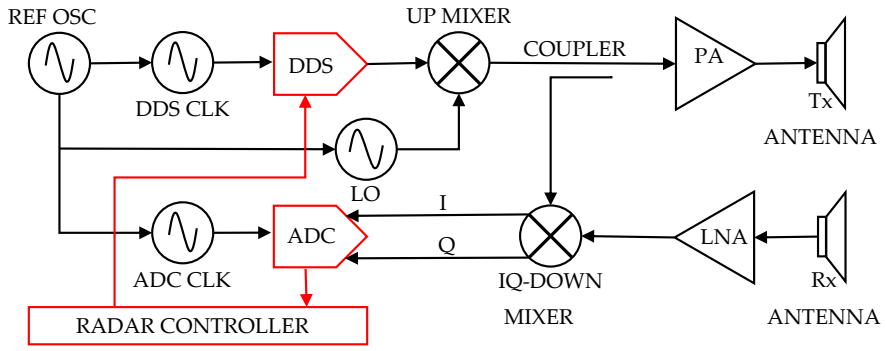

Figure 8. *Schematic view of the radar hardware. A linear frequency-sweep is generated by the Direct Digital Synthesizer (DDS) and up-converted (UP MIXER) by a high-frequency signal generated by the local oscillator (LO). The resulting signal is amplified and fed to the transmitting antenna (Tx). The signal intercepted by the receiving antenna (Rx) is amplified by a low noise amplifier (LNA) and down converted (IQ-DOWN MIXER) with a copy of the transmitted signal obtained via a coupler (COUPLER). The output from the IQ-demodulator is connected to a dual channel Analog-to-Digital Converter (ADC). For coherent operation of the DDS clock, the LO reference, and ADC clock are all referenced to the same reference*

oscillator (REF OSC). The radar controller programs the DDS, triggers the frequency sweeps, and collects the data acquired by the ADC.

A comparison of the key parameters of the radars used in the experiments is given in Table 1.

Table 1. *Summary of key radar parameters for the instruments used in the experiments.*

FMCW Radar Parameters	**Radar 1**	**Radar 2**	**Radar 3**
Centre frequency, fc [GHz]	5.76	9.65	15.75
Maximum bandwidth, BW [MHz]	150	150	300
Maximum range resolution, ΔR [m]	1.0	1.0	0.5
Maximum pulse repetition frequency, PRF [Hz]	1	1	2000
Wave length, λ [mm]	52.1	31.1	19.0
Antenna gain [dB]	16/20	25	30

2.2.4. Radar development, Hegguraksla

The first measurements of the unstable crags at mount Hegguraksla were conducted in October 2003. These measurements were made with a stepped-frequency waveform radar (SFWR) against a flat plate reflector provisional located on the lower crag, see Figure 9. This is the area referred to as Site 1 in Paper II.

Figure 9. *Picture from Hegguraksla Site 1 overlooking the fjord Tafjord approximaly 3 km from the radar in Fjørå.*

The data acquisition time of the SFWR was several minutes. The analysis of the acquired data showed this to be too slow as the variation in radio refractivity leads to decorrelation. In August 2004 the SFWR was replaced by a first generation FMCW radar with a sub-second data acquisition time. The flat plate was replaced by dihedral radar reflectors which was firmly mounted in the mountainside see Figure 10.

(a) (b)

Figure 10. *Dihedral radar reflectors mounted at Hegguraksla Site 1 August 2004. (a) shows the reference reflector and (b) shows the main reflector on the crag.*

In 2006, triangular trihedral reflectors replaced the dihedral reflectors, as the dihedrals did not survive the winter between 2005 and 2006. Triangular trihedrals were selected, as their alignment with the radar direction is less critical than for the dihedral reflectors. The radar was upgraded to the second generation FMCW radar and in 2010; the radar was upgraded to the third generation FMCW radar, which is the current version of the radar system.

(a) (b)

Figure 11. *Trihedral corner reflectors at Hegguraksla Site 1 after the 2006 upgrade. (a) shows the reference reflector and (b) shows the main reflector mounted on the foundation for the sattellite reflector on the crag.*

2.2.5. Radar development, Kronebreen

The first measurements of Kronebreen was made in September 2007 from Pynten with a real aperture FMCW radar, see Figure 12.

Figure 12. *Picture from Pynten, Ny-Ålesund, Svalbard, where the first measurements of the Kronebreen glacier were made in September 2007, at the time approximately 4 km from the front of the glacier. Photograph courtesy of ISPAS AS.*

In the 2008 experiment the same FMCW radar was used but this time with two receiving antennas i.e. forming an interferometer, see Figure 13. This made it possible to detect whether an event happened left or right of the antenna boresight.

Figure 13. *Picture from the 2008 measurements of Kronebreen from Pynten. To the left is the transmitting antenna and to the right are the two receiving antennas forming the interferometer. Photograph courtesy of ISPAS AS.*

In the 2009 experiment the same FMCW radar was used but this time the measurements were made from Ny-Ålesund, at the time approximately 14 km from the front of the glacier, see Figure 14.

Figure 14. *Picture showing the transmitting and receiving antennas mounted on the balcony on Kings Bay's service building in Ny-Ålesund in 2009. Photograph courtesy of ISPAS AS.*

The 2010 experiment was pretty much like the 2008 experiment except this time four receiving antennas were used to form the interferometer, see Figure 15.

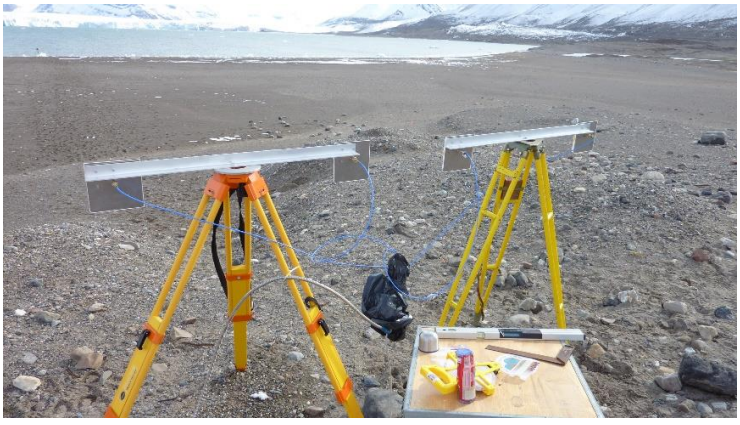

Figure 15. *Picture showing the four receiving antennas on tripods at Pynten in 2010. Photograph courtesy of ISPAS AS.*

In 2017, the measurements were made with a radar with an electronic steerable antenna enabling mapping of the glacier. This time measurements were made both from Pynten and Ny-Ålesund.

(a) (b)

Figure 16. *Pictures from September 2017 showing the radar on site at Pynten (a) and Ny-Ålesund (b). Photograph courtesy of ISPAS AS.*

From the measurements 2009 to the measurements 2017 the front of Kronebreen has retreated more than 1.5 km see Figure 17.

(a) (b)

Figure 17. *The two pictures of Kronebreen glacier taken eight years apart (a) is from 2008 and (b) is from 2017 clearly shows how the front of the glacier has retreated. The orange line indicates the location of the glacier front in 2008. Photograph courtesy of ISPAS AS.*

2.2.6. Field and laboratory measurements

To verify the accuracy and precision of the measurements several controlled measurements were made in field and in laboratory. Both range and cross-range measurements were made, see Figure 18a and b. The down-range measurements are presented in Paper I. Several antenna constellations were tested in the field including two and four receiving antennas, and mechanical rotation of a real aperture antenna. These cross-range measurements were all made before the development of the electronically steered antenna started. After the electronically steered antenna was completed the other

methods were abandoned as the performance of the electronically steered antenna proved to be superior when it comes to temporal resolution.

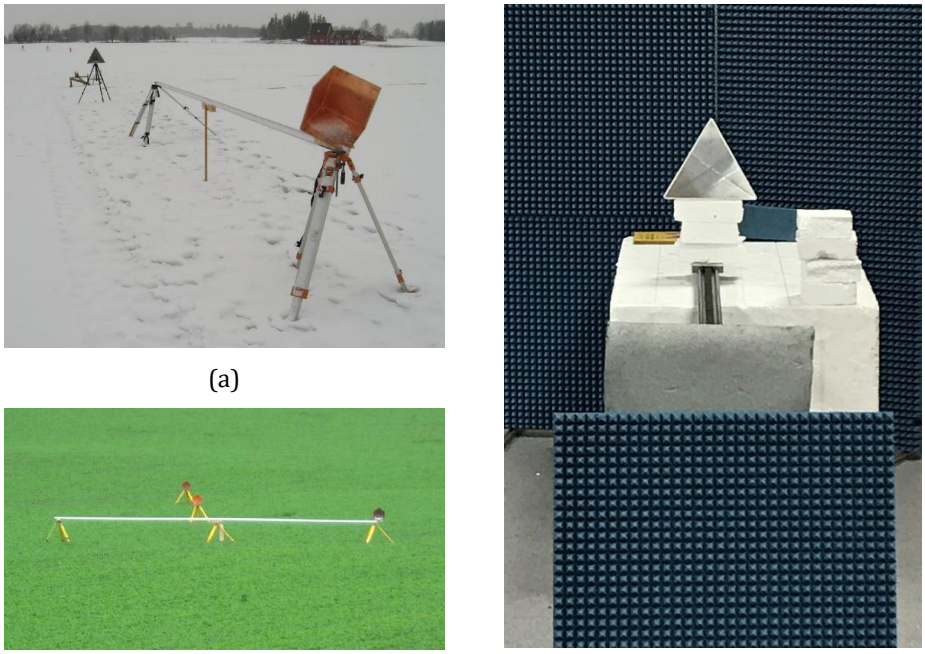

(a) (b) (c)

Figure 18. *(a) Down-range measurements, (b) cross-range measurements, and (c) laboratory measurements.*

2.3. Radar data processing

2.3.1. Radar signal processing

As described in section 2.2.2 Equation (33) the received radar signal is composed of frequencies between f_{min} and f_{max} where the beat frequency is equal to the distance between the radar and the reflecting object. The received radar signal is sampled at discrete time intervals t_{sample}. The sampled radar signal consists of a sequence of N complex numbers $x_0, x_1, \dots, x_{N-1}$ where N = T_{sweep}/t_{sample}. The sampled sequence is transformed to an N-periodic sequence of complex numbers $X_0, X_1, \dots, X_{N-1}$ by a Discrete Fourier Transform (DFT)

$$X_k = \sum_{n=0}^{N-1} x_n e^{-j2\pi\frac{kn}{N}} = \sum_{n=0}^{N-1} x_n \left[cos\left(2\pi\frac{kn}{N}\right) - jsin\left(2\pi\frac{kn}{N}\right)\right], \qquad (34)$$

The minimum distance between two targets is given by the range resolution of the radar, Equation (2). Let τ_{min} be the minimum resolvable time difference between two radar echoes at distance R_1 and R_2

$$\tau_{min} = \frac{2(R_2 - R_1)}{c_0}, \tag{35}$$

Noting the R_2-R_1 = ΔR and by combining Equation (35) and Equation (2) we get

$$\tau_{min} = \frac{2\left(\frac{c_0}{2BW}\right)}{c_0} = \frac{1}{BW}, \tag{36}$$

Each range-gate corresponds to a time span from $-\tau_{min}/2$ to $\tau_{min}/2$ centred around τ. This may be viewed as a series of ***N*** rectangular windows ranging from R_{min} to R_{max}. The Fourier transform of a rectangular function is a *sinc* function with its maximum in the centre of the range gate and the first null in the centre of the neighbouring range gates as shown in Figure 19.

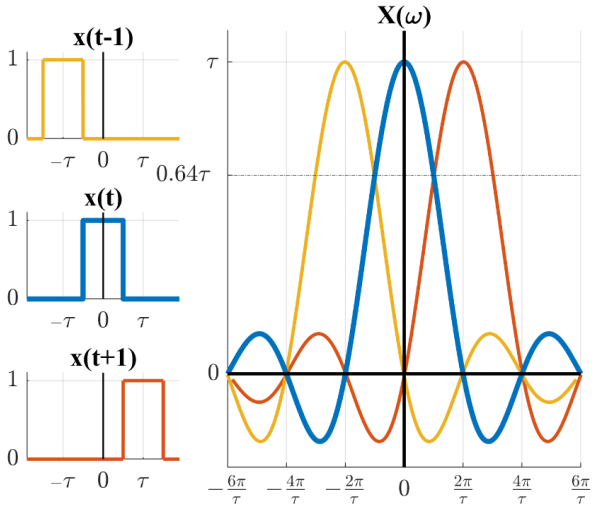

Figure 19. *An illustration of the transformation from the time-domain to the frequency-domain. The three lefthand figures illustrate the time intervalls equalling the range-gate resolution, t-1, t, and t+1. The righthand figure illustrates the range-gate resolution after the Fourier transformation and how the energy is distributed. The crossover between adjecent range-gates occurs at 0.64 times the maximum amplitue of the range-gate.*

The crossover point between two adjacent range gates occurs at 0.64 times the maximum amplitude of the range-gate, which equals -3.88 dB.

2.3.2. Radio refractivity

The variation in path length experienced by an electromagnetic wave propagating through the atmosphere is [19]:

$$L_{atm} = \int_{s} (n-1)ds. \tag{37}$$

where ***s*** is the path through the atmosphere and ***n*** is the refractive index. Since ***n*** is close to unity, it is usually used in its scaled-up version

$$N = (n-1) \times 10^6. \tag{38}$$

The change in the interferometric phase is:

$$\varphi_{atm} = 2k\Delta ns, \tag{39}$$

where $\boldsymbol{k}$ is the wave number and $\boldsymbol{\Delta n}$ is the change in the refractive index. $\boldsymbol{N}$ can be estimated by [20]:

$$N = 77.6890\frac{P}{T} + 71.2952\frac{P_w}{T} + 3.75463 \times 10^5\frac{P_w}{T^2}, \quad (40)$$

where $\boldsymbol{P}$ is the pressure in mbar, $\boldsymbol{T}$ the ambient temperature in Kelvin and $\boldsymbol{P_w}$ the partial water vapour pressure in mbar.

The partial water vapour pressure can be estimated from the relative humidity, $\boldsymbol{RH}$, by the relation

$$P_w = RH\left(\frac{e_s}{100.0}\right), \quad (41)$$

where $\boldsymbol{e_s}$ is the saturation water pressure and is only a function of the temperature, in degrees Celsius, given by the relation [18]

$$e_s = 6.1121 \times e^{\left(\frac{17.502 \cdot T}{240.97+T}\right)}. \quad (42)$$

A temperature lapse rate of -6.5°C per km height was used to compensate for elevation in accordance to ISO 2533:1975 [21]. The height-induced change in pressure was calculated using

$$p = p_0\left((1 - 0.0065\left(\frac{h}{T_0}\right)\right)^{5.2561}, \quad (43)$$

where $\boldsymbol{h}$ is the height, $\boldsymbol{p_0}$ and $\boldsymbol{T_0}$ are the pressure and temperature at sea level respectively. The unit of $\boldsymbol{T_0}$ is Kelvin, the height is in meters, and $\boldsymbol{p}$ is in [hPa].

The range $\boldsymbol{R}$ is given by

$$R = \frac{T_0 \cdot c_0}{2 \cdot n(\vec{r},\ t)}, \quad (44)$$

$\boldsymbol{c_0}$ is the speed of light in vacuum; $\boldsymbol{T_0}$ is the time of travel of the electromagnetic wave from the radar to the reflector and back. $n(\vec{r},\ t)$ is the spatial and temporal index of refraction. The distance to a reflector is thus varying as a function of the index of refraction. The variation of $\boldsymbol{n}$ can be calculated from measurements of the phase of the carrier. The relation is given by:

$$\Delta\varphi = \frac{4\pi \cdot R}{\lambda}\,\Delta n. \tag{45}$$

Combining equation (45) and equation (38) gives us the variation of the refractivity ***ΔN***

$$\Delta N = N_0 - \left(\frac{\Delta\varphi \cdot \lambda}{4\pi \cdot R} - 1.0\right) \cdot 10^6, \tag{46}$$

where ***N₀*** is a reference refractivity, typically the value of the first measurement. The variation in radio refractivity as a function of air temperature and humidity is shown in Figure 20.

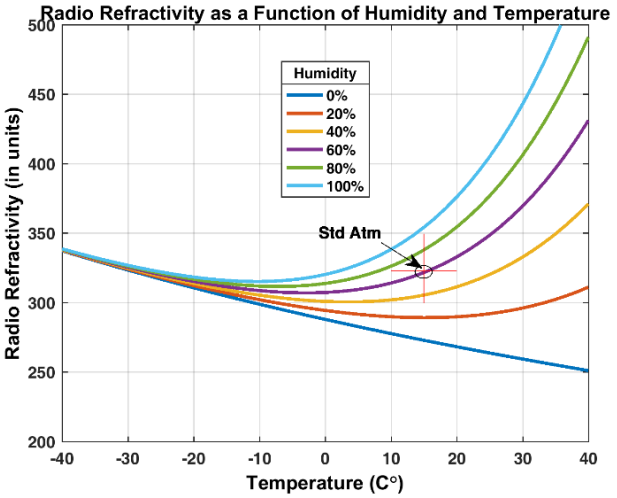

Figure 20. Variation in refractive index as a function of air temperature and relative humidity. The pressure is kept constant at 1013.25 mbar. The International Standard Atmosphere according to ISO 2314 is marked with a red cross-hair (The ISO 1314 Standard Atmosphere is defined as Temperature = 15°C, Humidity = 60% and Pressure = 1013.25 mbar at Sea Level).

3. Discussion of selected topics in the studies

3.1. Possible thermal expansion of mounting beams

The monitoring data from the eight years of monitoring Mount Hegguraksla, presented in Paper II, showed oscillations with an annual cycle. Parts of this motion are believed to be caused by thermal expansion of the mounting beams used to fasten the radar reflector to the mountain. Figure 21 shows pictures of the reference reflectors on Site 1 and Site 3 at Mount Hegguraksla.

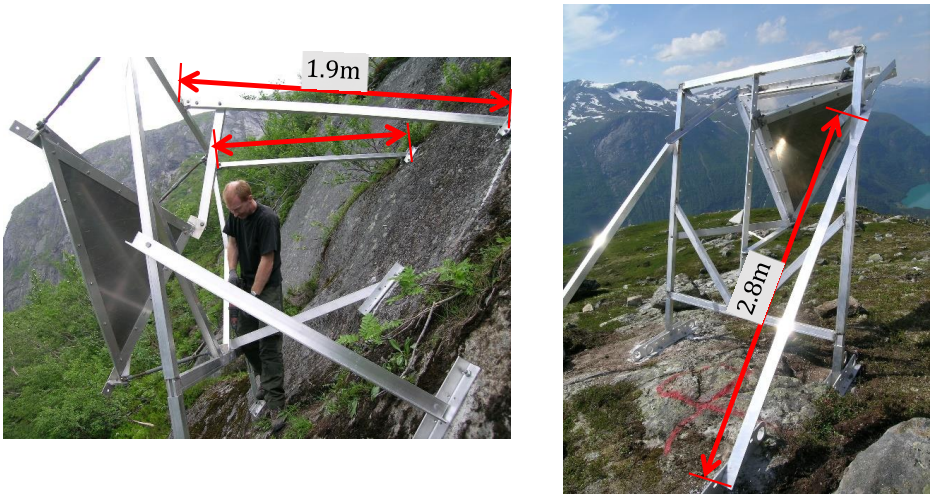

(a) (b)

Figure 21. *Pictures showing the reference reflectors on Site 1 (a) and Site 3 (b) at Mount Hegguraksla.*

All the reflectors are fixed to the mountain with aluminium beams, where some of these beams are more than 2 meters long. Variation in length of the beams will directly alter the measured distance since the beams are radially in line with the radar-reflector path. The thermal expansion is the fractional change in length per degree of temperature change. The thermal expansion for aluminium is taken to be 23.1 μm/°C. The lengths of all the reflector beams are listed in Table 2.

Table 2. *Length of reflector support beams.*

Site	Reflector number	Length of support beams [m]	Mean Temperature T_{mean} [°C]	Maximum Temperature T_{max} [°C]	Minimum Temperature T_{min} [°C]	Linear Expansion ΔL [mm]
Site 1	1	0.1	2.7	24.5	-24.6	0.11
	2	1.9	2.6	24.4	-24.7	2.15
Site 2	3	1.6	2.1	23.9	-25.2	1.81
	4	2.5	2.0	23.8	-25.3	2.84
Site 3	5	3.0	1.3	23.1	-26.0	3.40
	6	2.8	1.0	22.8	-26.3	3.18

The annual variation calculated from the seven-year median temperature for a one-metre aluminium beam is presented in Figure 22a, and it shows a variation of 0.35 mm. The annual variation due to thermal expansion between the reflectors at Site 1 is presented in Figure 22b.

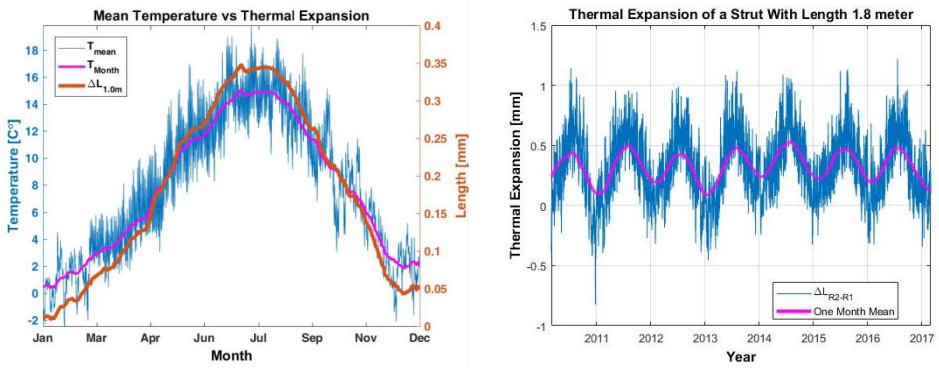

(a) (b)

Figure 22. *Panel (a) shows the annual thermal expansion for an aluminium beam of length 1 m calculated from the median temperature for seven years. Panel (b) shows the variations between the two reflectors at Site 1 caused by thermal expansion of the aluminium beams by which they are mounted to the mountain.*

The variation caused by the thermal expansion for all three sites is shown in Figure 23. Since the calculations of the thermal expansion is based on the same temperature data as used to estimate the variation in radio refractivity, they correlate with the differential measurements.

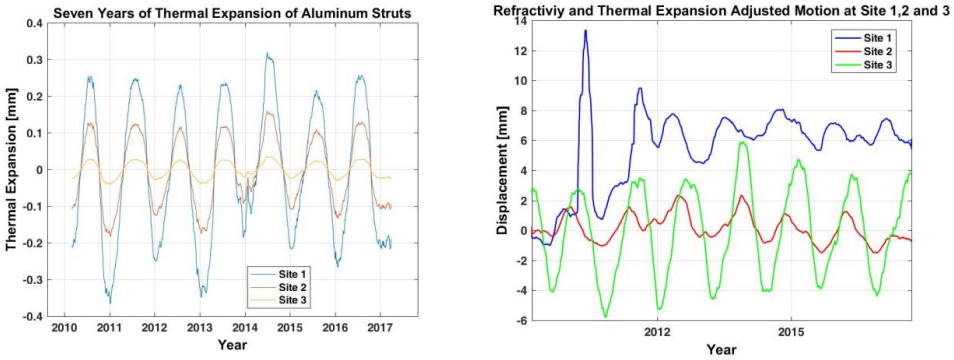

(a) (b)

Figure 23. *Panel (a) shows the variation in distance due to thermal expansion of the mounting beams. Panel (b) shows the calculated displacement of the reflectors at Mount Hegguraksla after compensating the measurements by the estimated variation due to thermal expansion of the mounting beams.*

As we see, the thermal expansion of the aluminium beams can explain part of the cyclic motion observed in the measurements.

3.2. Range shift of radar data

The results from the towed reflector experiment showed that the amplitude of the backscatter fell from its maximum value in the centre of the range-gate with 3.9 dB to the end of the range-gate. In the measurements from Mount Hegguraksla, the backscatter from each of the six reflectors were individually range-shifted to the centre of their respective range-gate, using the average of the first few thousand measurements as reference to centre the reflection in the range-gate. In a FMCW radar, this implies a linearly increasing frequency shift according to the bandwidth and the range for which the shift is intended. By applying this for all the reflectors, we maximized the backscatter-to-clutter ratio for all the reflectors, thus maximizing our ability to track the movement of the reflectors. The same effect could have been achieved by shifting each reflector individually back or forth until it was perfectly aligned in the centre of the range-gate. The range shifts used for the measurements presented in Paper II are listed in Table 3.

Table 3. *The range-shift values used to centre the reflectors in the range gates. Since radar measurements are two-way measurements, the actual change in distance is half the value given in the table.*

Site	Reflector	Range Shift, [m]	t_{shift}, [ns]
1	1	-0.205	1.366
	2	-0.110	0.733
2	3	0.075	0.500
	4	0.240	1.600
3	5	-0.300	2.000
	6	-0.080	0.533

3.3. Doppler processing

There are several ways of processing sampled radar data to obtain the displacement or velocity. In the published papers, the data were processed by interferometry. Another way of processing is by Doppler-processing as described in section 2.1.11. Doppler-processed data from Paper I and Paper II is presented below and a short discussion on the velocity distribution.

3.3.1. Doppler processing of the towed reflector

The results of the Doppler processed measurements from the reflector towing experiment is given in Figure 24.

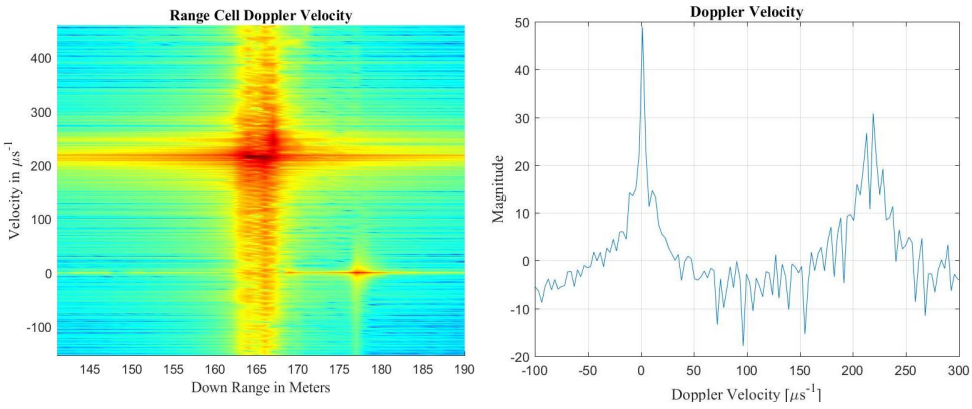

(a) (b)

Figure 24. *Doppler velocity as a function of distance. Panel (a) shows the calculated Doppler velocity of the towed reflector. Panel (b) shows the maximum value recorded for all ranges.*

The calculated Doppler velocity is between 215 and 223 µm/s, which corresponds well with the differential interferometric calculated velocity of 211 µm/s. The Doppler processing was done with an FFT-size of 16k giving a maximum unambiguous velocity of v_{max} of 12.4 mm/s and a velocity resolution of Δv = 1.54 µm/s.

3.3.2. Flow-speed of the glacier calculated by Doppler-processing

In this section, we present Doppler-processed flow-speed of the Kronebreen glacier. This data was not published in Paper III. Highly detailed information can be extracted by Doppler-processing the radar data. The Doppler-processed result will give an average speed, while the interferometric data gives the instantaneous speed. Doppler-processing can highlight variations in the velocity, as any variation in velocity will result in a spread in the velocity-range data. Figure 25 shows Fourier processed range-flow and range-gate speed profiles respectively for two selected radar-scan angles measured from Pynten.

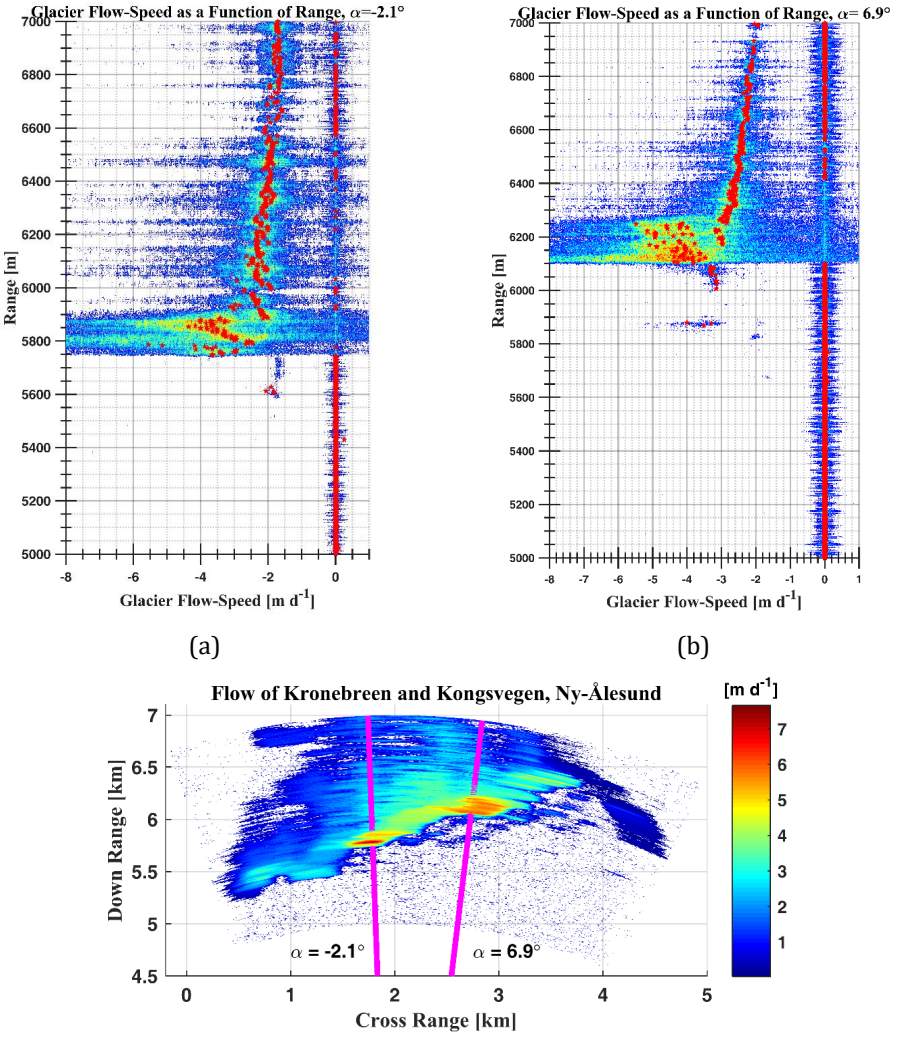

Figure 25. *Range-Speed profiles for a radar scan angle of -2.1° and 6.9° with respect to radar boresight. Panel (a) shows how the speed varies from 780 m in front of the glacier and 1,200 m up the glacier. The motions in the range from 5,000 m to 5,770 m are icebergs floating in the water, in front of the glacier. In panel (b) the glacier front is located at a range of 6,100 m. The two magenta lines in panel (c) show where the two range-speed profiles are located on the glacier. The red stars mark the most frequent flow-speed through a range-gate during the measurements. We used 4,096 points in the FFT giving a speed bin size of 13.3 mm/day.*

From Figure 25 we can extract detailed flow-speed of the glacier in the down-range direction. From Figure 25 (a) the first 786 m contain the reflections from the sea in front of the glacier. There is almost no motion detected in the sea, except at 5,610 m where there are some ice chunks. The average speed of the ice is -1.9 m/day, which indicates that the ice chunks are floating towards the radar. From 5,786 m and about 600 m up-glacier, we have the highest activity. For some range-gates the flow-speed exceeds 5 m/day during the measurements. From 6 to 7 km, the flow reduces from 2.3 m/day to 1.7 m/day. The speed from one range-gate reveals the temporal flow of one specific area on the glacier. From some range-gates on the glacier, there is no reflection. This occurs if the area of the range-gate is in a crevasse or if the range-gate is in an area of radio shadow. Figure 26 shows a detailed range-speed profile for a fixed scan-angle of 0.7° measured from Ny-Ålesund.

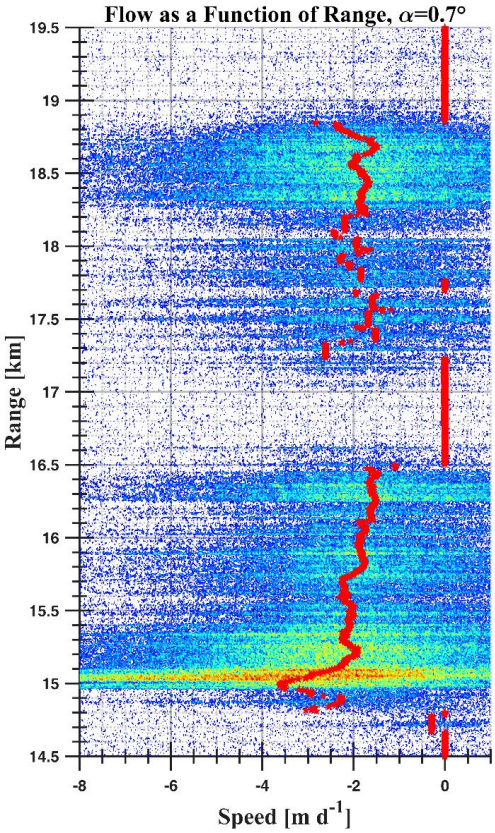

Figure 26. *Range-Speed profile for a fixed radar angle of 0.7°. The figure shows how the speed varies from 500 m in front of the glacier and 4,500 m up the glacier. The red stars mark the most frequent flow-speed through a range-gate during the measurements. We used 4,096 points in the FFT giving a speed bin size of 18.7 mm/day.*

The range-speed profile shows how the flow-speed of the glacier varies with range from the radar. Due to the calving activity, the highest speed is observed in the front of the glacier. Further, up the glacier the speed is reduced to an average of approximately 2 m/day. As with the results from Pynten we have some ice floating in the sea in front of the glacier.

3.3.3. Effect of the temporal resolution

In Figure 27 we look at how the number of points in the Fourier transform influence the computed flow-speed distribution in one range-gate.

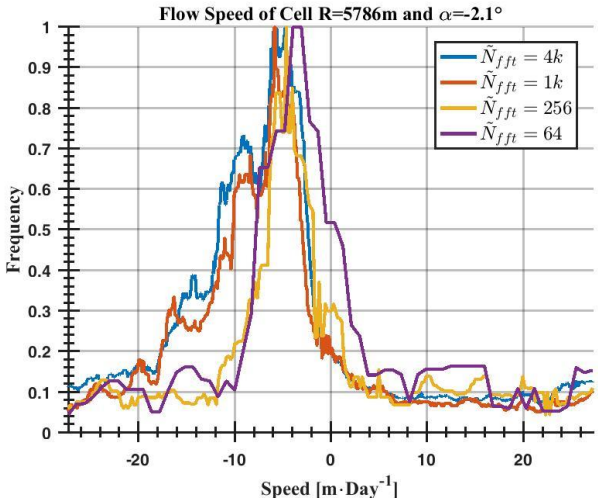

Figure 27. *Flow-speed as a function of the number of points used in the Fourier transform. The number of speed-bins depends on the length,* ***N****, of the Fourier transform. The impact of the number of points in the transformation is illustrated in the figure with* ***N*** *varying from 64 to 4k. For all values of* ***N,*** *a moving average of* ***N****/32 is used.*

Figure 27 highlights the relation between the length of the FFT and the resolution in flow-speed. When using fewer points, the distribution is close to the mean speed while a higher number of points reveal temporal variations in the flow-speed.

3.3.4. Glacier flow velocity through one range-gate

To get insight into the instantaneous measured variation in flow-speed we look at the computed speed through one range-gate, see Figure 28.

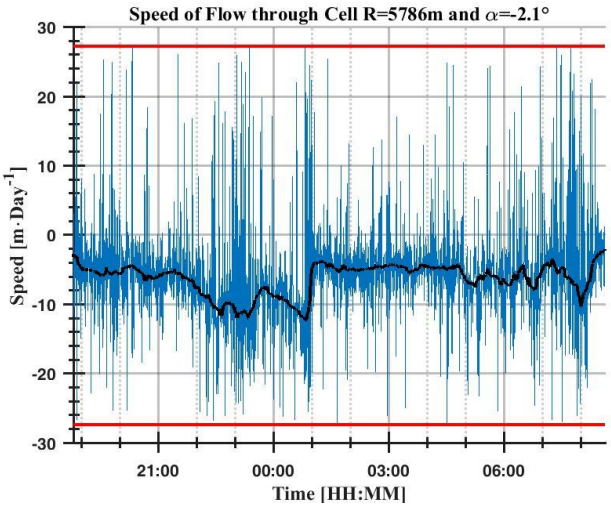

Figure 28. *Fourier processed data showing the flow-speed through one range-gate. The blue line is the instantaneous speed while the black line is a moving average. The data is for a angle of -2.1° and a range of 5,786 m. We have a possible calving event developing from 21:30 to 01:00, there is also some motion around 08:00. The red lines indicate the maximum unambiguous velocity we can measure with the radar settings used. The range-gate resolution is 2 m and the PRI is 12 s.*

From Figure 28 we observe that the maximum unambiguous velocity is reached several times during the measurements. Since the motion of the glacier is unidirectional it is unlikely that the positive velocities are measured glacier flow i.e. the glacier flowing backwards. One probable explanation of the positive flow is that due to the flow of the glacier the reflection points with highest backscatter intensity on the glacier surface are constantly changing. The major reflection may move within the range-gate both sideways and in range. From Equation (9), we know that the measured phase is the coherent sum of all scatterers within the range-gate. Another explanation is under sampling of the glacier flow as all glacier flow above the maximum unambiguous velocity is wrapped to a lower velocity. The noisy character of the instantaneous range-gate speed data indicates that a moving mean window gives a better representation of the actual glacier flow. The measured average flow-speed through this range-gate is –5.2 m/day.

4. Conclusions and outlook

4.1. Conclusions

The results of this work and discussion of the findings is covered in the published papers but a short summary of the key findings follows. This work has demonstrated the remote sensing capabilities of a ground-based real-aperture interferometric radar for monitoring geological events and hazards. We have further assessed the accuracy of real-aperture interferometric radar measurements and identified major error sources influencing the measurement accuracy. The main contributions of this work are:

- The study showed that interferometric radar measurements could achieve the same accuracy as differential interferometric radar if compensated for measurement geometry, temperature drift in the radar hardware, and variation in the atmosphere. The differential measurements showed inter-reflector oscillations, which increased inversely with the inter-reflector distance peaking when the reflectors were in the same range-gate.

- The study showed that ground-based interferometric radar produced reliable real-time weather-independent results, which is as accurate as in situ geotechnical instrumentation. The results show that high accuracy ground-based radar remote sensing is well suited for remote monitoring of geohazards.

- The study showed that a radar system with an electronically steered antenna is capable of high temporal and spatial mapping of glacier flow and geolocation of calving onsets and rotation of large blocks of ice. Measurement results gave detailed surface velocity maps of the glacier flow. The glacier was measured from two different locations and the only difference in results was the cross-glacier resolution, which declines with the radar-to-glacier distance.

4.2. Improvements and future research

In Paper I, we assessed methods for correcting interferometric measurements for geometric, atmospheric, and hardware variations. The meteorological data with a temporal resolution of one hour was collected from a meteorological station 2.7 km from the measurement site. Ideally, the data should have been recorded locally at the measurement site with high temporal resolution. This would probably give better correction of the variation in the refractive index.

In the towed reflector experiment, the cross-over signal from the transmitting to the receiving antennas should have been saved and used to compensate for variation in the radar hardware like the temperature induced change in length of the microwave cables, drift and ageing of the oscillators etc. This also applies to the results presented in Paper II and Paper III.

The experiment with the towed reflector should be repeated with the following enhancements: Local weather station, rail with position feedback, all four polarizations, and a longer distance between the rail and the stationary reflector. The radar installation in Fjøråå should be upgraded to a higher pulse repetition frequency and include at least one local weather station. If possible, the radar should be relocated to a location radial to the anticipated motional direction of the mountain crags. At the Kronebreen glacier, the addition of one or more reference reflectors close to the glacier would create reflection points with a more stable backscatter than the mountains.

Due to the rapid development and introduction of new and advanced integrated microwave circuits we expect the cost of remote sensing systems to drop substantially. Communication applications with high volumes and multiple companies offering circuits drive this development, which due to competition is likely to lower the component cost. The availability of processing is expected to increase which means that larger amounts of data may be processed in real-time even in compact remote sensing systems.

The introduction of high-performance ground-based remote sensing systems with electronically steered antennas that can continually create high amounts of data that will need purpose build processing to handle all the data in real-time.

In the future, we are likely to see a fusion of remote sensing data from multiple sensors combined to give a large area awareness. Automatic combination of data from various sources with varying accuracy calls for the use of machine learning as the amounts of data available will be too large for human assessment.

5. Publications from the thesis

5.1. Peer reviewed journal publications

1. *Gundersen R, Norland R, Denby Rolstad C*: Experimental and theoretical assessment of error sources and accuracy in interferometric and differential interferometric ground-based radar systems, Published in Remote Sensing, vol. 10 no. 12, 2018. doi.org/10.3390/rs10122070
2. *Gundersen R, Norland R, Denby Rolstad C*: Ground-Based Differential Interferometric Radar Monitoring of Unstable Mountain Blocks in a Coastal environment, Published in Remote Sensing, vol. 16 no. 6, 2018. doi.org/10.3390/rs10060914
3. *Gundersen R, Norland R, Denby Rolstad C*: Monitoring glacier flow and calving events with terrestrial interferometric radar in Ny-Ålesund, Svalbard, In review.

5.2. Conferences contributions

1. *Gundersen R.* High temporal and spatial interferometric radar measurements of Kronebreen, Spitsbergen, Svalbard Science Conference 2017 – cooperation for the future, 2017, Oslo, Norway.
2. *Norland R, Gundersen R*: Lateral mapping of glacier flow-speed with a scanning radar. 2018 IEEE International Geoscience and Remote Sensing Symposium, 2018, Valencia, Spain
3. *Norland R, Gundersen R*: Ground-Based Radar for Permanent Monitoring of Landslides. Landslide Science and Practice, Proceedings of the Second World Landslide Forum, pp 525-530, 2013. doi.org/10.1007/978-3-642-31445-2.
4. *Denby Rolstad C*, *Gundersen R*: Ground based radar measurements in a marine environment for glacier calving front studies. EGU General Assembly 2012, 22-27 April, 2012 in Vienna, Austria, p.4486

Bibliography

[1] J. R. R. S. M. Hansen and K. Lo, “Global surface temperature change,” *Reviews of Geophysics,* vol. 48, no. 4, 2010.

[2] S. Banholzer, J. Kossin and S. Donner, “The Impact of Climate Change on Natural Disasters,” in *Reducing Disaster: Early Warning Systems for Climate Change*, A. Singh and Z. Zommers, Eds., Dordrecht, Springer, 2014, pp. 21-49.

[3] L. Blikra, G. A. E. Majala, H. Berg, O. Eikenæs, G. Helgås, T. Oppikofer, R. Hermanns and M. Böhme, “Rapport nr 77-2016, Fare- og risikoklassifisering av ustabile fjellparti, Faresoner, arealhåndtering og tiltak,” Norges vassdrags- og energidirektorat (NVE), Oslo, 2016.

[4] P. Gleick, “Water resources,” *In encyclopedia of climate and weather,* vol. 2, pp. 817-823, 1996.

[5] J. L. Bamber, R. M. Westaway, B. Marzeion and B. Wouters, “The land ice contribution to sea level during the satellite era,” *Environmental Research Letters,* vol. 13, no. 6, p. 063008, June 2018.

[6] J. E. Box, T. C. Colgan, B. Wouters, D. O. Burgess, S. O'Neel, L. I. Thomson and J. S. Haugaard Mernild, “Global sea-level contribution from Arctic land ice: 1971 to 2017.,” *Environmental Research Letters,* vol. 13, no. 12, p. 125012, 2018.

[7] T. Moon, A. Ahlstrøm, H. Goelzer, W. Lipscomb and S. Nowicki, “Rising Oceans Guaranteed: Arctic Land Ice Loss and Sea Level Rise,” *Current Climate Change Reports,* vol. 4, no. 3, pp. 211-222, 2018.

[8] C. Rolstad and R. Norland, “Ground-based interferometric radar for velocity and calving-rate measurements of the tidewater glacier at Kronebreen, Svalbard,” *Annals of Glaciology,* vol. 50, pp. 47-54, 2009.

[9] N. Levanon, Radar Principles, Tel-Aviv: John Wiley & Sons, 1988.

[10] M. A. Richards, Fundamentals of Radar Signal Processing, 2nd ed., New York: McGraw Hill Education, 2014, p. 656.

[11] M. Skolnik, Radar Handbook, Second ed., McGraw-Hill, 1990, p. 1200.

[12] E. Knott, J. Shaeffer and M. Tuley, Radar Cross Section, Its Prediction, Measurement and Reduction, Nortwood, MA: Artech House Inc, 1985, p. 462.

[13] L. Graham, "Synthetic interferometer radar for topological mapping.," *Proceedings of the IEEE,* vol. 62, no. 6, pp. 763-768, 1974.

[14] C. Chen and H. A. Zebker, "Phase unwrapping for large SAR interferograms: statistical segmentation and generalized network models.," *IEEE Transactions of Geoscience and RemoteSensing,* vol. 40, no. 8, pp. 1709-1719, 2002.

[15] R. Hanssen, Radar Interferometry: Data Interpretation and Error Analysis., Dordrecht: Kluwer Academic Publishers, 2002.

[16] P. C. R. F. Ferretti A, "Permanent csatterers in SAR interferometry," *Transaction on Geoscience and Remote Sensing,* vol. 39, no. 1, pp. 8-20, 2001.

[17] R. Bracewell, The Fourier Treansform and its application, New York: McGraw-Hill, 1986.

[18] A. L. Buck, "New equations for computing vapor pressure and enhancements factor," *Journal of Applied Meteorology,* vol. 20, pp. 1527-1532, 1981.

[19] K. K. Pranab, Micrwave Propagation and Remote Sensing, Atmospheric Influences with Models and applications, New York: CRC Press, 2011.

[20] J. M. Rüeger, "Refractive Index Formulae for Electronic Distance Measurement with Radio and Millimetre Waves," School of Surveying and Spatial Information Systems, University of New South Wales, Sydney, Australia , 2002.

[21] ISO, ISO 2533-1975, Standard Atmosphere, Geneva: International Organization for Standardization, 1975.

Paper I

Experimental and theoretical assessment of error sources and accuracy in interferometric and differential interferometric ground-based radar systems.

Gundersen R, Norland R, Denby Rolstad C, Remote Sensing, vol. 10 no. 12, **2018**.
https://doi.org/10.3390/rs10122070

remote sensing

MDPI

Article

Geometric, Environmental and Hardware Error Sources of a Ground-Based Interferometric Real-Aperture FMCW Radar System

Rune Gundersen [1,2,*], Richard Norland [2] and Cecilie Rolstad Denby [1]

[1] Faculty of Science and Technology, Norwegian University of Life Sciences, 1433 Ås, Norway; cecilie.rolstad.denby@nmbu.no

[2] ISPAS AS, P.O. Box 506, 1522 Moss, Norway; richard.norland@ispas.no

* Correspondence: rune.gundersen@nmbu.no; Tel.: +47-9055-8418

Received: 28 September 2018; Accepted: 17 December 2018; Published: 19 December 2018

Abstract: Ground-based interferometric radar systems have numerous environmental monitoring applications in geoscience. Development of a relatively simple ground-based interferometric real-aperture FMCW radar (GB-InRAR) system that can be readily deployed in field without an established set of corner reflectors will meet the present and future need for real-time monitoring of the expected increased number of geohazard events due to climate changes. Several effects affect electromagnetic waves and limit the measurement accuracy, and a careful analysis of the setup of the deployed radar system in field is essential to achieve adequate results. In this paper, we present radar measurement of a moving square trihedral corner reflector from experiments conducted in both the field and laboratory, and assess the error sources with focus on the geometry, hardware and environmental effects on interferometric and differential interferometric measurements. A theoretical model is implemented to assess deviations between theory and measurements. The main observed effects are variations in radio refractivity, multipath interference and inter-reflector interference. Measurement error due to radar hardware and the environment are analyzed, as well as how the geometry of the measurement setup affects the nominal range-cell extent. It is found that for this experiment the deviation between interferometry and differential interferometry is mainly due to variations in the radio refractivity, and temperature-induced changes in the electrical length of the microwave cables. The results show that with careful design and analysis of radar parameters and radar system geometry the measurement accuracy of a GB-InRAR system without the use of deployed corner reflectors is comparable to the accuracy of differential interferometric measurements. A GB-InRAR system can therefore be used during sudden geo-hazard events without established corner reflector infrastructure, and the results are also valid for other high-precision interferometric radar systems.

Keywords: radar; interferometry; multipath interference; inter-reflector interference

1. Introduction

The all-weather capability of radar makes it the natural instrument for real-time monitoring in geosciences for potential life-threatening natural events like rock and mountain slides; clay and snow avalanches; volcanoes; open pit mines [1]; and structural monitoring of dam fronts [2], buildings and bridges [3–5]. The use of ground-based interferometric real aperture radar to measure unstable mountains [6–9], landslides [10], glacier movements, and calving events [11–13] gives good results. Experience from radar measurements shows that environmental and geometrical effects limit or have a great influence on the accuracy of the measurements. In a recent 8-year study of monitoring an

unstable mountainside [6], it was found that atmospheric decorrelation was the major factor limiting the measurement accuracy when monitoring submillimeter motion at distances of 3 to 4 km. In this study and in Reference [8], it was shown that by introducing a reference reflector and by performing differential interferometry, most of the variations caused by atmospheric decorrelation were removed. However, it is not always possible to introduce radar reflectors due to the nature of the monitored area or from a safety point of view, typically for an unstable mountain with a lot of motion and occasional rock falls. In cases with unexpected geological hazards, it may not be possible to establish a set of corner reflectors. There is, therefore, a need for a thorough assessment of GB-InRAR systems, including radar hardware, measurement geometry and environmental effects, to find ways to compensate for the interferometric measurements for the environmental and geometrical effects in order to achieve accuracies comparable to differential interferometry.

Published literature on environmental variations on longtime geological monitoring with real-aperture radar are scarce as the main focus is on space-borne and ground-based Synthetic Aperture Radar (SAR); however, the environmental effects discussed in the literature are also for the use of Frequency Modulated Continuous Wave (FMCW) GB-InRAR systems. Atmospheric decorrelation was first observed in space-born SAR data when assessing slow subsidence rates [14]. To overcome the problem of atmospheric decorrelation, the Permanent Scatter (PS) Technique was developed [15], and a thorough analysis of the technique is given in Reference [16]. The technique utilizes time-coherent pixels to help bypass the geometrical and temporal decorrelation. Efficient techniques for compensation of GB-SAR based on statistical analysis of local meteorological data in combination with PS is reported in References [17–20]. In Reference [20] it was noted that compensating for atmospheric decorrelation due to temperature-induced turbulence and long distances is still a challenge. A recent study of Alpine glaciers in Italy and Spain reports an accuracy of a few millimeters/day when applying atmospheric phase screening (APS) corrections under challenging atmospheric conditions [13]. Accuracy improvements for real-aperture differential interferometric radar based on local meteorological data are reported in Reference [8].

One of the main differences between GB-SAR and real-aperture radar is the two-dimensional mapping capability of the GB-SAR system. The cost of 2D mapping is longer data acquisition time due to the mechanical motion of the antenna, which makes the GB-SAR system more sensitive to atmospheric and geometric decorrelation both during and between data acquisition. As stated in Reference [19], the time between data acquisition should be reduced as much as possible to avoid significant variation in the atmospheric conditions between measurements. Typical acquisition times of a GB-SAR-system are in the order of minutes while a typical real-aperture radar has a pulse repetition frequency (PRF) of a few thousand measurements per second. The high PRF of the real-aperture radar makes it easier to track and correct for atmospheric decorrelation due to the temporal variation in temperature, humidity and the pressure between measurements.

The geometry of the system must be considered carefully when deploying a GB-InRAR. When deploying an on-demand remote sensing system it is often time-critical to get the system operational and on-line. The choices of where to locate the radar are often restricted and the measurement geometry may deviate from an optimum radar measurement setup. If the radar is not radially directed against the anticipated motional direction of the monitored objects, the motion will be underestimated and must be corrected for. Another geometrical effect that may affect the measurement accuracy is multipath interference [21]. Multipath interference can occur when the energy radiated from the radar antenna hits a reflective surface, usually the ground, and is reflected towards the target. This additional signal adds coherently to the direct path signal and deteriorates the phase and magnitude of the data. It is stated in Reference ([22]; p. 2.31) that multipath interference is the most important non-free-space effect. A ripple in the amplitude of the backscatter from both stationary and moving objects is another geometric effect observed in high-resolution radar measurements of moving objects, where the data acquisition time is substantially faster than the velocity of the tracked object. This effect is probably coupled to the relative radar cross-section (RCS) value of the objects in the measurement area.

Environmental effects affect all radar system hardware, however, unlike a permanently installed remote sensing system an on-demand deployed system is more likely to be exposed to environmental variations as no infrastructure or environmental shielding can be expected to be present. The frequency and phase stability of microwave hardware is sensitive to variation in temperature, and this applies especially to oscillators and microwave cables. Uncorrected, this may lead to variations in the measured interferometric distance and a decrease in measurement accuracy. In Reference [23] it is stated that the temperature-induced phase shift in microwave cables is critical in high performance measurements. The magnitude of the phase-shift depends on the length of the cable and the operational temperature range of the radar system. The temperature-induced variation in the radar hardware should be separated from the temperature-induced environmental effects to avoid overcompensation of either effect.

A concern when measuring displacements without the use of reflectors is strong scatterers on the surface illuminated by the radar. Strong scatterers may be natural, e.g., stone blocks, or artificial, e.g., rockfall catch fences. Their presence may negatively affect the accuracy of the measurements as the strong back scatterers may interfere or shadow the backscatter from the other objects in the monitoring area. In Reference [24] it is stated that when monitoring in the presence of rockfall catch fences the interferometric phase information is not reliable. This is likely due to multiple effects like strong backscatter, shadowing and interference. In Reference [25] it is stated that GB-SAR is less suited for single-point monitoring than GB-InRAR in the presence of spatially-concentrated backscatter. This may be due to the azimuth width of the antennas, which for GB-SAR usually is much wider than for GB-InRAR, resulting in a larger illuminated area, hence, making the GB-SAR more vulnerable to cross-range interference. It is therefore of interest to assess the effect experimentally by tracking objects in the presence of stationary strong scatterers.

In this paper, we have investigated the effects influencing interferometric measurements of moving targets using a GB-InRAR, with a focus on applications in geosciences. Both controlled field and laboratory measurement experiments were set up to assess the effects influencing the measurement accuracy. In addition, a software model was developed to verify these effects. A series of experimental interferometric radar measurements were conducted on both stationary and moving targets. The purpose of the measurements was to gather information on how various environmental and geometric effects influenced the accuracy of the measurements, and to find a way to predict and correct for the effects, so that a relatively simple GB-InRAR system can be readily and optimally employed on site for field measurements.

This paper deals with five major effects influencing the accuracy of interferometric and differential interferometric radar measurements:

- The geometry of the measurement setup
- Atmospheric effects i.e., radio refractivity
- Effect of ground reflections i.e., multipath interference
- Radar target interference
- The radar hardware

The presented field results are utilizing the measured phase information registered by the GB-InRAR from the company ISPAS AS, and movements are calculated from phase differences based on the principle of interferometry. To exclude any systematic artifacts of the GB-InRAR, the laboratory measurements were all made using a Rhode & Schwarz Vector Network Analyzer (VNA).

In this paper, we start by outlining the radar theory necessary to analyze the measured data and to develop the numerical simulation model. We then describe the measurement setup and compare the field measurements with the results from the numeric model. Finally, we discuss the error sources and the factors limiting the accuracy of interferometric measurements and give some advice regarding setup and operational measurements.

2. Radar Theory and Implementation of Numerical Model

In this section, the theory for the implemented numerical simulation model and some of the radar theory that is used in the analysis of the measurements are presented.

2.1. Modeling of FMCW Radar Signals

A numerical simulation model was implemented, based on analytic expressions, to analyze and find deviations between theoretic and measured results. The transmitted radar signal is [26]

$$u(t) = A_u \cos \varphi_u = A_u \cos\left(2\pi\left(f_0 + \frac{\alpha}{2}t\right)t + \varphi_0\right), \quad (1)$$

where A_u is the amplitude of the transmitted signal; f_0 is the frequency of the carrier; α is the ramp rate of the modulating signal; $\alpha = \frac{BW}{T_{sweep}}$ where BW is the bandwidth of the modulated signal, T_{sweep} is the modulation time and φ_0 is the initial phase of the transmitted signal. The received radar signal is [26]

$$z(t) = A_z \cos \varphi_z = A_z \cos\left(2\pi\left(f_0 + \frac{\alpha}{2}(t-\tau)\right)(t-\tau) + \varphi_0\right), \quad (2)$$

where τ is the travel time of the electromagnetic wave. The received signal is split in two parts; one part is down-converted by in-phase and the second part by a 90°-shifted time delayed copy of the transmitted signal. The decomposition of the received signal in quadrature channels is [26]

$$I(t) = A'_z \cos\left(2\pi\left(\frac{\alpha}{2}\tau - \alpha t\right)\tau\right), \quad (3)$$

$$Q(t) = A'_z \sin\left(2\pi\left(\frac{\alpha}{2}\tau - \alpha t\right)\tau\right) \quad (4)$$

where I(t) is the in-phase part and Q(t) is the quadrature part of the signal. The amplitude and phase of the complex down-converted signal are

$$A(t) = \sqrt{I(t)^2 + Q(t)^2}, \quad (5)$$

$$\varphi(t) = \tan^{-1}\left(\frac{Q(t)}{I(t)}\right), \quad (6)$$

where A(t) is the amplitude and φ(t) is the phase of the received signal. The output from this computational model is used to analyze and verify the measurement.

2.2. Effects Comprising the Interferometric Phase

Interferometric radar measurements exploit the phase φ of the electromagnetic wave to derive information from the reflecting object. The interferometric phase φ is the sum of multiple effects

$$\varphi(t) = \frac{4\pi R}{\lambda} + \varphi_{atm} + \varphi_{noise} + \varphi_{cable}, \quad (7)$$

where $4\pi R/\lambda$ is the phase due to the displacement of the target, φ_{atm} is the phase due to radio refractivity, φ_{noise} is the phase noise due to the radar hardware, and φ_{temp} is the phase due to thermal expansion of the microwave cable. Movements are calculated for measured phase differences using standard theory of interferometry.

2.3. Reflection Coefficient and Multipath Interference

When conducting radar measurements close to the earth's surface, the results may differ from ideal free-space theory if the antenna lobe touches the ground. There may be reflections from the surface and possibly multiple signal paths between the radar and the target. Then there is a direct

signal from the radar to the target and an indirect signal from the radar to the target via the ground. The amplitude and phase of this indirect signal depends on the nature of the surface i.e., its roughness relative to the frequency of the radar waves, the dielectric constant of the surface and the grazing angle. The complex Fresnel reflection coefficients for a smooth surface for vertical Γ_v and horizontal Γ_h polarization are ([27]; pp. 70–71).

$$\Gamma_v = \frac{\varepsilon \sin\psi_g - \sqrt{\varepsilon - \left(\cos\psi_g\right)^2}}{\varepsilon \sin\psi_g + \sqrt{\varepsilon - \left(\cos\psi_g\right)^2}} \tag{8}$$

$$\Gamma_h = \frac{\sin\psi_g - \sqrt{\varepsilon - \left(\cos\psi_g\right)^2}}{\sin\psi_g + \sqrt{\varepsilon - \left(\cos\psi_g\right)^2}} \tag{9}$$

where ψ_g is the grazing angle and ε is the complex dielectic constant of the surface,

$$\varepsilon = \varepsilon' - j\varepsilon'', \tag{10}$$

where ε' is the real part of the permittivity and ε'' is the complex part of the permittivity.

As an example, the dielectric constant for dry snow is found to be $\varepsilon' = 3.15$ and $\varepsilon'' = 0.003$ at 6 GHz [28,29]. The resulting reflection coefficient magnitude and phase versus grazing angle are shown in Figure 1 for both horizontal and vertical polarization.

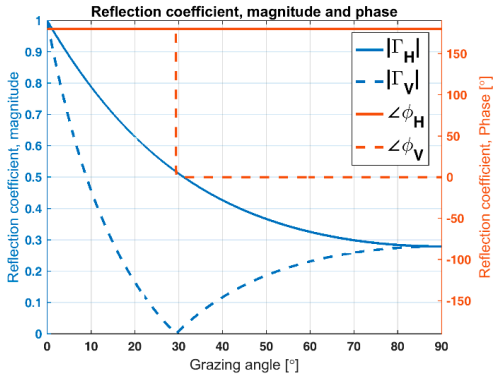

Figure 1. The Fresnel reflection coefficient as a function of grazing angle. The dielectric constant used for snow is $\varepsilon' = 3.15$ and $\varepsilon'' = 0.003$ at 6 GHz. The blue lines are the magnitude of the reflection coefficients and the red lines are the phase of the reflection coefficients. Dotted lines are vertical polarization and the unbroken lines are horizontal polarization.

The result presented in Figure 1 is based on Equations (8) and (9) and assumes a smooth reflecting surface. To get a more realistic value of the reflection coefficient, the roughness of the surface must be considered. The surface roughness is ([30]; p. 307)

$$S_r = e^{-2\left(\frac{2\pi h_{rms} \sin\psi_g}{\lambda}\right)^2} \tag{11}$$

where h_{rms} is the rms variation in height of the surface which was estimated from visual inspection to be between 20 to 30 mm. Equations (8) or (9) multiplied by Equation (10) gives us the total reflection

coefficient for a rough surface. To include the effect of multipath interference, the received power equation ([30]; p. 39) will be modified by the propagation factor F ([27]; p. 76)

$$|F^4| = 16\left(\sin\left(\frac{2\pi h_r \sin\psi_g}{\lambda}\right)\right)^4 S_r, \tag{12}$$

where h_r is the height of the target relative to the height of the radar antennas. This implies that the energy backscattered from an object will vary depending on the grazing angle from zero to sixteen times the value calculated based on Equation (12).

2.4. Inter-Reflector Interference

When there are two or more scattering objects in the radar scene they will interact. Their mutual distance gives the magnitude and phase of this interaction. This will result in range-dependent constructive and destructive interference according to the exponent in the equation for the RCS of multiple objects ([27]; p. 26)

$$\sigma = \left|\sum_{n=1}^{M} \sqrt{\sigma_n} e^{\left(\frac{i4\pi R_n}{\lambda}\right)}\right|^2 \tag{13}$$

where M is the number of scatterers in the range-cell and σ_n is the RCS of the n individual scatterers.

2.5. Electrical Length of Microvawe Cabels

The electrical length of microwave cables vary with temperature and is referred to as the phase-temperature response of the cable in Equation (7). For a lossless microwave cable, the phase velocity is ([31]; p. 51)

$$v_p = \frac{\omega}{\beta} = \frac{1}{\sqrt{L'C'}}, \tag{14}$$

where ω is the radian frequency, β is the phase constant, L' is the distributed inductance per unit length, and C' is the distributed capacitance per unit length between the two conductors in the cable.

The velocity factor or wave propagation speed in the microwave cable is the phase velocity from Equation (14) divided by the speed of light

$$VF = \frac{1}{c_0\sqrt{L'C'}} \tag{15}$$

Hence, the propagation speed depends on the physical properties of the cable. Typical values of VF are between 0.6 and 0.85 of c_0. These properties will change with temperature, and the electrical length of the cable will change accordingly. This physical change will affect the phase of the received signal and will be part of φ_{cable} in Equation (7).

2.6. Free Space Path-Loss

The free space path loss (FSPL) is the loss in signal strength an electromagnetically wave suffers when it travels in a straight line through free space ([32]; p. 2)

$$FSPL = 20\log_{10}\left(\frac{4\pi R}{\lambda}\right), \tag{16}$$

where R is the radar-to-target distance which must be multiplied by two since radar is a two-way measurement; λ is the wavelength of the electromagnetic wave.

3. Experimental Field and Laboratory Measurement Setup

In this chapter, the test setups used to assess the effects of the radar measurements are presented is some detail.

3.1. Field Measurement Setup

The measurements were conducted outdoors in an open field covered with approximately 0.5 m of snow. The windswept compact snow provided a uniform flat surface. To track the motion of the reflector and compare the accuracy achievable with interferometry and differential interferometry, a square corner reflector was towed along a 6-m-long aluminum rail with a velocity of roughly 220 μm/s. The rail was aligned radially to the radar radiation direction, 157 m from the radar. A reference reflector was located 8 m further downrange from the end of the rail. A radar bandwidth of 150 MHz was used which gives a nominal range resolution of 1 m. With this setup, the motion of the towed reflector could be observed through five complete range cells. In this setup, the PRI is 0.9517 s and $\lambda_{5.7GHz}$ = 52.6 mm giving a maximum unambiguous velocity of approximately v_{max} = 13.8 mm/s.

Figure 2 shows a picture of the field measurement setup. The relevant parameters of the radar used in the field experiment are given in Table 1.

Figure 2. Picture showing the setup of the field experiment. The square trihedral corner reflector is in the front on top of the rail and in the rear is the reference triangular trihedral corner reflector on the tripod. Both the rail and the reference reflector were radially aligned to the look angle of the radar.

Table 1. FMCW Radar Parameters.

FMCW Radar Parameters	Value
Center Frequency, fc [GHz]	5.70
Bandwidth, BW [MHz]	150
Pulse Repetition Frequency, PRI [s]	0.9517
Maximum Unambiguous Velocity, vmax [m/s]	0.0138
Polarization	VV
RCS of Towed Reflector, [dBsm]@ 5.70 GHz	20.4
RCS of Stationary Reflector, [dBsm] @ 5.70 GHz	13.1

By towing the reflector at a speed of 220 μm/s the number of measurements per range cell were roughly 4780, which equals approximately 250 measurements per wavelength. This assures an unambiguous phase unwrapping when performing the interferometric calculations.

3.2. Geometry of the Outdoor Experiment

The geometry of the setup is illustrated in Figure 3.

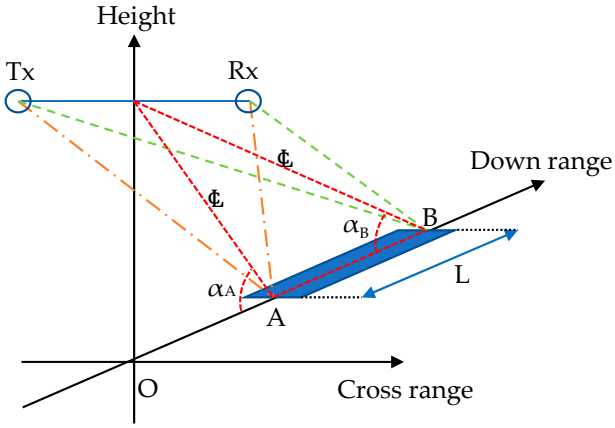

Figure 3. Illustration of the measurement setup. The angles and distances are exagerated compared to the real-life setup to highlight the geometry. A marks the close end of the rail, B marks the far end of the rail and L is the length of the rail. The angle α_A and α_B are referred to as angle of depression. The red lines mark the centerline path of the electromagnetic waves while the green and orange lines mark the actual path of the electromagnetic waves due to the distance between the transmitting and receiving antennas.

In Figure 3, α_A is the angle between the electromagnetic waves and the close end of the rail and α_B is the angle between the electromagnetic waves and the far end of the rail. The towing of the reflector will change the geometry and result in a varying angle between the electromagnetic waves and the towed reflector. This gives a range-dependent variation in the range cell length ($\delta = \Delta R / \cos \alpha$), in this case, an increase of approximately 2 mm. The geometrical modified range cell size for the length of the rail is given in Table 2.

Table 2. Variation in range cell size as the reflector is towed along the rail.

Distance [m]	157	158	159	160	161	162
Range Cell Increase [mm]	1.96	1.94	1.93	1.91	1.89	1.88

3.3. Laboratory Measurement Setup

In addition to the outdoor experiment, two laboratory experiments were conducted to verify the results for the towed reflector experiment. The first experiment was conducted to assess the effect of shadowing the reference reflector. Two half-scale corner reflectors were used. In front, is the square trihedral corner reflector on a Styrofoam support. In the rear, is the triangular trihedral corner reflector mounted on a linear actuator. To suppress unwanted reflections from the measurement, fixture microwave absorbers were used. To eliminate any unforeseen irregularity from the radar hardware, a Rohde & Schwarz Vector Network Analyzer was used in stepped frequency mode with a center frequency of 11.4 GHz, since half-scale reflectors were used. A picture of the measurement setup is given in Figure 4.

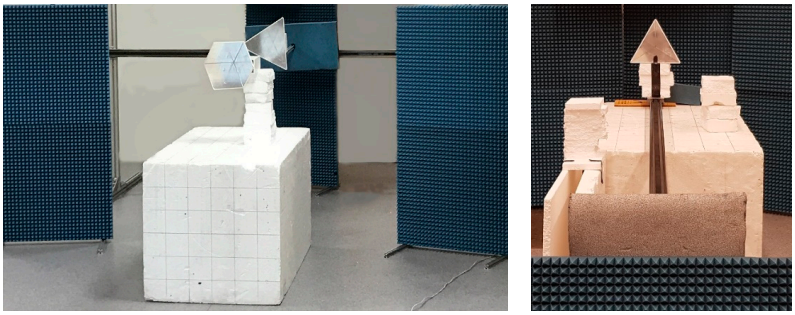

(**a**) (**b**)

Figure 4. Pictures showing the setup of the laboratory experiments. (**a**) In front is the square trihedral corner reflector on a Styrofoam support. In the rear is the triangular trihedral corner reflector mounted on a linear actuator. Microwave absorbers were used to suppress unwanted reflections from the measurement fixture. (**b**) Triangular corner reflector at the far end of the linear actuator.

Three measurements were conducted; in the first, the reflector was moved 1800 mm radially towards the radar in increments of 200 µm. In the second measurement, a stationary reflector was introduced 520 mm from the far end of the rail, and then the motion of the first reflector was repeated. In the third measurement, a second stationary reflector was introduced 1170 mm from the far end of the rail and the motion of the first reflector was repeated. The VNA was operated with a center frequency of 32 GHz with a bandwidth of 1500 MHz. Microwave absorbers were used to suppress reflections from the floor, walls and rail. The distance from the antennas to the near end of the linear actuator was approximately 5.5 m.

4. Experiment Results

In this chapter, we first present and compare the measurements with the theoretical calculations. The analysis of the differences is divided into the following subsections: amplitude analysis, radio refractivity, multipath interference, reflector interference, and electrical length of microwave cables. We then assess the geometric, environmental and hardware influence on interferometric and differential interferometric measurements. Finally, we summarize all measurement results. The range to the targets is given as the radar range cell number rather than the actual distance in meters.

4.1. Amplitude Analysis

We start by comparing the amplitude of measured backscatter with the computed values to highlight the differences. The resulting normalized High-Resolution Range (HRR) plot from the towed reflector experiment is shown in Figure 5a. The results from the numerical model based on Equations (2) and (5) are shown in Figure 5b.

Figure 5a shows how the amplitude of the reflected energy from the towed reflector changes as it is moved away from the radar. The reflector starts in range index 164 and ends in range index 169. The reference reflector remains stationary in range index 177. The amplitude of the stationary reflector is approximately five times lower than the towed reflector due to its smaller size; see Table 1. Figure 5b shows the computed backscatter from the numerical model.

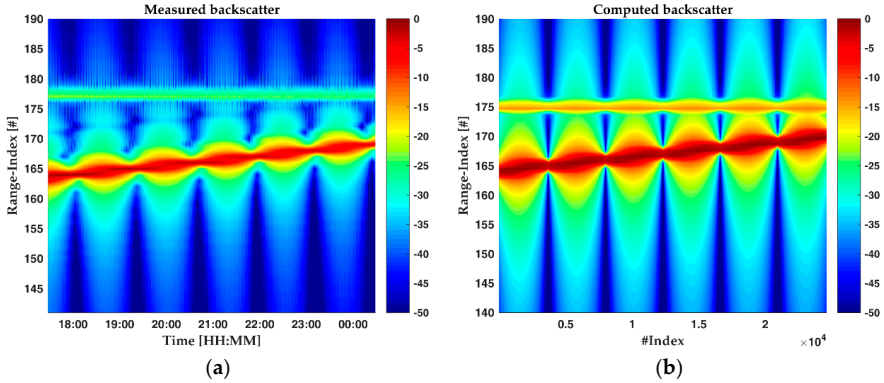

Figure 5. Time-Range plot, (**a**) measured as a function of time and (**b**) simulated as a function of the numerical simulation (#index). Likewise in other captions, such as Figures 6 and 10. The figure shows how the energy is shifted from range cell to range cell as the reflector is towed away from the radar. The reference remains stationary at range index 177. (**b**) The x-axis shows the simulation step index.

Figure 6a,b shows a cut through Figure 5a,b following the maximum amplitude of the backscattered energy.

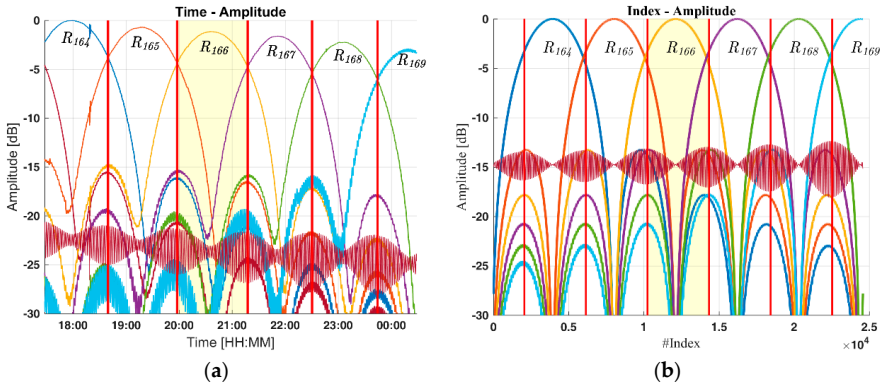

Figure 6. Normalized amplitude of backscattered energy, (**a**) measured as a function of time and (**b**) simulated as a function of numerical simulation #index. The range index is marked at the peak of each range cell. The range-resolution is indicated with the vertical red lines.

The measurements and the computed results correlate to some extent, but major differences are observed, like the reduction in amplitude as the towed reflector is moved away from the radar. The theoretical attenuation from the FSPL, see Equation (16), is approximately 0.33 dB while we observe a close to 3 dB attenuation. This missing 2.7 dB is, as discussed in the next section, believed to be caused by ground reflection or multipath interference. Another difference is the amplitude level of the stationary reflector, which starts 7 dB below the theoretic value and drops in amplitude as the towed reflector gets closer. This is partly believed to be caused by shadowing which will be addressed in Appendix A. The oscillations in the amplitude of the backscatter from the reference reflector are observed in both Figure 6a,b. This oscillation is believed to be caused by constructive and destructive interference between the two reflectors which is discussed in Section 4.3.

4.2. Multipath Interference

To assess whether the excess damping of the amplitude of the towed reflector was caused by multipath interference, the geometry of the measurement setup was analyzed. During the measurements, the ground was covered by windswept compact snow, which provided a smooth reflecting surface. The difference between the direct path and the indirect path of the backscatter varies with the grazing angle ψ_g. In the measurements, the change in grazing angle comes from the towing of the reflector as illustrated in Figure 7.

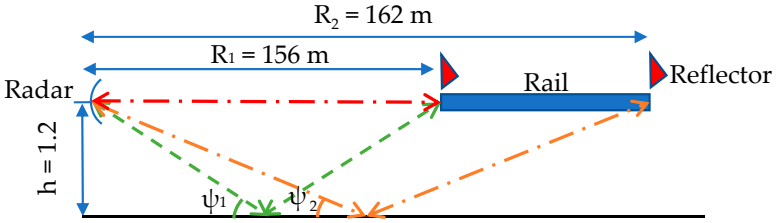

Figure 7. Vertical geometry of the measurement setup. When the reflector is towed along the rail, the grazing angle will change from $\psi_1 = 3.01°$ to $\psi_2 = 2.89°$ due to the change in the measurement geometry. The red line indicates the direct path between the radar and the towed reflector and the green and orange line is the indirect path respectively at the near and far end of the rail.

The geometrical change in range and angle, when towing the reflector, will produce an alternating constructive and destructive pattern according to Equation (13). This pattern is proportional to the wavelength and is inversely proportional to the height of the radar above the ground. In this measurement setup, the first four maxima will occur for a grazing angle of $\psi = 0.63°$, $1.89°$, $3.15°$, and $4.41°$ likewise the four first minima will occur at $\psi = 0°$, $1.26°$, $2.52°$, and $3.78°$. Figure 8 shows the variation in amplitude as a function of the grazing angle relevant for the measurement geometry.

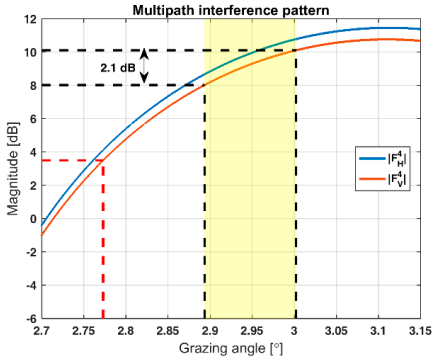

Figure 8. Variation in magnitude as a function of grazing angle. At the near end of the rail, the grazing angle is close to $\psi = 3°$ and at the far end $\psi = 2.88°$ as indicated by the yellow patch. This multipath interference-induced modification of the propagation will lead to an additional damping of the reflection by approximately 2.1 dB. The red line indicates the multipath interference gain of the stationary reflector.

Figure 8 shows that a 2.1 dB attenuation of the backscattered energy from the towed reflector due to the change in measurement geometry. By adding the multipath interference loss to the FSPL of 0.3 dB, the total loss is 2.4 dB, which correlates well with the measured 2.7 dB attenuation of the

towed reflector. Based on this analysis it is believed that multipath interference is the main cause of the damping of the reflected energy from the towed reflector.

4.3. Constructive and Destructive Interference between Reflectors in the Measurement Scene

The amplitude oscillations in the backscatter from the stationary reflector in Figure 6 are believed to be caused by inter-reflector interference. The distance to the stationary reflector is constant, hence the frequency of its demodulated signal is constant. The distance to the towed reflector changes proportionally with the tow-speed and the demodulated signal will produce a time-varying increasing frequency. To verify the inter-reflector interference, a laboratory experiment was undertaken, and the measurements are presented in Figure 9.

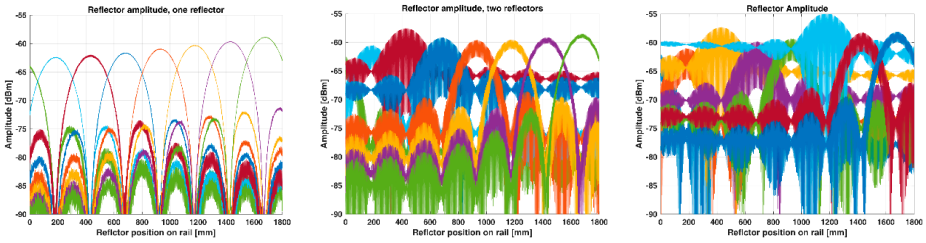

(**a**) (**b**) (**c**)

Figure 9. Measured amplitude as a function of reflector position on the rail. (**a**) Amplitude of the single reflector. (**b**) Same as (**a**) but with a stationary reflector at 520 mm, which is equal to 0.4 times the range cell extent from the center of the range cell. (**c**) Same as (**b**) but now with an additional stationary reflector at 1170 mm, which is at the center of the range cell.

Figure 9a shows little variation in amplitude of the backscatter from the towed reflector apart from the 3 dB variation which is a function of the reflector's position within the range cell and the FSPL attenuation of approximately 2 dB. When a second and third reflector are introduced, as shown in Figure 9b,c, there is a noticeable increase in the amplitude variation of the moved reflector. The amplitude decreases with the distance to the stationary reflector, and the peak occurs when they are in the same range cell. In Figure 9b, the stationary reflector is located 0.4 times the distance from the center of the range cell, while in Figure 9c it is located at the center. Based on this experiment, the amplitude variations observed in Figure 6a are believed to be caused by inter-reflector interference.

4.4. Comparison of Measured and Numerically Calculated Inerferometric and Differentail Interferometric Motion

During the outdoor experiment, the actual position of the towed reflector was not recorded. To find the extent of the range cells, the point where the maximum amplitude has fallen by $\sqrt{2}$ or the 3 dB-point is used. However, since there are several environmental effects affecting the amplitude it was simply recorded when the maximum returned energy was shifted from one range cell to the next. The distance between the two amplitude intersections is the range cell resolution, as indicated by the vertical red lines in Figure 6. The measured motion from the outdoor measurement is shown in Figure 10a and the computed motion is show in Figure 10b.

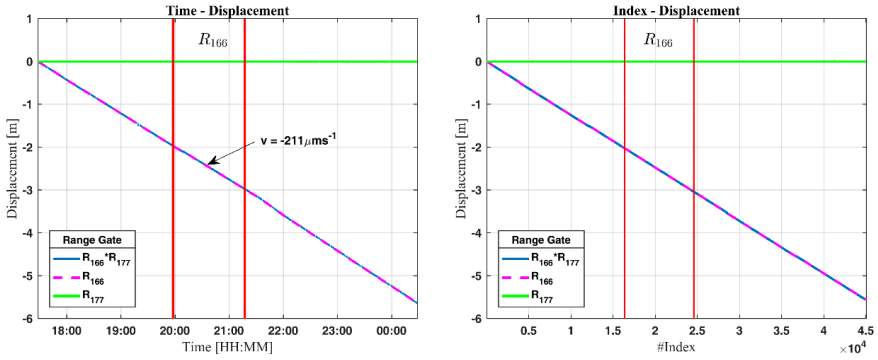

(**a**) (**b**)

Figure 10. Displacement, (**a**) measured as a function of time and (**b**) simulated as function of numerical simulation #index. The magenta line is measured displacement, the blue line is the differential measured displacement, and the green line is the displacement of the reference reflector. The red lines mark the extent of range index 166.

Figure 10a shows the measured displacement of the towed reflector, and Figure 10b shows the computed displacement. As expected, the reference reflector remains stationary while the towed reflector shows a displacement of approximately 5.61 m. The calculated velocity of the motion is −211 µm/s, which corresponds well with the theoretical speed of the winch, which is 220 µm/s. The measured displacement from the second laboratory experiment is presented for two different step increments in Figure 11.

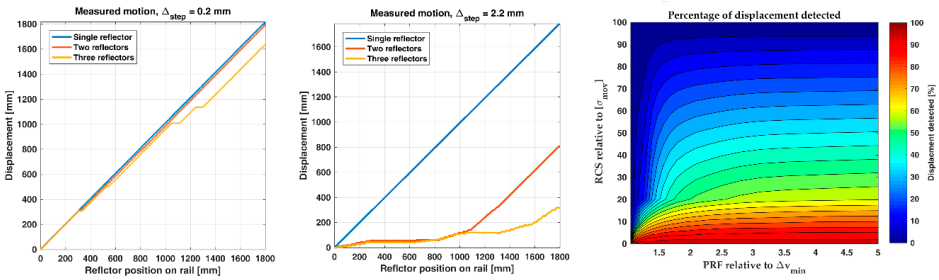

(**a**) (**b**) (**c**)

Figure 11. Displacement as a function of reflector position on the rail for step increments of (**a**) 0.2 mm (~λ/45) and (**b**) 2.2 mm (~λ/4). The blue line is the measured motion of the single reflector. The red line is the measured motion when a stationary reflector was introduced at 520 mm from the start of the rail. The yellow line is the measured motion when two stationary reflectors were introduced at 520 mm and 1170 mm from the start of the rail. (**c**) Simulated detection of displacement as a function of RCS and PRF.

Figure 11 shows the measured motion from the three laboratory experiments for two different sampling intervals. In both experiments, the reflector was moved 1800 mm. The blue line shows the single reflector displacement, and the red and yellow lines show the displacement when one and two stationary reflectors are added to the measurement scene. The data is from the same measurement, the only difference is the step-size between the measurements which is equal to a radar setup with three different PRFs. Both measurements fulfill the maximum unambiguous velocity ($V_{max} = 0.25\lambda \cdot PRF$) as can be seen from the single-reflector displacement (the blue line in Figure 11a,b). When stationary

reflectors are introduced, the displacement is partly masked. Figure 11c shows the result of a simulation where a reflector is moved past a stationary reflector. The RCS of the stationary reflector is varied from 0 to 100 times the RCS of the moved reflector, and the PRF is varied from $\lambda/4$ to $\lambda/20$. The total motion is collected in 20 range cells from the stationary reflector, and the displacement is presented as a percent of the total motion.

In Figure 12, the determined displacements from the outdoor experiment based on interferometric and differential interferometric measurements are compared.

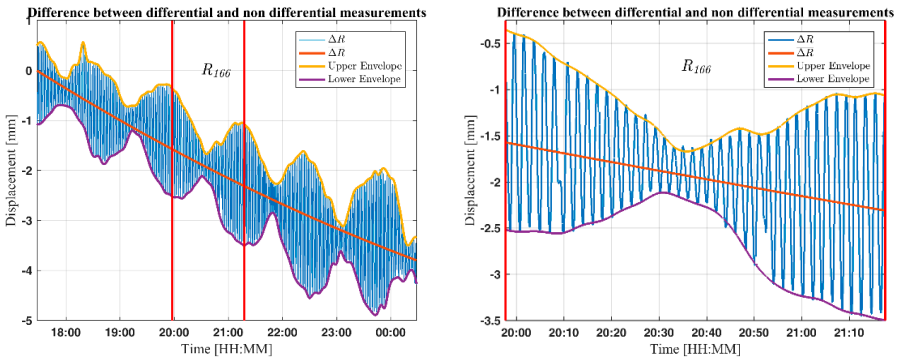

Figure 12. Difference in determined displacement using interferometric or differential interferometric measurements as a function of time. (**a**) The blue line shows the oscillations in the differential measured displacement; the red line shows the moving mean of the differential displacement. The accumulated difference in displacement between the two methods is 3.9 mm; (**b**) shows how the differential measured displacement oscillated due to constructive and destructive interference within range cell 166. The number of wavelengths per range cell corresponds to the range resolution divided by the wavelength Equation (13), which in this setup is 38 wavelengths per range cell.

Figure 12a highlights the difference between the interferometric and differential interferometric measured displacement. Most noticeable are the oscillations in the differential measurements, which reach an amplitude of approximately ± 1.5 mm, this oscillation is due to inter-reflector interference. The difference between the two methods is approximately 3.9 mm, which corresponds to 0.7‰ of the total motion. Figure 12b highlights the oscillations in the differential displacement for range index 166. The number of wavelengths per range cell corresponds to the range resolution divided by the wavelength, see Equation (13), which in this setup is 38 wavelengths per range cell.

4.5. Geometric, Environmental and Hardware Influence on Interferometric and Differential Interferometric Measurements

In this section, we assess the deviations in the interferometric and differential interferometric displacements. We analyze the effect the environment, measurement geometry and radar hardware have on the measurement accuracy.

4.6. Radio Refractivity

To compensate for the variations in the radio refractivity, an empirical model based on temperature, humidity and pressure may be used ([33]; p. 304). To compensate for atmospheric decorrelation, metrological data was downloaded from the Norwegian Metrological Institutes Station in Ås, located 2.7 km from the measurement site. During the measurements, the temperature dropped from -1.9 °C at 17:00 to -13.1 °C at 01:00 at the same time the relative air humidity increased from 26 to 81%, see Figure 13a. The pressure was not recorded but the mean air pressure was 990 mbar. This gives a

change in the refractivity index from n = 298 to n = 314 resulting in an apparent motion of approximately 1.9 mm, see Figure 13b.

By adjusting the displacement for the estimated variation in refractivity the deviation is reduced by 1.9 mm. This is an improvement of nearly 50%, even when the metrological data is not acquired locally.

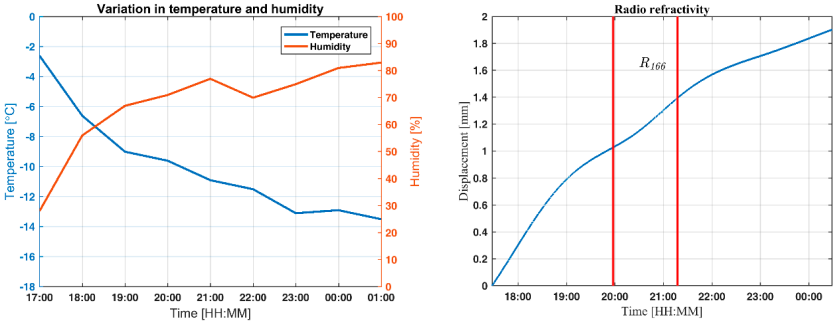

(**a**) (**b**)

Figure 13. (**a**) Air temperature and humidity as a function of time. (**b**) Variation in radio refractivity estimated from the meteorological data as a function of time. Range index 166 is indicated by the two vertical lines.

4.7. Multipath Interference

In Section 4.2, multipath interference was found to affect the amplitude of the backscatter from the reflectors. Multipath interference will also affect the phase of the received signal as shown in Figure 14.

The change in distance due to multipath interference during the measurement is estimated to be 0.35 mm.

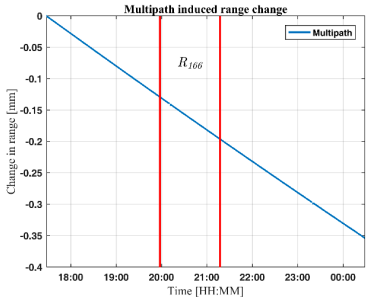

Figure 14. Multipath interference induced range variation as a function of time. The multipath interference induced a shift in range proportional to the motion of the towed reflector. Range index 166 is indicated by the two vertical lines.

4.8. Electrical Length of the Microwave Cables and Velocity Factor

Varying temperature and/or any change in the path of the electromagnetic waves will affect the accuracy of high precision radar measurements. Two types of microwave cables were used, Huber & Suhner Multiflex_141 and S_04272_B. The total length of the cables was 10.5 m, 4.5 m of Multiflex_141 and 6 m of S_04272_B. The temperature phase variation used for the two cables is Multiflex_141 = 1500 ppm and S_04272_B = 400 ppm [34]. Estimated change in electrical length of the cables used during the measurement based on the same temperature data as used in Section 4.6 is shown in Figure 15.

Applying the estimated change in electrical length of the microwave cable further reduces the difference by approximately 2 mm.

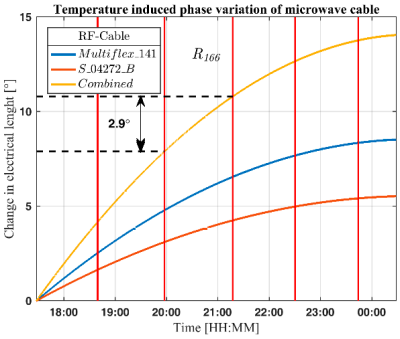

Figure 15. Estimated phase variation as a function of time during the experiment. The temperature-induced change in phase during the measurements is approximately 14°, which equals an increase in electrical length of approximately 2 mm. The 2.9° phase variation during the tow through range index 166 resulted in a 0.4 mm longer range cell.

4.9. Result of Compensation

Figure 16 sums up the combined effect of radio refractivity and change in electrical length of the microwave cable. To avoid the effect of inter-reflector interference, the moving mean of the differential displacement is used for comparison.

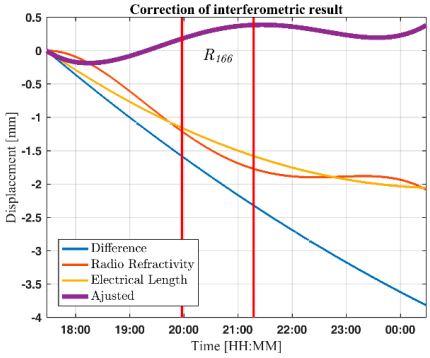

Figure 16. Displacement as a function of time. The blue line shows the difference between interferometric and moving mean of the differential interferometric displacement. The red line shows the estimated effect of the variation in radio refractivity and the yellow line shows the estimated change in electrical length of the microwave cable. The purple line shows the adjusted interferometric result i.e., the combined effect of the corrections. By applying these corrections, the deviation is reduced by approximately 96%.

In Figure 16 the blue line is the difference between the mean differential displacement and the interferometric displacement. The red line is the estimated displacement due to variation in the radio refractivity, the yellow line is the variation in distance due to the change in electrical length of the microwave cables, and the purple line shows the resulting interferometric displacement when the corrections are applied.

4.10. Summary of the Interferometric Experiment

Table 3 summarizes geometrical, environmental and electrical effects on the measurement accuracy.

Table 3. Measured and adjusted displacement per range cell in mm. The four center range cells where the motion covers the full extent of the range-cell are marked with gray color.

Range [m]	157	158	159	160	161	162	Sum all range-cells	Sum R_{158} to R_{161}
Range-index [#]	164	165	166	167	168	169		
Interferometry	927.17	1008.20	1005.94	1007.71	1007.38	602.37	5558.8	4029.23
Differential Interferometry	927.30	1007.87	1005.63	1006.98	1006.61	600.43	5554.8	4027.09
Measurement Geometry	1.96	1.94	1.93	1.91	1.89	1.88	11.51	7.67
Radio Refraction	0.10	0.15	0.25	0.37	0.38	0.65	1.90	1.15
Multipath Interference	0.036	0.061	0.061	0.067	0.067	0.062	0.35	0.26
Shadowing	3.87	3.85	3.87	3.48	3.02	2.47	20.57	14.23
Electrical Change in Cable Length	0.61	0.54	0.42	0.27	0.16	0.04	2.05	1.40
Adjusted Interferometry	-	1005.51	1003.28	1005.10	1004.89	-	-	4018.78
Adjusted Differential Interferometry	-	1002.07	999.75	1001.30	1001.43	-	-	4004.52

Note that the change in electrical length of the microwave cable only applies to the interferometric computation while shadowing only applies to the differential interferometry. The radio refractivity applies to all computations but for the differential interferometry only by a fraction varying from $^{13}/_{157}$ to $^{7}/_{162}$. Multipath interference and the measurement geometry applies to both methods. The average range cell length measured is 1004.69 mm for interferometry and 1001.13 mm for differential interferometry.

5. Discussion

The experiment shows that the accuracy of both interferometry and differential interferometry depends on the measurement geometry, variations in radio refractivity, multipath interference, interference between scatterers, and the radar hardware. In this chapter, the influence of these effects are discussed. The discussion is divided into three sections: Amplitude, phase and radar hardware. Some general advice is then given on how to minimize the impact of these effects in an operational system.

5.1. Amplitude

The amplitude data is often the first information to assess when analyzing radar measurements. Any deviations in backscattered energy from reflectors compared to what is expected from theoretical values are easily detectable. Two effects were observed, damping and oscillations. The theoretical RCS of the towed reflector is 20.4 dBsm and the theoretical RCS of the stationary reflector is 13.1 dBsm. This gives a difference in backscatter between the two reflectors of 7.3 dB, while the measured difference was approximately 21.7 dB when the towed reflector was at the far end of the rail. Three major effects may explain this difference: Multipath interference, shadowing (for details see Appendix A) and propagation loss. First, the multipath interference-induced gain of the towed reflector, which is estimated to 8 dB when the towed reflector is at the end of the rail, and the multipath interference-induced gain of the stationary reflector, which is estimated to be 3.5 dB, see Figure 8. This gives a 4.5 dB multipath interference gain. Second, the contribution from shadowing which is estimated to be 7.8 dB (see Appendix A). Third, the FSPL that is 0.7 dB. The combined total of these three effects are 13 dB. Subtracting the combined contribution from the measured value gives a difference of 8.9 dB, which agrees with the theoretical difference of 7.3 dB. The deviation of 1.6 dB might come from using uncalibrated corner reflectors, by misalignment of one or both reflectors, and inaccurate measuring of reflector and radar antenna height. The results show that the combined effect of measurement geometry, multipath interference and shadowing may give large time variations

in the backscattered energy from scatterers in the measurement scene. In a measurement scene with many moving scatterers, tracking of natural scatterers can be challenging as they may disappear and reappear depending on geometry, shadowing and motion.

The shadowing of the stationary reflector was found to be the main cause of the damping of the reflected energy. This is supported both by observing the increase in reflected energy backscattered from the reference reflector as the towed reflector was towed beyond the end of the rail, see Figure A1, and by the reflector shadowing experiment in the laboratory, see Figure A3.

The oscillations observed in the amplitude of the backscatter from the reference reflector are caused by inter-reflector interference between the two reflectors in the measurement scene. The oscillation increase as the towed reflector gets closer to the stationary reflector, see Figure 9a. The interference is visible in both Figure 9a,b, however, the amplitude of the oscillations is higher for the stationary reflector than for the towed reflector. This is due to the mutual size difference, i.e., the largest reflector has a greater influence on the small reflector than the small reflector on the large reflector. Maximum constructive interference between two reflectors occurs when the mutual distance, ΔR, is equal to integer multiples of the wavelength of the transmitted signal and maximum destructive interference that occurs when the mutual distance is equal to integer multiples of half the wavelength. The amplitude of the interference will follow a sine cardinal pattern due to the Fourier transform when going from the time domain to frequency domain. The maximum and minimum amplitude will occur when the two reflectors are in the same range cell, see Figure 9. This shows that all scatterers within the measurement scene may affect each other and the magnitude of the interference depends on the reflected energy of the scatterers according to the exponent in Equation (13).

5.2. Phase

As discussed in the previous section, the effect of radio refractivity, multipath interference, inter-reflector interference, and shadowing affects the amplitude. In addition, it affects the phase of the reflections, see Figures 13–15.

The variation in radio refractivity during the measurements was estimated based on meteorological data and was found to contribute to almost 50% of the deviation between the interferometric and the differential interferometric displacement. The temporal sampling rate of the meteorological data was 1 h. This gives a relatively large uncertainty in the computations. Another factor adding to the uncertainty is the distance between the radar site and the meteorological station that is 2.7 km. However, we show that the corrections of radio refractivity improve the results. The influence of the variation in radio refractivity increases with distance; hence, in real-life setups the contribution may be substantially higher.

The effect of multipath interference depends on the geometry of the measurement setup and since the height of the antennas and reflectors were recorded manually, a fair amount of tolerance in the result is to be expected. The change of 0.35 mm for the 6 m tow of the reflector in this setup might seem to be insignificant, but given another setup geometry, the effect might be significantly higher. The effect of multipath interference should therefore always be considered as a source of measurement error in high-precision measurements. The estimation of multipath interference is a challenging task in real-life measurements due to temporal variation in the reflection coefficient as the backscatter depends on surface roughness, moisture and texture [35].

The effect of shadowing was, based on the laboratory measurements, found to contribute to 14.2 mm of the measured displacement of the differential result. The laboratory experiment was based on the measured geometry of the field experiment and some uncertainty is expected in the result. The effect of shadowing was an unintended result of an unfortunate measurement setup and is only added to explain the measured deviations. In some remote sensing scenarios, shadowing might be unavoidable, leading to low coherence and consequently, could be detrimental for the monitoring [24].

The laboratory experiment shows that inter-reflector interference can mask the motion. To avoid this, the backscatter of the moving object should be higher than the backscatter of the stationary object,

see Figure 11c. This follows directly from Equation (13), which states that the energy backscatter of a range cell is the coherent sum of all the scatterers within the range cell. In GB-SAR, this applies both in the down and cross range [24] (Figure 7b). This result indicates that it is beneficial to introduce reflectors to the measurement scene to follow the motion of point objects. The introduction of a reflector is artificial, but it can be viewed without loss of generality as natural stationary clutter or infrastructure like rockfall catch fences in a real-life measurement scene either in the mainlobe or in the sidelobe. This indicated that in a measurement scene without a distinct scatterer, care should be exercised when analyzing the displacement.

The variation in radio refractivity applies to both interferometry and differential interferometry, but for differential interferometry only by a fraction equal to the length between the reflectors. The multipath interference applies to both interferometry and differential interferometry.

5.3. Radar Hardware

A part of the difference between the interferometric and differential interferometric results may be explained by variations in the radar hardware. If the variations due to the radar hardware can be measured or predicted, the measurements can be corrected. The main source affecting the modulation bandwidth is the accuracy of the reference clock of the signal generator. Inside the radar used during this experiment there are two oscillators, one for the local oscillator, one for the sweep generator (DDS). Fluctuations in any of these oscillators will affect the measurements. The total uncertainty of the DDS reference oscillator is used in the GB-InRAR $\pm$23 ppm, disregarding any aging effects. This may lead to variations in the transmitted bandwidth. Due to programming technicalities, the effective bandwidth from the DDS multiplier chain was 149,912,000 MHz. This will give a maximum decrease in range cell length by approximately 0.6 mm, giving a total of 3.5 mm for the 6 m tow of the reflector further reducing the deviation between the measured and computed movement. This effect is independent of distance and applies to all range cells.

The temperature-induced change in electrical length of the microwave cables contributed to a variation in range, which is visible in the measurements. The total effect of this change was approximately 2 mm. This estimate is based on meteorological data from a station 2.7 km away from the radar, leading to uncertainties in the calculations. The estimated change in electrical length of the microwave cables are based on coarse values from data sheets; a fair amount of tolerance in the calculations are expected. The temperature–phase relationship of a microwave cable is complex, and it is usually measured and not numerically modelled. To minimize error, the microwave cables used should be temperature cycled to get the correct temperature–phase variation.

5.4. Measured Displacement

The measured difference in displacement between interferometry and the mean differential motion is approximately 3.9 mm, see Figure 12a. The mean displacement was used for the differential interferometric displacement to avoid the inter-reflector interference to influence the interferometric result. The average range cell size was estimated to be 1007.3 mm for interferometry and 1006.8 mm for differential interferometry. After adjusting the interferometric displacement for measurement geometry, variation in radio refractivity, multipath interference, change in electric length of the microwave cable, and actual bandwidth, the average range-cell size was reduced to 1004.1 mm. The differential displacement was adjusted for measurement geometry, multipath interference, shadowing, and actual bandwidth, resulting in an average range cell size of 1000.5 mm. The major part of the difference between the two methods are believed to come from inaccuracy in the data used to calculate the variation in radio refractivity and change in electric length of the microwave cable as the temperature and humidity data was not recorded locally. There is some measurement uncertainty with the geometry of the measurement setup, but this will affect both methods equally except for the shadowing, which only applies to the differential method.

The differential displacement is closer to the theoretical range cell length of 1 m, but this is the mean motion. The inter-reflector interference displayed in Figure 12a shows a range variation of approximately ± 1.5 mm, which is a product of the measurement setup and not a physical motion. This effect will diminish by increasing the distance between the reflectors, but care should be exercised when placing a reference reflector.

5.5. Minimizing the Influence of Geometic, Environmental, and Radar Hardware Effects in Operational Monitoring

In this section, we summarize the findings and give general advice on how to avoid or reduce the impact of the effects presented in this chapter.

The impact of radio refractivity is frequency dependent and it is stated in Reference [14] that the longest radar waves possible should be used to minimize the effect of atmospheric variations. Using a lower frequency has the inherent consequence of a larger antenna to achieve the same beamwidth as the beamwidth is approximately given as λ/L, where L is the physical size of the antenna ([22]; p. 6.8). Applying meteorological data collected locally has been shown in a number of studies to be an efficient way to compensate for atmospheric decorrelation [8,13,17–20].

To minimize the effect of multipath interference, the vertical part of the antenna lobe should not illuminate the ground. This can be controlled by adjusting the elevation angle of the antenna and by using an antenna with a narrow elevation beam. If the installation geometry prohibits this, vertical polarization is preferable as it generates less multipath interference than horizontal polarization. This can be seen from Figure 1 where the magnitude of the reflection coefficient for VV-polarization is significantly lower than for HH-polarization. Hence, multipath interference is less at VV-polarization than at HH-polarization. This was also one of the main findings in Reference [21]. Another way of reducing multipath interference is by adding shielding of the antennas, preventing the radar waves from illuminating the reflective surface as presented in Reference [21]. They state in their experiment that this greatly reduced the problem, but it did not eliminate the interference. They also recommend installing the radar at an elevated area if possible. If none of the above measures is possible, this study has shown that the effect of multipath interference can be reduced by applying corrections based on analysis of the measurement geometry and the reflective surface.

Unless the backscatter from the object or surface in motion is stronger than the backscatter from the surroundings, inter-reflector interference can mask the motion as shown in Figure 11. One way to avoid this effect is by introducing an artificial reflector. The laboratory experiment also showed that a high PRF partly helps to resolve the problem. Both the outdoor and laboratory experiments showed that the interference between strong reflections where one object is in motion results in oscillations in the amplitude of the backscatter. This indicated that care should be taken when measuring objects in strong clutter, so that the motion of the monitored object or area is not suppressed by backscatter from stationary clutter. The general solution is to use a large antenna with a narrow beam to reduce the illuminated area and reduce the range cell size i.e., use a wideband radar.

The reference oscillator should be of high quality and preferably both temperature and voltage compensated.

The temperature-induced phase shift in the microwave cables may be reduced by keeping the cables as short as possible and by using high performance cables with low a temperature–phase coefficient. In Reference [23] it is suggested to use active temperature stabilization of the cables to minimize the phase–temperature variation. They also recommend using PTFE-free cables for operating temperatures below 22 °C. One solution to monitor the major variations in phase due to radar hardware is to measure the phase of the antenna cross-talk and to adjust the measurements accordingly.

6. Conclusions

A GB-InRAR system is used for experimental interferometric and differential interferometric measurement experiments in the field and laboratory with a moving trihedral corner reflector.

A theoretical model is developed to asses measurement uncertainties for the geometry of the measurement setup, atmospheric effects i.e., radio refractivity and the effect of ground reflections i.e., multipath interference, radar target interference and the radar hardware.

It is shown that major deviations between interferometric and differential interferometric calculated displacement can be explained by variations in environmental and geometrical effects. The accuracy of interferometry can be comparable to the differential accuracy when adjusted for environmental variations. For the analyzed experiment, the major contributing environmental effects are radio refractivity and temperature-induced change in electrical length of the microwave cables. The major geometrical effects are multipath interference and inter-reflector interference.

The experiments show inter-reflector interference, which for the differential method resulted in oscillations in measured displacement. The amplitude of these oscillations increased inversely with distance peaking when they were in the same range cell. It is shown that the motion can be masked when the backscatter from the stationary object is equal or higher than the backscatter from the moving object. It was also shown that the effect of inter-reflector interference could be reduced by using a high PRF.

The accuracy of both methods can be improved by adjusting for offsets in the radar hardware. The temperature-induced change in the electrical length of the microwave cables can be significant, and it should be considered separately to avoid mixing the effect with the radio refractivity, which is also influenced by variation in temperature.

The results derived from the experiment verify that the GB-InRAR can detect and monitor small displacements. The analysis suggests that differential interferometry is close to unaffected by radio refractivity but vulnerable to inter-reflector interference.

The compensated average interferometric displacement is within 4‰ of the theoretical range cell size while the compensated average differential displacement is within 1‰ of the theoretical range cell size. Validation of the experiments is based on general radar theory, and the calculations and results should be valid for other radar systems.

Author Contributions: Conceptualization: R.G.; Data Curation: R.G.; Formal Analysis: R.G.; Investigation: R.G.; Methodology: R.G., R.N., and C.R.D.; Software: R.G.; Supervision: R.N. and C.R.D.; Visualization: R.G.; Writing—Original Draft: R.G.; Writing—Review & Editing: R.G., R.N., and C.R.D.

Funding: The work was supported by the Research Council of Norway.

Conflicts of Interest: The authors declare no conflict of interest.

Appendix A

The analysis of the reflector shadowing is included to explain some of the amplitude and phase deviations found in the outdoor experiment. Please note that the shadowing was an unintended effect of the measurement setup, found when analyzing the data after the measurement campaign was finished.

Appendix A.1. Amplitude Attenuation as a Result of Reflector Shadowing

To assess whether the damping of the amplitude of the stationary reflector was caused by shadowing, the measurement geometry was analyzed. When the towed reflector is at the near end of the rail it is approximately 14 cm below the Line-Of-Sight (LOS) to the reference reflector while at the far end the towed reflector is approximately 13 cm above the LOS to the reference reflector. This observation is supported by viewing the amplitude of the reflection from the reference reflector before and after the towed reflector was towed off the far end of the rail. The magnitude of the reflection from the reference reflector, when the towed reflector is located at the far end of the rail, is 7 dB below the magnitude of the reflection from the reference reflector after the towed reflector has fallen of the far end of the rail, see Figure A1.

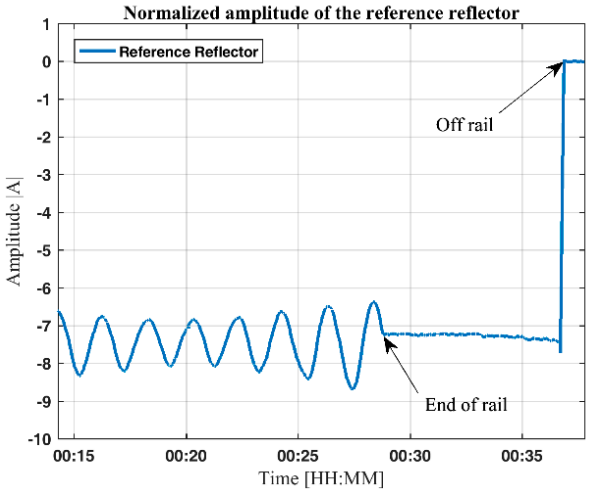

Figure A1. Amplitude as a function of time for the stationary reflector. The amplitude increases by approximately 7 dB when the towed reflector falls off the far end of the rail, supporting the theory that the towed reflector shadows the reference reflector.

Modelling the effect of shadowing and multiple reflections between the two reflectors is a non-trivial task. Instead, an experiment was conducted in the laboratory using two reflectors, keeping one reflector stationary while moving the other reflector in height behind it. Initially, it begun moving the reflector 30% of its height below the stationary reflector and then it moved it step-by-step until it was 30% of its height above the stationary reflector, see Figure A2. This ensured a free view of the moved reflector at the beginning and end of the motion. The two reflectors were aligned radially to the radar ensuring a 100% shadowing in the center of the motion. The resulting amplitude of the backscatter from the two reflectors from the experiment is shown in Figure A3.

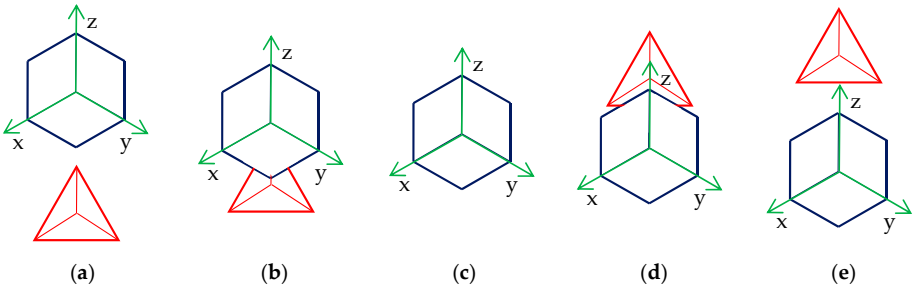

Figure A2. Illustration of how the reflector was moved in the laboratory experiment. (**a**–**e**) illustrates how the triangular trihedral corner reflector with red color is shadowed by the stationary blue square trihedral corner reflector. The triangular corner reflector was moved from 30% of its height below the stationary square corner reflector to 30% of its height above.

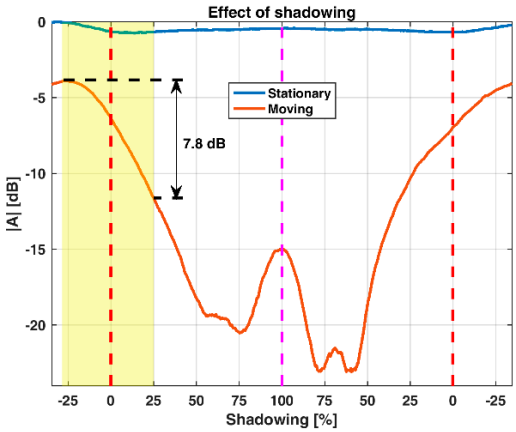

Figure A3. Amplitude as a function of shading. One reflector was moved from approximately 30% of its height below the stationary reflector, right-hand side of the figure, to approximately 30% of its height above the stationary reflector on the left-hand side of the figure. In the center, the view of the rear reflector is blocked by the front reflector. The yellow patch marks the shadowing corresponding to the measurements. The amplitude of the reflection from the shadowed reflector falls by 7.8 dB as the radar's view of the reflector is obstructed by the stationary reflector. The reason why the reflected pattern is not symmetrical is due to the geometry of the triangular reflector i.e., the pointed top versus the flat bottom, see Figure A2b versus Figure A2d.

In Figure A3, the degree of shadowing corresponding to the measurement is marked by the horizontal black lines, indicating a decrease in reflected energy from the shadowed reflector of 7.8 dB. It is interesting to note that the decrease in energy starts even before the reference reflector is physically shaded. This is believed to be caused by higher order effects like edge diffraction and destructive interference between the two reflectors. This experiment supports the assumption that the decreasing backscatter from the stationary reflector comes from shadowing by the towed reflector. Likewise, the jump in energy backscattered from the reference reflector when the towed reflector falls off the rail comes from shadowing.

Appendix A.2. Phase Shift as A Result of Reflector Shadowing

The increased shadowing of the reference reflector has another effect than the decrease in reflected energy as shown in Figure A1. As the LOS of the reference reflector is obstructed, the phase-center of the reference reflector is moved away from the radar as shown in Figure A4.

Figure A4 reveals how the phase of the backscattered energy of the reference reflector is shifted as the towed reflector obstructs the radar's view of the reference reflector. In the differentially processed data, this will look like the reference reflector is moving away from the radar. The total shift is in the order of 141°, which at the operating frequency of the radar equals approximately 20.6 mm. For the differential interferometric measurements, this will result in a motion which is approximately 3.4 mm per range cell.

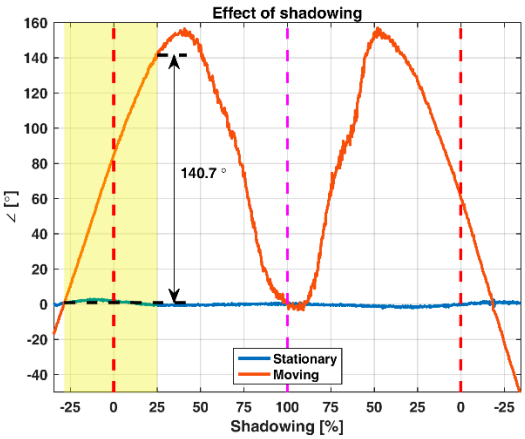

Figure A4. Measured phase as a function of shadowing of the reference reflector. As the obstruction of the reference reflector increases, the phase of the reflected energy is shifted close to 141° away from the radar. This results in an increased measured range of the reference reflector of 20.6 mm for the tow along the rail.

References

1. Mecatti, D.; Macaluso, G.; Barucci, A.; Noferini, L.; Pieraccini, M.; Atzeni, C. Monitoring open-pit quarries by interferometric radar for safety purposes. In Proceedings of the 7th European Radar Conference, Paris, France, 30 September–1 October 2010.
2. Di Pasquale, A.; Nico, G.; Pitullo, A.; Prezioso, G. Monitoring strategies of earth dams by ground-based radar interferometry: How to extract useful information for seismic risk assessment. *Sensors* **2018**, *18*, 244. [CrossRef] [PubMed]
3. Lukin, K.; Anatoliy, M.; Palamarchuk, V.P.; Vyplavin, P.L.; Kozhan, E.; Lukin, S. Monitoring of St. Sophia Cathedral interior using Ka-band Ground Based Noise Waveform SAR. In Proceedings of the 2009 European Radar Conference (EuRAD), Rome, Italy, 30 September–2 October 2009; pp. 215–217, ISBN 9781424447473.
4. Liu, X.; Lu, Z.; Yang, W.; Huang, M.; Tong, X. Dynamic monitoring and vibration analysis of ancient bridges by ground-based microwave interferometry and the ESMD method. *Remote Sens.* **2018**, *10*, 770. [CrossRef]
5. Luzi, G.; Crosetto, M.; Fernández, E. Radar interferometry for monitoring the vibration characteristics of buildings and civil structures: Recent case studies in Spain. *Sensors* **2017**, *17*, 669. [CrossRef] [PubMed]
6. Gundersen, R.; Norland, R.; Denby Rolstad, C. Ground-Based Differential interferometric radar monitoring of unstable mountain blocks in a coastal environment. *Remote Sens.* **2018**, *10*, 914. [CrossRef]
7. Norland, R. Differential Interferometric Radar for Mountain Rock Slide Hazard Monitoring. In Proceedings of the 2006 IEEE International Symposium on Geoscience and Remote Sensing, Denver, CO, USA, 31 July–4 August 2006; pp. 3293–3296. [CrossRef]
8. Norland, R. Improving Interferometric Radar Measurement Accuracy using local Meteorological Data. In Proceedings of the IGARSS 2007 IEEE International Geoscience and Remote Sensing Symposium, Barcelona, Spain, 23–28 July 2007; pp. 3293–3296. [CrossRef]
9. Norland, R.; Gundersen, R. Use of radar for landslide hazard monitoring. In *Landslides and Avalanches: ICFL 2005 Norway: Proceedings of the 11th International Conference and Field Trip on Landslides, Norway, 1–10 September 2005*; Taylor & Francis: London, UK, 2005.
10. Luzi, G.; Pieraccini, M.; Mecatti, D.; Noferini, L.; Macaluso, G.; Galaro, A.; Atzeni, C. Advances in ground-based microwave interferometry for landslide survey: A case study. *Int. J. Remote Sens.* **2006**, *27*, 2331–2350. [CrossRef]
11. Rolstad, C.; Norland, R. Ground-based interferometric radar for velocity and calving-rate measurements of the tidewater glacier at Kronebreen, Svalbard. *Ann. Glaciol.* **2009**, *50*, 47–54. [CrossRef]

12. Gundersen, R.; Norland, R.; Denby Rolstad, C. Monitoring glacier flow with ground-based interferometric radar in Ny-Ålesund, Svalbard. *Polar Res.* **2018**, under review.
13. Luzi, G.; Dematteis, N.; Zucca, F.; Monserrat, O.; Giordan, D.; Lopez Moreno, J. Terrestrial radar interferometry to monitor glaciers with complex atmospheric screen. In Proceedings of the 2018 International Geoscience and Remote Sensing Symposium, Valencia, Spain, 22–27 July 2018; pp. 6243–6246.
14. Zebker, H.; Rosen, P.; Hensley, S. Atmospheric effects in interferometric synthetic aperture radar surface deformation and topographic maps. *J. Geophys. Res.* **1997**, *102*, 7547–7563. [CrossRef]
15. Ferretti, A.; Prati, C.; Rocca, F. Nonlinear Subsidence Rate Estimation Using permanent scatterers in differential SAR interferometry. *IEEE Trans. Geosci. Remote Sens.* **2000**, *38*, 2202–2212. [CrossRef]
16. Kempes, B. *Radar Interferometry, Persistent Scatterer Technique*; Springer: Munich, Germany, 2006; ISBN 9781402045769.
17. Luzi, G.; Pieraccini, M.; Mecatti, D.; Noferini, L.; Guidi, G.; Moia, F.; Atzeni, C. Ground-based radar interferometry for landslides monitoring: Atmospheric and instrumental decorrelation sources on experimental data. *IEEE Trans. Geosci. Remote Sens.* **2004**, *42*, 2454–2466. [CrossRef]
18. Noferini, L.; Pieraccini, M.; Mecatti, D.; Luzi, G.; Atzeni, C.; Tamburini, A.; Broccolato, M. Permanent scatterers analysis for atmospheric correction in ground-based SAR interferometry. *IEEE Trans. Geosci. Remote Sens.* **2005**, *43*, 1459–1471. [CrossRef]
19. Pipia, L.; Fàbregas, X.; Aguasca, A.; López-Martínez, C. Atmospheric artifact compensation in ground-based DInSAR applications. *IEEE Geosci. Remote Sens. Lett.* **2008**, *5*, 88–92. [CrossRef]
20. Monti Guarnieri, A.; Iannini, L.; Giudici, D. Atmospheric phase screen in ground-based radar: Statistics and compensation. *IEEE Geosci. Remote Sens. Lett.* **2011**, *8*, 537–541. [CrossRef]
21. Lucas, C.; Leinss, S.; Bühler, Y.; Marino, A.; Hajnsek, I. Multipath interferences in ground-based radar data: A case study. *Remote Sens.* **2017**, *9*, 1260. [CrossRef]
22. Skolnik, M. (Ed.) *Radar Handbook*, 2nd ed.; McGraw-Hill Education: Boston, MA, USA, 1990; p. 1200, ISBN 9780070579132.
23. Czuba, K.; Sikora, D. Temperature stability of coaxial cables. *ACTA Phys. Pol.* **2011**, *119*, 553–557. [CrossRef]
24. Frukacz, M.; Wieser, A. On the impact of rockfall catch fences on ground-based radar interferometry. *Landslides* **2017**, *14*, 1431–1440. [CrossRef]
25. Frukacz, M.; Wieser, A. Terrestrial radar interferometry with objects observed through protection fences. In Proceedings of the 18 Internationaler Ingenieurvermessungskurs Graz, Graz, Austria, 25–29 April 2017.
26. Gurgel, K.; Schlick, T. *Remarks on Signal Processing in HF Radars Using FMCW Modulation*; International Radar Symposium IRS: Hamburg, Germany, 2009.
27. Levanon, N. *Radar Principles*; John Wiley & Sons: Tel-Aviv, Israel, 1988; ISBN 0471858811.
28. Stiles, W.; Ulaby, F. *Dielectric Properties of Snow*; University of Kansas: Lawrence, KS, USA, 1980.
29. Frolov, A.D.; Macheret, Y.Y. On dielectric properties of dry and wet snow. *Hydrol. Process.* **1999**, *13*, 1755–1760. [CrossRef]
30. Mahafza, B.R. *Radar Systems & Analysis and Design Using Matlab*; Chapman & Hall: Huntsville, AL, USA, 2000; p. 772, ISBN 978-158-488-182-7.
31. Pozar, D. *Microwave Engineering*, 4th ed.; John Wiley & Sons Inc.: Amherst, MA, USA, 2012; p. 732, ISBN 9780470631553.
32. ITU. *RECOMMENDATION ITU-R P.525-3, Calculation of Free-Space Attenuation*; International Telecommunication Union: Geneva, Switzerland, 2016.
33. Morchin, W. *Radar Engineer's Sourcebook*; Artech House Publisher: Northwood, MA, USA, 1992; p. 496, ISBN 9780890065594.
34. Fosli, E. (Bredengen AS, Oslo, Norway). Personal communication, 2018.
35. Ulaby, F.; Batlivala, P.; Dobson, M. Microwave backscatter dependence on surface roughness, soil moisture, and soil texture: Part I-bare soil. *IEEE Trans. Geosci. Electron.* **1978**, *16*, 286–295. [CrossRef]

Paper Ⅱ

Ground-Based Differential Interferometric Radar Monitoring of Unstable Mountain Blocks in a Coastal environment.

Gundersen R, Norland R, Denby Rolstad C, Remote Sensing, vol. 16 no. 6, **2018**. https://doi.org/10.3390/rs10060914

remote sensing

MDPI

Article

Ground-Based Differential Interferometric Radar Monitoring of Unstable Mountain Blocks in a Coastal Environment

Rune Gundersen [1,2,*], Richard Norland [2] and Cecilie Rolstad Denby [1]

[1] Faculty of Science and Technology, Norwegian University of Life Sciences, 1433 Ås, Norway; cecilie.rolstad.denby@nmbu.no

[2] ISPAS AS, P.O.B. 506, 1522 Moss, Norway; richard.norland@ispas.no

* Correspondence: rune.gundersen@nmbu.no; Tel.: +47-9055-8418

Received: 27 April 2018; Accepted: 5 June 2018; Published: 9 June 2018

Abstract: In this paper, we present the results of eight years of continuous monitoring with a ground-based, interferometric, real-aperture radar of two unstable mountain blocks at Tafjord on the western coast of Norway. A real-time, interferometric, ground-based radar has the capability to provide high accuracy range measurements by using the phase of the transmitted signal, thus achieving sub-millimeter accuracy when a sufficient signal-to-noise level is present. The main challenge with long term monitoring is the variations in radio refractivity caused by changes in the atmosphere. The range variations caused by refractive changes in the atmosphere are corrected using meteorological data. We use triangular corner reflectors as references to improve the signal-to-clutter ratio and improve the accuracy of the measurements. We have also shown that by using differential interferometry, a significant part of the variation caused by radio refractivity variations is removed. The overall reduction in path length variation when using differential interferometry varies from 27 to 164 times depending on the radar-to-reflector path length. The measurements reveal cyclic seasonal variations, which are coherent with air temperature. The results show that radar measurements are as accurate as data from in situ instruments like extensometers and crack meters, making it possible to monitor inaccessible areas. The total measured displacement is between 1.2 mm and 4.7 mm for the two monitored mountain blocks.

Keywords: interferometry; Remote Sensing by Radar; monitoring

1. Introduction

High precipitation, erosion, and temperature variation or extreme stresses from earthquakes can trigger rockslides [1]. In Norway, global warming is leading to increased precipitation and wind, and a higher frequency of extreme weather conditions. It is reasonable to expect that a wetter climate with more frequent events of high precipitation will decrease rock stability.

The Norwegian Water Resource and Energy Directorate (NVE) is the national body responsible for flood and landslide warnings in Norway. Geologists from the NVE have identified two potentially unstable blocks at the Hegguraksla Mountain above the fjord Tafjorden on the west coast of Norway, see Figure 1. Each of these blocks could potentially create a flood wave if one of them should fall into the fjord [2]. The volume of each of the blocks is estimated to be between 1 and 2 million m^3 [2]. The first block is at an elevation of 500 m to 700 m above mean sea level (AMSL), and the second at an elevation from 500 m to 840 m AMSL. The lower block has a back-wall crack at about 70° and a horizontal crack at the base. From the geological analysis, main motion of the lower block is in the vertical plane downwards. Additionally, the block has a counter clockwise motion moving outwards

at the base and inwards at the top. There is some uncertainty regarding the movements of the upper block, but it is likely to be moving outward at the base (away from the mountain), while the top has a backwards rotation that leads to vertical motion with a horizontal component. For a detailed analysis of the motion of these two instabilities, see [3] (pp. 127–131).

This is in the same area where in the year 1934 roughly 3 million m^3 of rock fell into the fjord below. The rock fell from a height of about 730 m, creating a wave that reached a height of more than 60 m. The wave followed the fjord in both directions with disastrous consequences to the settlements along the fjord. The height of the wave front is believed to have been about 15–16 m when it hit the nearby settlements, and about 40 people were killed. This was one of Norway's worst natural disasters in the 20th century. This incident shows the need for real-time monitoring with the ability to give early warnings of geohazards to reduce the consequences to a minimum.

As part of the NVE-managed monitoring program of the Hegguraksla Mountain, see Figure 1, the company ISPAS has gained almost 15 years of experience with radar monitoring of this mountainside. During this period, we have tested two different radars and improved the measurement setup and tracking algorithms. The first measurements were made using a stepped frequency radar in October 2003. As reference, we used a one-square-meter, flat aluminum plate mounted on a tripod located at the lower unstable mountain block. The stability and fine alignment of the reflector proved to be difficult, and the flat plate was considered too hard to use without a firm mounting structure. The flat plate reflector has a narrow reflection pattern of approximately 1°, requiring a fine alignment of less than 0.5° in both azimuth and elevation. In addition, the data acquisition time of the stepped frequency radar was approximately 10 min, which was due to the instability of the reflector being too slow to get stable measurement results. In the summer of 2004, the measurements were repeated using a Frequency Modulated Continuous (FMCW) radar with a data acquisition time of 50 msec. This time, we used a trihedral corner reflector firmly mounted onto the unstable mountain block as reference. This combination of a stable reference reflector and short acquisition time gave stable measurement results. Based on the results from these two measurement campaigns, a permanent monitoring system was installed early in 2006. In 2011, the data acquisition and processing unit of the radar was upgraded to its current specification. To our knowledge, this is the world's first permanent installation of differential interferometric radar monitoring mountain slides [4,5].

Many studies have been published showing the application of ground-based interferometric synthetic aperture radar (GB-InSAR) for monitoring of rock and slope instabilities. Few studies have been published on the application of the ground-based, interferometric real-aperture radar [4–6]. The obvious difference between the two radar-systems is the GBInSAR's ability to map an area, a capability the real-aperture radar lacks. In this study, we present results from the monitoring of two mountain blocks with reference reflectors. For monitoring of fixed points, reference reflectors will give a high measurement accuracy independent of the weather conditions. Another difference between the two radar-systems is the measurement frequency. A GBInSAR typically uses tens of minutes to measure a scene, due to the motion of the antenna, while a real-aperture radar can measure multiple times per minute. A high measurement frequency is essential in real-life measurements due to changing weather conditions; otherwise, phase unwrapping can be challenging. The third difference between the two radar-systems is the cost of the system and the lifetime maintenance cost. As there are no moving parts in a real-aperture radar, the maintenance intervals are long and costs are low.

We use a ground-based FMCW radar with fixed antennas. Portable versions of the radar have been used to measure landslides and glacier movements [6]. The all-weather capability of the radar makes it a natural instrument for real-time monitoring of potential life-threatening natural events.

The radar is located in the small village of Fjørå 3 km from mount Hegguraksla (see Figure 1).

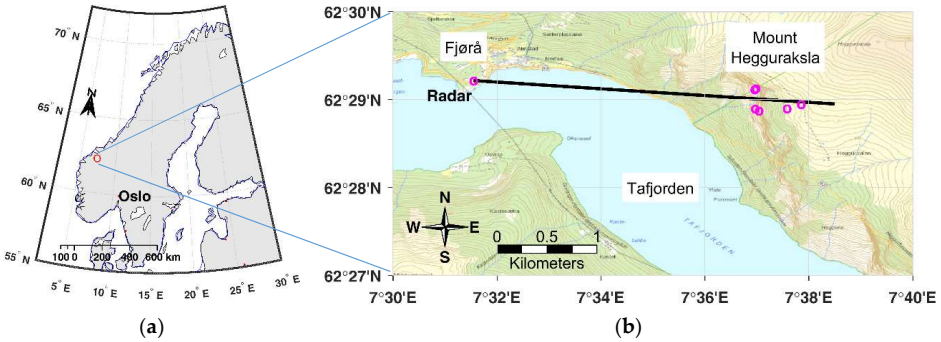

Figure 1. Two maps showing the location of the radar. (**a**) Overview map showing where in Norway the radar is located. (**b**) Shows a detailed map of the studied area. The circle to the left marks the location of the radar, and the 6 circles to the right marks the monitored mountain area. The black line marks the pointing direction of the radar.

We have continuously monitored two unstable mountain blocks from 2006 to 2018. This has given us a unique insight into the problems associated with real-time monitoring of sub-millimeter displacements under changing weather conditions. The climate on the west coast of Norway is wet and mild despite its northern latitude.

Precipitation, especially wet snow or sleet, has a strong impact on the attenuation of the electromagnetic waves. Reflectors are used to ensure that the radar system remains operational during changing weather conditions. The backscattered energy from the reflectors are between 15 dB and 30 dB higher than the backscattered energy from the mountain. This makes the reflectors stand out from the mountain and makes the monitoring system more resistant to weather-caused attenuation of the electromagnetic waves.

The aim of this study is to determine:

- displacements of the two mountain blocks
- improvement of accuracy using differential interferometry
- the influence of cycles in weather and atmospheric conditions on measurement accuracy.

To answer these questions, we first describe the measured area and the theory influencing the accuracy of the measurements. We then present the measurement setup and our results, and compare our results to in situ geotechnical instruments.

2. Installation of Permanent Monitoring System

The geologists at the NVE have identified two blocks in the mountainside as potentially unstable: one at a height of 740 m and one at a height of 840 m, subsequently referred to as Site 1 and Site 2, respectively. We have installed triangular corner reflectors at both unstable blocks. In addition, we have installed triangular corner reflectors close to both blocks, well away from the fault, serving as reference for differential measurements. Additionally, we have two triangular corner reflectors at the top of the mountain serving as reference for Site 1 and Site 2. These two reflectors are at a height of 1000 m and will be referred to as Site 3. All six triangular trihedral reflectors have a short side length of 1 m, which corresponds to a radar cross section of 36.2 dBsm at 9.65 GHz see Equation (10). The trihedrals give a reflection within 3 dB of its maximum value over an angle of the incident field close to $\pm 17^{\circ}$. The wide opening of the reflection pattern from the trihedral makes it the natural choice for use in monitoring systems involving movement, because the reflector still has a predictable backscatter even when severely dislocated or tilted.

The radar was installed on the second floor of an abandoned factory in Fjørå. The transmitting and receiving antennas are located 4.6 m apart, and approximately 8 m AMSL.

The distance from the radar to the three sites ranges from 2.9 km to 3.4 km, which gives an elevation angle between 14.5° and 16.9°. The setup is illustrated in Figure 2.

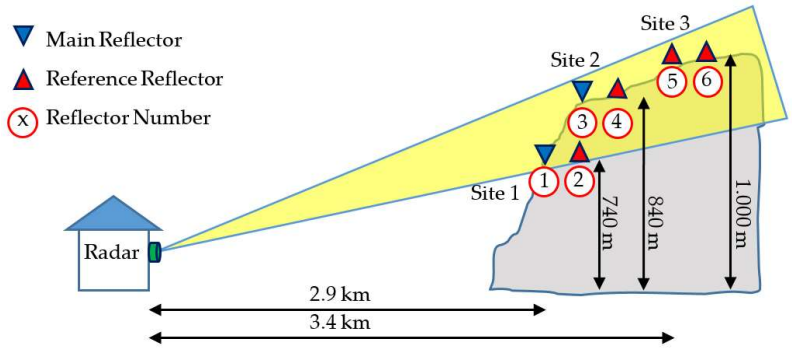

Figure 2. Illustration of the measurement setup at Hegguraksla. There are three sites in the mountain with two reflectors at each. The numbering of the six reflectors is indicated below each reflector. The radar is located roughly 3 km from the mountain. The triangular corner reflectors are located from 740 to 1000 m AMSL.

We have estimated the angle between the assumed direction of motion of the blocks at Sites 1 and 2 and the radial direction of the radar to be approximately 31°. Consequently, the radar will underestimate the motion by approximately 15%. Between 1.5 km and 2 km of the path from the radar to the reflectors is over the fjord, i.e., saltwater. The longest path over water is to Site 1. An image of the mountain and a close-up image of Site 1 is presented in Figure 3.

Figure 3. (**a**) Hegguraksla Mountain viewed from Fjørå where the radar is located. The three areas (Sites 1–3) are marked with white circles. (**b**) is a close-up picture of Site 1, showing the vertical fault and the location of reflector 1 and 2. Reflector 1 is the main reflector, and 2 is the reference reflector. The white arrow indicates the anticipated motional direction of the block.

The technical specifications of the radar are listed in Table 1.

Table 1. Key radar parameters.

FMCW Radar Parameters	Value
Frequency, fc [GHz]	9.65
Bandwidth, BW [MHz]	300
Range Resolution, ΔR [m]	0.5
Pulse Repetition Frequency, PRF [Hz]	1/60
Wave Length, λ [mm]	31.1
Antenna Gain [dB]	24
RCS of the Reflectors, [dBsm] @ 9.65 GHz	36.2

3. Meteorological Influence on Interferometric Measurements

It is stated that the accuracy of interferometric measuring is limited by the variation in radio refractivity [7]. The propagation velocity of the electromagnetic waves through a medium is influenced by the physical properties of the medium. The variation is defined as [8]:

$$\vec{n} \equiv \frac{c_0}{v} = \sqrt{\varepsilon\mu}, \tag{1}$$

in which $\vec{n}$ is the refractive index, c_0 is the speed of light in vacuum, v is the actual velocity, ε is the permittivity, and μ is the permeability. Since the change in $\vec{n}$ is close to unity, it is usually used in its scaled-up version $N = (n - 1) \times 10^6$.

The variation in refractive index as a function of humidity and temperature is illustrated in Figure 4.

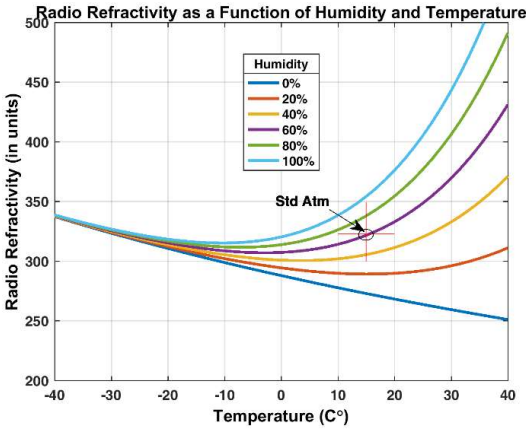

Figure 4. Variation in refractive index as a function of air temperature and relative humidity. The pressure is kept constant at 1013.25 mbar. The International Standard Atmosphere according to ISO 2314 is marked with a red cross-hair (The ISO 1314 Standard Atmosphere is defined as Temperature = 15°C, Humidity = 60% and Pressure = 1013.25 mbar at Sea Level).

For temperatures below −10 °C, the humidity contributes little to the changes in N. Above −10 °C, the changes in humidity has a significant influence on N. In our study, a temperature variation between −20 °C to +25 °C is to be expected.

The electromagnetic distance R is

$$\mathrm{R} = \frac{\mathrm{c}_0 T_0}{2 \cdot n\left(\vec{r}, t\right)}, \tag{2}$$

in which $\boldsymbol{T_o}$ is the travel time of the electromagnetic wave from the radar to the target and $\boldsymbol{n}\left(\vec{\boldsymbol{r}}, \boldsymbol{t}\right)$ is the spatial and temporal index of refraction. A small change in range $\boldsymbol{\Delta R}$ of a reflecting object will result in a proportional change in the phase $\boldsymbol{\Delta_\varphi}$ of the following reflected signal:

$$\Delta\varphi_{dis} = \frac{4\pi}{\lambda}\Delta\mathrm{R} = 2k\Delta\mathrm{R}, \tag{3}$$

in which $\boldsymbol{k} = \frac{2\pi}{\lambda}$ is the wavenumber. Equation (3) is the definition of interferometry. The phase is ambiguous with integer multiples of 2π. To track motions by interferometry, we must be able to unwrap the phase correctly. This turns out to be a major challenge for long distances due to atmospheric variations. Assuming a stationary reflector, the observed variation in distance is due to variations in the index of refraction. This phase-variation is

$$\Delta\varphi_{atm} = \frac{4\pi\mathrm{R}}{\lambda}\Delta\mathrm{n} = 2kR\Delta\mathrm{n}, \tag{4}$$

To partly overcome this problem, a reference reflector may be used, enabling us to do differential measurements. This will eliminate the effect of atmospheric variation on the path between the radar to the reflectors, leaving only the path between the two reflectors. If we have two reflections represented by the complex numbers $\boldsymbol{z_1}$ and $\boldsymbol{z_2}$, the differential interferogram is

$$z_1 z_2^* = a_1 a_2 \cdot e^{i(\varphi_1 - \varphi_2)}, \tag{5}$$

in which $\boldsymbol{z^*}$ denotes the complex conjugate of z. The angle is computed by taking the inverse tangent of the following argument:

$$\varphi_i = tan^{-1}\left\{\frac{imag(z_1 z_2^*)}{real(z_1 z_2^*)}\right\}, \tag{6}$$

The differential interferometric phase $\boldsymbol{\varphi_i}$, i.e., the difference between $\boldsymbol{z_1}$ and $\boldsymbol{z_2}$, is the sum of the following multiple effects:

$$\varphi_i = \varphi_{dis} + \varphi_{atm} + \varphi_{noise}, \tag{7}$$

in which $\boldsymbol{\varphi_{dis}}$ is the phase due to the displacement of the target, $\boldsymbol{\varphi_{atm}}$ is the phase due to atmospheric delays, and $\boldsymbol{\varphi_{noise}}$ is the phase noise due to the radar hardware.

When using interferometry the maximum unambiguous displacement is

$$\Delta r_{max} = \pm\frac{\lambda}{4}, \tag{8}$$

The relation between the wavelength and the pulse repetition frequency (PRF) gives the following maximum unambiguous velocity:

$$v_{max} = \pm\frac{\lambda}{4} \cdot PRF, \tag{9}$$

In our case, we measure once a minute, giving a PRF of 1/60 Hz. The wavelength of the signal is $\lambda_{9.65\,\mathrm{GHz}}$ = 31.1 mm, giving a maximum unambiguous velocity of v_{max} = 129.4 μm s^{-1} or ~4.2 mrad·s^{-1}. This gives a maximum unambiguous displacement per day of ~11.2 m.

Analytical expressions for the radar cross section (RCS) exist for some simple shapes including spheres, flat plates, and di- and trihedral. Apart from the sphere, the RCS of an object is heavily dependent on the frequency and the angle of the incident field. At Hegguraksla, we use triangular trihedrals reflectors. The analytical expression for the maximum RCS of a triangular trihedral is given as [4] (p. 25) as

$$\sigma_{trihedral} = \frac{4\pi a^4}{3\lambda^2}, \tag{10}$$

in which $\boldsymbol{a}$ is the short side of the triangle and λ is the wavelength of the radar.

4. Data Processing

In this chapter, we present some basic measurements of the mountain and the pre-processing of the data. We start by analyzing the amplitude of the reflections from the corner reflectors. We then analyze the statistical distribution of the backscatter from the reflectors and the clutter from the mountain. By clutter, we mean the unwanted backscatter from all surfaces other than the reflectors. We then look at how the variation in radio refractivity affects the path length between the radar and the reflectors, and how snow build-up affects the measurements and the phase tracking. All analysis is based on data from radar measurements in Tafjord between 2nd March 2010 and 23rd March 2018.

4.1. Data Preprocessing

To avoid including corrupted data in our analysis, basic data cleaning is necessary before interferometric processing. The most probable cause of corrupted data is heavy atmospheric attenuation resulting in low amplitude levels. An amplitude cut-off value was set, and all measurements with values below this cut-off were rejected. During periods with heavy atmospheric attenuation, we have experienced attenuation in the order of 40–50 dB. Our experience from data collected in Tafjord is that we can track and unwrap the phase correctly with a signal attenuation of more than 20 dB. Based on this observation, the initial cut-off value was put at 30 dB below the one-hour moving average of the amplitude. The variation in amplitude level for all six reflectors during the measurement period is presented in the time-amplitude plot in Figure 5.

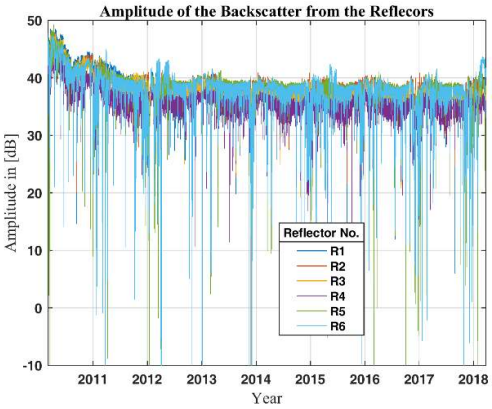

Figure 5. Time-Amplitude plot showing the amplitude of the reflected energy from the six reflectors as a function of time. Most of the attenuation is in the winter-months, which for this part of Norway and this elevation is from November to March.

An illustration of the signal and noise problem is shown in Figure 6. The noise, $\boldsymbol{N}$, is assumed to have a complex circular Gaussian distribution and is indicated by the red circle. $\boldsymbol{Y}$ is the actual backscatter, while $\boldsymbol{A}$ is the measured backscatter corrupted by the noise $\boldsymbol{N}$. The measured angle $\boldsymbol{\phi_A}$ differs from the actual angle by the noise angel. The noise is composed of variation in the clutter within the range-cell, variations in the refractivity, thermal noise, and instrument noise.

By using triangular corner reflectors, we increase the ratio between vector $\boldsymbol{Y}$ and $\boldsymbol{N}$, hence reducing the influence the noise has on the phase of the backscatter. If the ratio $\boldsymbol{Y{:}N}$ decreases to a level at which the noise is larger than the signal, i.e., the noise space covering the origin, we will have severe problems unwrapping the phase, since A will randomly move from quadrant to quadrant.

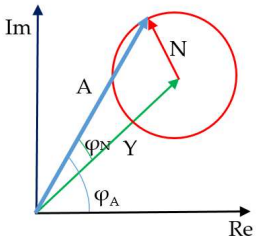

Figure 6. Phasor plot illustrating the amplitude and phase contribution. A is the amplitude of the measured backscatter from one range-cell. N is the sum of the noise and Y the actual backscatter from the reflector. $\boldsymbol{\phi_A}$ is the measured angle and $\boldsymbol{\phi_N}$ the angle of the noise contribution. The red circle illustrates the circular sample space of the noise.

After first eliminating measurements with values below the selected cut-off value, we use a statistical method to analyze the stability of the backscatter. Measurements with values below this statistical cut-off are rejected. We apply a method introduced by Ferratti et al. [9], originally intended as a way of identifying stable permanent scatterers in Synthetic Aperture Radar (SAR) data scenes. This is a measure for the phase stability called the dispersion index, defined as

$$D_A = \frac{\sigma_A}{m_A}, \tag{11}$$

in which $\boldsymbol{m_A}$ is the mean value of the backscatter and $\boldsymbol{\sigma_A}$ is the standard deviation of the backscatter. This method is reported to give reliable results for high signal-to-noise (SNR) ratios, but without specifying what a high SNR is. The method is reported in [9–11] to give stable results with a threshold value typically around 0.25. Some of the shortcomings of the method like its tendency to overestimate the stability of the phase are pointed out in Appendix B in [12]. After applying this data exclusion method, we calculate the differential interferogram according to Equation (5).

4.2. Amplitude Variations

The range–amplitude plot presented in Figure 7 shows the backscatter from the mountain and the six corner reflectors. The results presented in Figure 7 are range-compensated by a range factor of R^4 according to the radar equation [8].

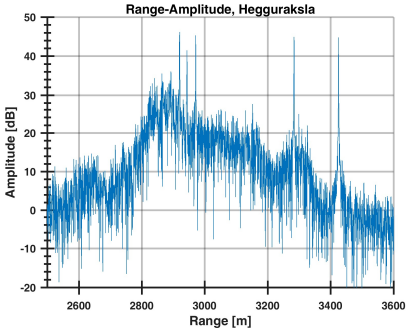

Figure 7. A section of the range–amplitude plot showing the distinct reflections from the six triangular corner reflectors. Note that the first peak contains both reflectors 1 and 3, as they are separated by just three range-cells. The range plot is range-compensated for by a range factor of R^4 according to the radar equation [8]. The corner reflectors are in a range from 2900 to 3400 m. The radar cross section of the reflectors is 36.2 dBsm at 9.65 GHz.

The range in the plot is from 2500 m to 3600 m. The steep increase in backscatter level from 2700 m to 2800 m corresponds to the incline of the mountain. Equally, the backscatter level decreases from 2900 m to 3400 m as the slope of the mountain falls off. From 3500 m onward, we have only clear sky; this means that the backscatter is mainly from the side-lobes of the antenna. The triangular corner-reflectors dominate the backscatter from their respective range-cells, which implies that they can be treated as stable point targets. Table 2 shows mean amplitude values and standard deviation of the amplitude for the measurement period.

Table 2. Mean amplitude value and standard deviation of the amplitude for the measurement period. The higher variation at Site 3 is believed to be caused by the longer distance, which gives a greater susceptibility to atmospheric attenuation.

Site	Reflector	Mean Amplitude [dB]	Standard Deviation [dB]
1	1	38.0	2.8
	2	38.8	2.2
2	3	37.6	2.5
	4	35.6	2.1
3	5	38.1	3.9
	6	38.0	4.0

The backscatter is stable, except during periods with high atmospheric attenuation or occasional blocking of the antennas. When this occurs, the data acquired is rejected. For the lower two sites, the standard deviation of the backscatter is between 2 and 3 dB; for Site 3 the standard deviation is approximately 4 dB. The higher variation in backscattered energy at Site 3 is probably due to the longer range between the radar and the reflectors, which gives greater susceptibility to atmospheric attenuation.

The majority of blocking due to attenuation occurs in the winter months and is believed to be caused by snow, especially wet snow or sleet (see Figure 8).

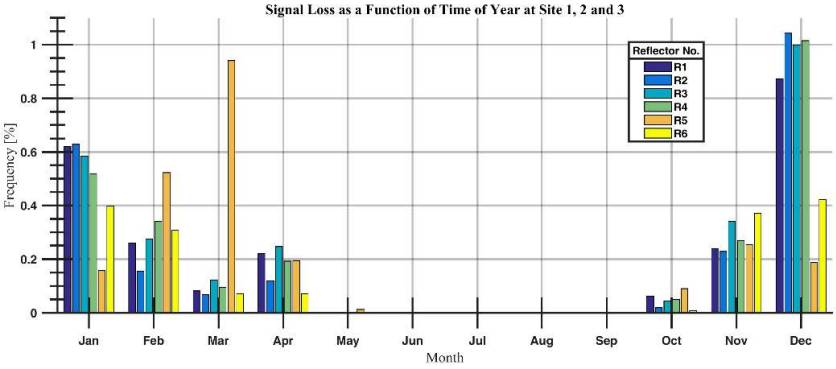

Figure 8. The percentage of time per month that the signal has fallen below the cut-off value for the measurement period. Most of the fall-outs occur in the winter.

As can be seen from Figure 8, most of the fall-outs occur in the winter-months. There is a significant difference between the frequency of fall-outs in January and December between the two lower sites and Site 3 at the top of the mountain. The reason for this might be the difference in height, which means Site 3 might experience snow while the two lower sites have rain or sleet as the attenuation of rain or sleet is higher than dry snow. Another reason is the signal-to-clutter level, which is higher at Site 3 than at the two lower sites, refer to Figure 7.

Comparison of the statistical distribution of the backscattered energy from the corner reflectors and the mountain gives further insight into the signal-to-clutter level to be expected. In Figure 9, histograms for the range-cell containing the reflector and nearby clutter from the 8 years of monitoring are shown.

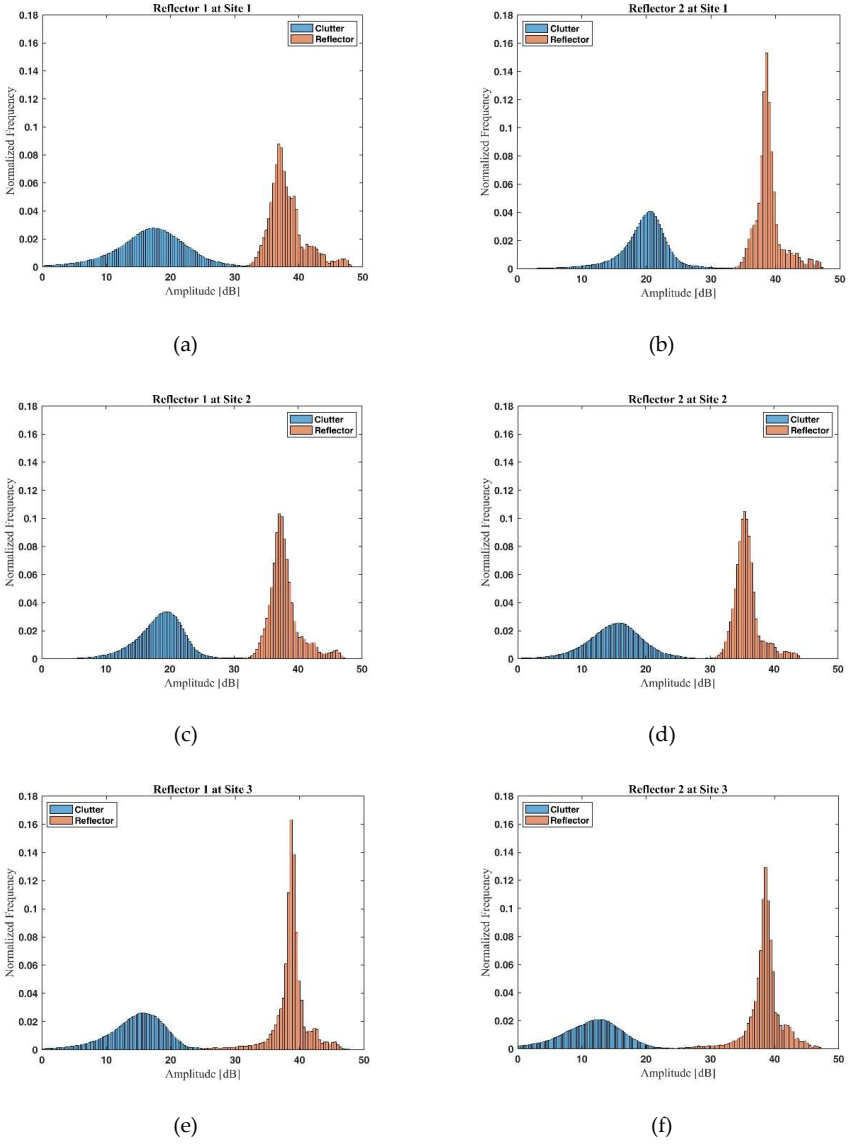

Figure 9. The variation of the amplitude reflects the signal-to-clutter level of each corner reflector. Panel (**a**) and (**b**) are from Site 1, panel (**c**) and (**d**) are from Site 2, and panel (**e**) and (**f**) are from Site 3. High signal-to-clutter level produces low variation. The amplitude of the backscattered energy from the reflectors shows a Rayleigh distribution as stated in [9], while the clutter from the mountain is normally distributed.

The histograms are based on all data from 2nd March 2010 to 23nd March 2018. The reflectors are grouped horizontally per site (panel (a) and (b) are from Site 1, panel (c) and (d) are from Site 2, and panel (e) and (f) are from Site 3). The results show that the amplitude of the backscattered energy from the triangular corner reflectors is about 20 dB above the clutter level, making them easily detectable point targets. The result corresponds to the range–amplitude plot presented in Figure 7. These results support the assumption that the natural clutter from the mountain has a normal distribution while the artificial reflectors, being point targets, have a Rayleigh distribution [9].

4.3. Relation between Meteorological Data and Radio Refractivity

As presented in Section 3, meteorological data can be used to calculate the radio refractivity, and the results can be used to compensate the measurements for variations in the refractivity. The meteorological data used in this chapter is from The Norwegian Meteorological Institute's measurement station in the village of Tafjord. The meteorological station is located at an altitude of 11 m AMSL and records meteorological data every sixth hour. This is not frequent enough to do post corrections of the measurements, but it can be used to show trends in the radio refractivity. Another weakness is the distance between the meteorological station and the radar, which is approximately 8.5 km. This adds uncertainty to the calculations. The measured pressure, humidity, and temperature is presented in Figure 10.

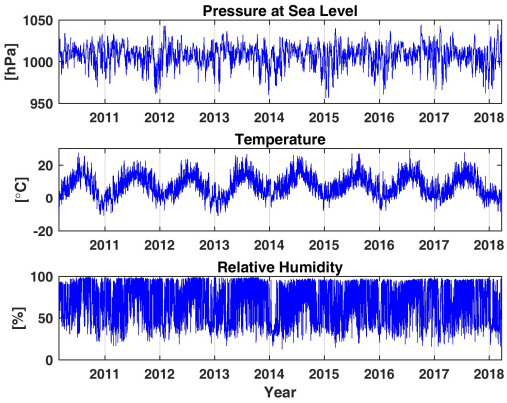

Figure 10. Meteorological data showing pressure, temperature, and relative humidity from March 2010 to March 2018. The meteorological data are from The Norwegian Meteorological Institute's measurement station in Tafjord, located approximately 8.5 km from the radar.

By estimating the variation in path length from the meteorological data presented in Figure 10, we can calculate the variation in path length for the path between the radar and the six reflectors. In Figure 11, we present the calculated variation in path length between the radar and reflector 1 at Site 1 and between the two reflectors at Site 1.

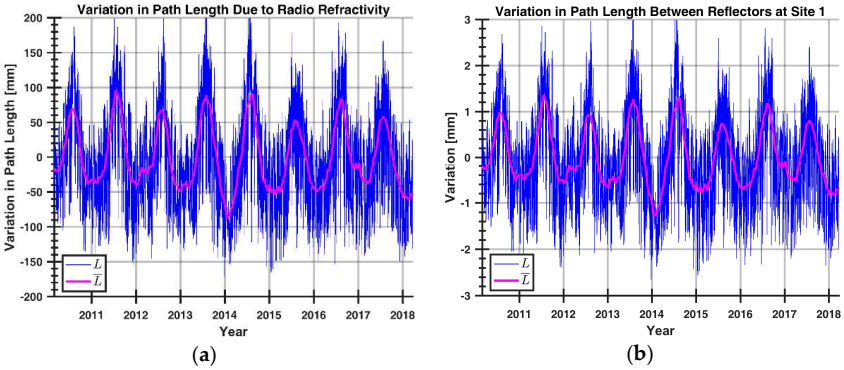

(**a**) (**b**)

Figure 11. Panel (**a**) shows the estimated variation in path length between the radar and reflector 1 at Site 1 due to variations in the radio refractivity. Panel (**b**) shows the path length variations between the two reflectors at Site 1. The blue line is the raw-data, while the magenta line is 3-month moving mean. The variation in path length due to radio refractivity is reduced by a factor of approximately 66 when using the differential technic.

From Figure 11a, the estimated variation in path length between the radar and reflector 1 at Site 1 is almost 400 mm. From Figure 11b, the variation in path length between the two reflectors at Site 1 shows a total variation of about 6 mm. This illustrates the reduction in path length variation between differential and non-differential measurements. Estimated variation due to radio refractivity in radar-to-reflector path length for reflector 3 at Site 2 is 390 mm, while the variation between reflector 3 and 4 at Site 2 is 2.6 mm. This is a reduction in variation due to radio refractivity by a factor 150. For Site 3, the radar-to-reflector path length variation due to radio refractivity is 438 mm, while the variation between reflector 5 and 6 at Site 3 is 16.1 mm. This is a reduction in variation due to radio refractivity by a factor 27.

This eliminates a lot of uncertainty in the phase tracking and the phase unwrapping processes. Referring to Figure 6, the noise vector, $\boldsymbol{N}$, is reduced accordingly. This clearly shows the benefit of the differential technique, which results in improved accuracy.

The distances between the reflectors and the estimated variation in path length due to refractivity both for differential and non-differential interferometry for the three sites are listed in Table 3.

Table 3. Key parameters for each site. The maximum variation in path length for both radar-to-site and reflector-to-reflector per site are listed.

Site	Reflector Number	Radar to Reflector Distance[m]	Height (AMSL) [m]	Inter Reflector Distance Per Site [m]	Difference in Reflector Elevation [m]	Maximum Variation in Path Length between Radar and Reflector [mm]	Maximum Variation in Path Length between Reflectors Per Site [mm]
1	1 2	2918.9 2970.9	734 754	52	20	395.2 401.3	6.0
2	3 4	2920.4 2942.9	837 853	22.5	16	389.4 391.8	2.6
3	5 6	3283.1 3424.7	957 995	141.6	38	430.1 446.3	16.1

Table 3 shows that by using differential interferometry, the variation due to radio refractivity can be significantly reduced. If we divide the variation in path length from radar-to-reflector by the radar-to-reflector distance, we get a factor of approximately 7.5:1. If we do the same with the reflector-to-reflector path length variation and reflector-to-reflector distance, we get a factor of approximately 9:1. The deviation in results might be explained by how the difference in height is

accounted for in the radio refractivity model. Another issue is that the local atmospheric conditions in the mountain might deviate from the radar-to-reflector atmospheric conditions.

4.4. Impact of Snow on the Reflectors

Over the years, we have experienced challenges when the reflectors are covered by snow. This will cause a phase tracking challenge, since we have no means of measuring the depth of the snow cover and compensating for the added path-delay. Figure 12a shows the effect of snow build-up inside the reference reflector at Site 1 during the winter of 2011. Figure 12b shows a picture taken of one of the reflectors during the winter of 2011.

The displacements presented in Figure 12a are believed to be caused by snow building up inside the reflector. This results in an increased distance due to the longer traveling path of the electromagnetic waves. By comparing the possible build-up of snow with the temperature profile, there is a good correlation between the calculated temperature and the snow build-up and the snow melting. Clearly identified in the end of February and beginning of March when the temperature rises, the snow inside the reflector melts, and the electromagnetic path length is once again reduced. The increase in distance at Site 1 during the winter of 2011 is tracked without loss of data, and the displacement before and after the snow build-up is within 1 mm. During the build-up and melting of snow in the winter of 2010, we lost the signal 5 times due to atmospheric attenuation, producing high uncertainty in phase unwrapping results.

The phase tracking in the winter of 2012 resulted in a displacement of more than 6 mm. This displacement is believed to be erroneous and a result of loss of signal due to heavy attenuation and snow build-up inside one or both reflectors at Site 1.

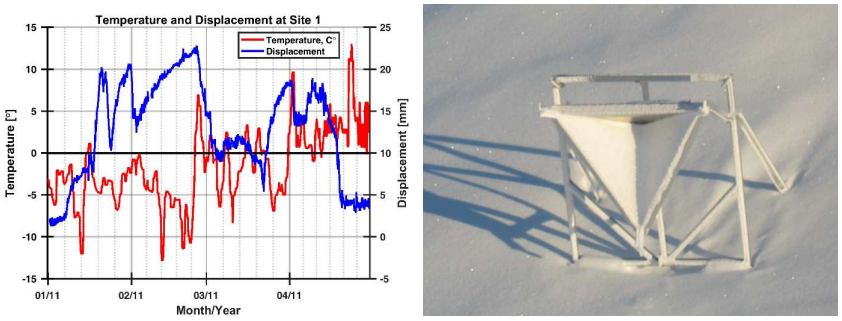

(**a**) (**b**)

Figure 12. (**a**) Variation in path length and estimated temperature profile as a function of time at Site 1 during the first four months of 2011. This variation is believed to be caused by build-up of snow inside the reflector. Please note that even though the variation at the end of January seems to be instantaneous, the maximum measured velocity is in the order of 2 mrad·s^{-1}, which is about half the maximum unambiguous velocity of the radar (vmax = 4.2mrad·s^{-1}). The temperature profile is based on the meteorological data presented in Figure 10. Even though the meteorological data is from a station 8.5 km away, it gives an indication of the temperature at Site 1. There is a good correlation between the temperature profile and the measured displacement of the reflector. (**b**) Picture of build-up of snow inside one of the reflectors during the winter of 2011. The photo is from Åknes-Tafjord IKS.

To check which of the reflectors at Site 1 were covered by snow, we compared the two reflectors at Site 1 with the reference reflector at Site 2. The comparison reveals that reflector 2 at Site 1 was covered by snow in the winters of 2011, 2012, and 2015. Reflector 1 at Site 1 showed no sign of being covered by snow. This result is supported by the placement of the reflectors at Site 1. The main reflector is right

at the edge of the mountain, making it less likely to be exposed to snow drift, whereas the reference reflector is located at a more shielded position that is more likely to be exposed to snow drift.

5. Long Term Monitoring Results

In this chapter, we present the results from the long-term monitoring of the mountain with the ground-based radar in the period 2nd March 2010 to 23rd March 2018. The radar has been operational 96.4% of the time, in which major stops are due to faults on the mains power.

5.1. Diurnal Variations

The data from the ground-based radar reveals diurnal variations in the measured path length using Equation (3). This variation is believed to be caused by diurnal variations in temperature and radio refractivity. An example from four days in June 2010 is presented in Figure 13.

The results presented in Figure 13 show a diurnal cyclic variation in path length between the two reflectors at Site 2. There is a good correlation between the measured path length variation and the calculated radio refractivity. However, the estimation of radio refractivity seems to underestimate the path length variation.

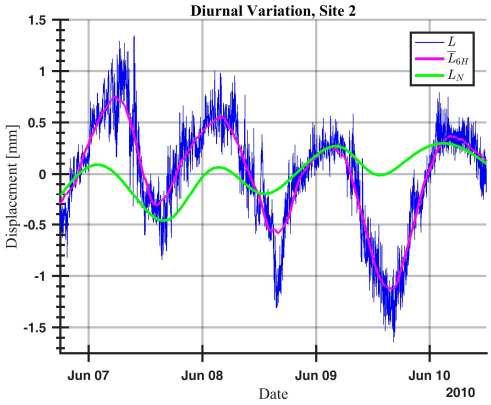

Figure 13. Diurnal variation in measured path length between the two reflectors at Site 2. The blue line is the raw data, the magenta line is the 6-h moving mean, and the green line is the calculated variation in the radio refractivity. As the plot shows, there is a good correlation between the measured path length variation and the calculated radio refractivity.

5.2. Annual Variations

The path length to the reflector pairs at each site is calculated by differential interferometry, Equation (3), and the resulting time-displacement diagram for all three sites are presented in Figure 14. Negative values indicate a shorter path length between the radar and the reflectors.

When analyzing the results, we see an annual cyclic variation in the path length, especially at Site 3. This variation is in good correlation with the annual temperature variations; see meteorological data in Figure 10. There is significant variation in phase stability from site to site. Sites 3 and 1 have a significantly higher variation than Site 2. This is as expected, since the distance between the two reflectors at these sites is longer. The cumulative displacement at Site 1 is 4.7 mm, at Site 2 the displacement is approximately 1 mm, while Site 3 shows, as expected, no displacement. The large displacement at Site 1 is believed to be a result of snow build-up, which we were unable to track correctly during both build-up and melting (see Section 4.4).

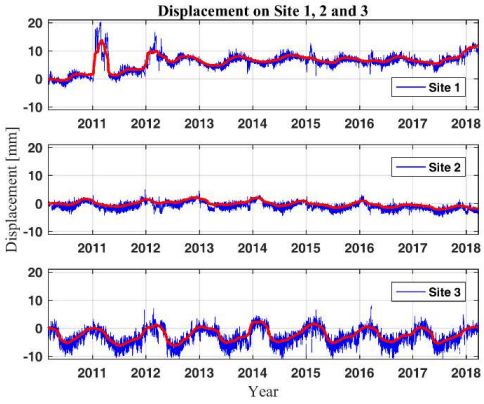

Figure 14. Time–Displacement diagram for the three sites during 8 years of monitoring. Note that negative values indicate shorter distance between the radar and the reflectors. The blue line is the raw-data, while the red line is the 3-months moving mean. The figure shows annual cyclic variations, which correlate with the annual temperature variations.

5.2.1. Estimated Motion at Site 1, Reflector 1

A detailed plot of the displacement of Site 1 as measured by the radar is presented in Figure 15a, both raw data and three-months moving mean. We also present the displacement of reflector 1 with respect to the four reference reflectors (reflectors 2, 4, 5, and 6, see Figure 2) in Figure 15b.

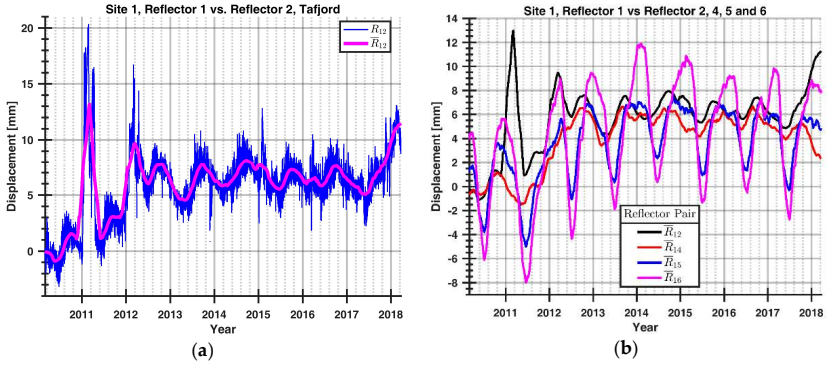

Figure 15. (**a**) The displacement as a function of time for Site 1, reflector 1 referenced to reflector 2. There are three large displacements visible in the plot during the winters of 2011, 2012, and 2018. All three displacements are believed to be caused by build-up of snow inside the reference reflector. The blue line is the raw-data, while the magenta line is the 3-month moving mean. (**b**) The displacement of reflector 1 at Site 1 referenced to all the reference reflectors. They all show similar motion, the major difference being the variation in the amplitude of the annual cyclic motions. The variation in amplitude increases with the distance between reflector 1 and the reference reflectors.

Figure 15a shows two interesting features: firstly, the three large displacements taking place during the first months of 2011, 2012, and 2018; and secondly, the displacement developing from the middle of 2011 to the middle of 2012 that is about 6 mm. According to geological analysis, the most probable reason is a rotation of the mountain block towards the fjord at the base and backwards at

the top [13]. Other possible reasons are snow build-up inside the reference reflector or snow build-up behind the reference reflector permanently bending the beams securing the reflector to the mountain.

The comparison between the four reference reflectors presented in Figure 15b shows the same trend but with some differences. The amplitude of the annual cyclic variations gets higher as the distance between the reflectors compared increases. This result is supported by the results presented in Section 4.3 and is due to the radio refractivity caused by variation in path length. Only the results from Site 1 show a pronounced displacement in the winter of 2011 and 2018, further supporting the belief that reflector 2 at Site 1 was covered by snow. The displacement occurring in the winter of 2011–2012 is present in all the data, indicating a backwards motion of the block. This assumption is supported by the geological analysis of the mountain block as it is moving outwards at the base, which implies an inward rotation of the top of the block [13]. An inwards rotation of the top would result in an increased radar-to-reflector path, which is what we observe in the winter of 2011–2012.

The measured displacement of reflector 1 at Site 1 compared to the four reference reflectors is given in Table 4.

The reason why the standard deviation of reflector 2 at Site 1 is higher than the standard deviation of reflector 4 at Site 2 is probably due to the partial loss of reflector 2 in the winters of 2011, 2012, and 2015.

Table 4. Measured displacement of Reflector 1 at Site 1, referenced to the four reference reflectors.

Site	Reference Reflector	Total Motion 2010–2018 [mm]	Standard Deviation [mm]	Motion 2013–2018 [mm]
1	2	4.7	3.1	1.7
2	4	5.3	2.9	−0.9
3	5	5.2	4.5	−0.2
	6	6.1	6.5	−0.5

5.2.2. Estimated Motion of Site 2, Reflector 3

A detailed plot of the measured displacement of Site 2 is presented in Figure 16a, both raw data and three-months moving mean. To verify the displacement at Site 2, reflector 3 is compared to all the four reference reflectors (reflectors 2, 4, 5, and 6, see Figure 2) in Figure 16b.

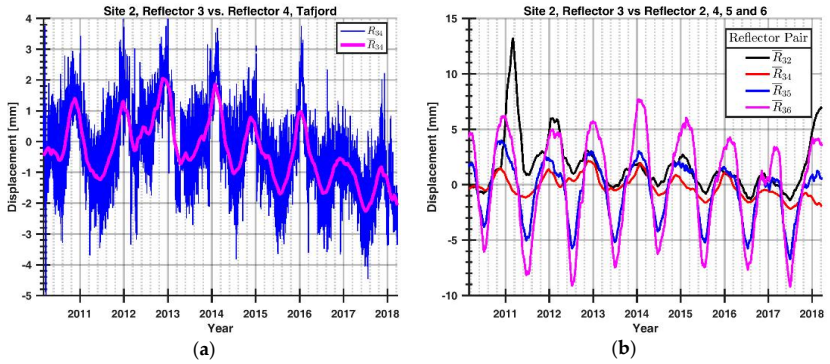

(**a**) (**b**)

Figure 16. (**a**) The displacement as a function of time for Site 2 from 2010 to 2018, reflector 3 referenced to reflector 4. The blue line is the raw-data, while the magenta line is the 3-months moving mean. The results show a displacement of −1.2 mm for the whole timespan. The displacement from 2013 to 2018 is in the order of −2.0 mm. (**b**) The displacement as a function of time for reflector 3 referenced to the four reference reflectors (reflectors 2, 4, 5, and 6). They all show similar motion, the major difference being the variation in the amplitude of the annual cyclic motion. The standard deviation increases with the distance between reflector 3 and the reference reflectors.

The total displacement from 2010 to 2018 is in the order of −1.2 mm. The annual cyclic variations are clearly visible in Figure 16. The measurements seem to be stable for the first two years and then show a motion away from the radar during the last 6 months of 2012. From 2013 onwards, there seems to be a steady motion towards the radar. The displacement from 2013 to 2018 is in the order of −2.0 mm.

Reflector 3 shows the same displacement pattern when compared to the four reference reflectors, with the major differences being the variation in the amplitude of the annual cyclic variations. The Site 2 comparison is summed up in Table 5.

Table 5. Measured displacement of reflector 3, referenced to the four reference reflectors.

Site	Reference Reflector	Standard Deviation [mm]	Total Motion [mm]	Motion 2013–2018 [mm]
1	2	3.2	−2.2	0.6
2	4	1.2	−1.6	−2.0
3	5	4.0	−1.6	−1.3
	6	6.3	−0.9	−1. 8

There is a significant motion of the mountain block of approximately 2 mm from 2013 to 2018. The major direction of motion of the block is believed to be vertical with an outwards motion at the base [13].

5.2.3. Estimated Motion at Site 3, Reflectors 5 and 6

We have not detected any motion between reflectors 5 and 6 at Site 3, except annual cyclic motions that are believed to be caused by temperature variations, see Figure 17.

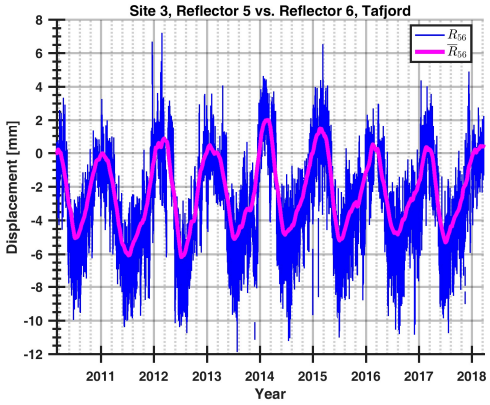

Figure 17. Displacement as a function of time for Site 3; reflector 5 referenced to reflector 6. The blue line is the raw-data while the red line is the three-months moving average. There is no displacement detected of Site 3 except for the annual cyclic motion.

For reference, a comparison of differential interferometric measurements with and without radio refractivity corrections applied to the path length between the reflectors is presented in Figure 18.

As shown by Figure 18, the result for Site 3 shows a good correlation between the estimated refractivity and the calculated differential interferometric displacement. The annual variation is reduced by nearly 35%.

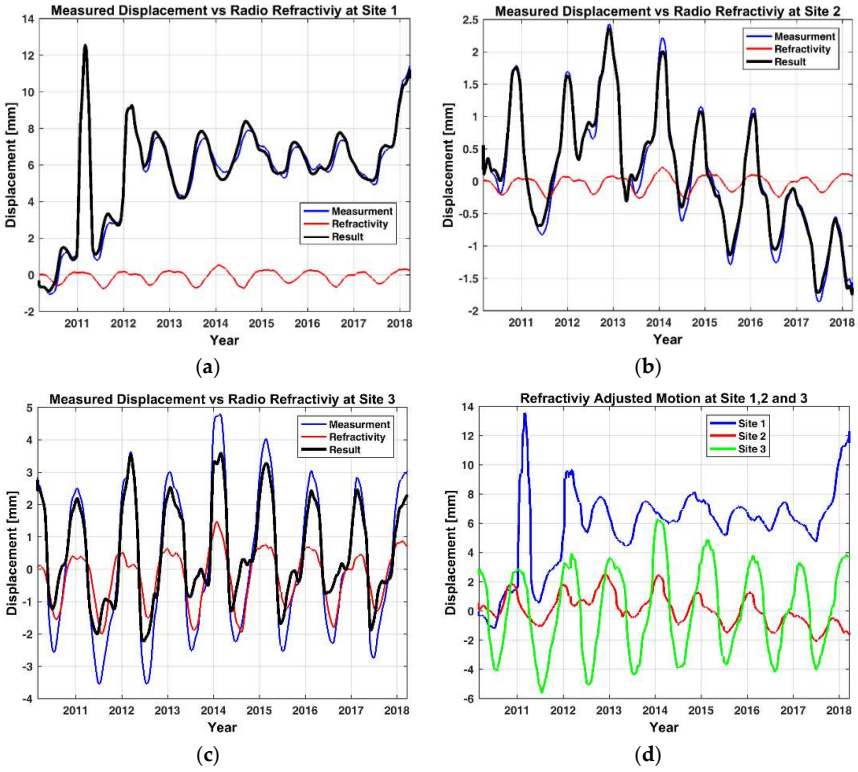

Figure 18. Three months moving average of the measured displacement adjusted with radio refractivity estimated from the meteorological data. (**a**) is Site 1, (**b**) is Site 2, (**c**) is Site 3, and (**d**) is all three sites combined. The blue line is the differential interferometric displacement. The red line is the variation in path length estimated from radio refractivity. The black line is the radio refractivity-corrected displacement. This shows that meteorological data can be used to reduce the path length variation due to variations in radio refractivity, in the case of Site 3 by approximately 35%. Note the different scaling of the y-axis on the four figures.

6. Comparison of Displacement with Other Measurement Methods

The two unstable blocks at Hegguraksla are in addition to the ground-based radar monitored by spaceborne radar and geotechnical instruments like extensometers and crackmeters. At Site 1, two extensometers have been operational since February 2012. The extensometer data is collected every 30 min; this data was kindly made available from the Åknes/Tafjord Beredskap IKS [13] (see Figure 19a). We also have data from the Earth Observation Satellite RADARSAT-2 owned by the Canadian Space Agency. This data was kindly made available for us from Norut [14] (see Figure 19b). This is a spaceborne radar, and all measurements are line-of-sight (LOS) and not converted to vertical displacemet. The two triangular corner reflectors used for the SAR measurements are located close to Site 1 and Site 3. At Site 1, we share foundation with the SAR-reflector.

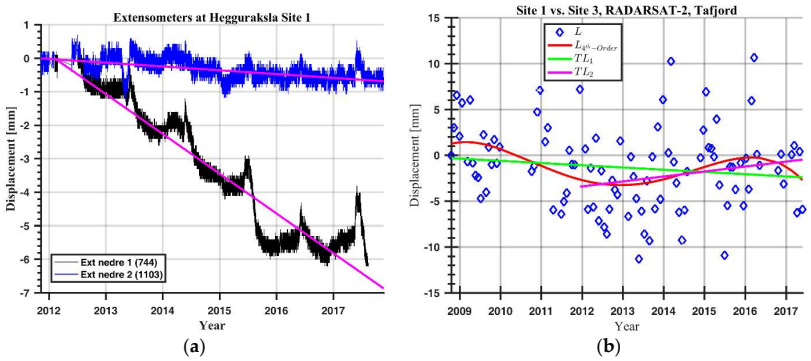

Figure 19. (**a**) Displacement as a function of time from the two extensometers mounted at Site 1. The trends show a displacement of −0.7 mm for extensometer 1 and of −6.0 mm for extensometer 2 from 6th February 2012 to 10th March 2017. The motion of extensometer 2 is believed to be partly due to failure of the mounting rods at one end. (**b**) Displacement as a function of time for the data from RADARSAT-2. The blue diamonds are the data samples, the red line is a 4th order polynomial fit, and the green line is a linear fit. The magenta line is a linear fit covering the same measurement period as the extensometers. Note that the satellite data are line-of-sight displacement and not vertical displacement.

From Figure 19, we see that the data from the two extensometers differ significantly; the one with reference number 744 has a recorded displacement of −0.7 mm, and the one with reference number 1103 has a recorded displacement of −6.0 mm. The motion of extensometer 2 is believed to be partly due to failure of the mounting rods at one end. Table 4 shows our measurements, which vary from 4.7 mm to 6.1 mm. The vertical displacement trend of the satellite reflector at Site 1 referenced to the satellite reflector at Site 3 from 2008 to 2017 is −2.1 mm, and from 2012 to 2017 is 2.1 mm. There are 98 samples available for this 8-years period.

At Site 2, there are three extensometers and three crack meters. These data were also made available for comparison with the radar data (see Figure 20).

All six instruments show different displacements due to the way they are mounted. It is interesting to note the distinct annual cyclic motion, which is in good correlation with the cyclic variation measured by the radar.

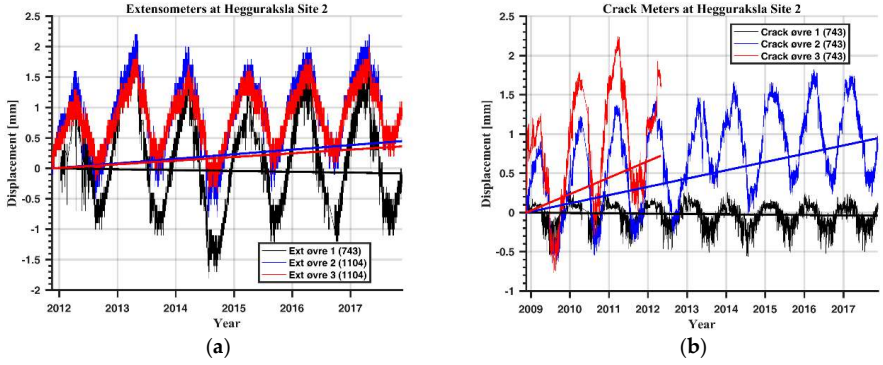

Figure 20. Displacement as a function of time from the extensometers and crack meters at Site 2. (**a**) The extensometers show a displacement varying from −0.08 mm to 0.45 mm. (**b**) The crack meters show a displacement varying from −0.04 mm to 0.95 mm.

7. Discussion

We have conducted eight years of continuous measurements with ground-based interferometric real-aperture radar of two unstable mountain blocks at Tafjord on the western coast of Norway. With this relatively long measurement period, we are able to assess and discuss several aspects of the project: the measurement uncertainties due to periodic changes on various timescales in atmospheric conditions typical for the local marine environment, applied measurement corrections, practical challenges of the established radar set-up shown in Figure 2, and measurement uncertainties relative to typical seasonal geological movement determined by other types of sensors. All sensors have their strengths and weaknesses, noise sources, and measurement errors, and measurement noise is displayed for extensometers in Figures 19 and 20a, crack meters Figure 20b, SAR Figure 19b, and ground-based radar Figure 13. It is beyond the scope of this article to discuss the error sources of geotechnical instruments, and in the following we will focus on error sources in interferometric ground-based radar. In general, the results presented show that a ground-based radar is a valuable supplement to, or substitute for, in situ geotechnical instruments.

The radar measurements show amplitude variation in backscatter from the reflectors due to variations in atmospheric attenuation and radio refractivity on various timescales. The fast variations between radar pulses are believed to be caused by rapid but small changes in the radio refractivity, see Figure 13. The diurnal and annual changes are believed to be mainly caused by temperature changes. The variations in atmospheric attenuation are mainly caused by the changing weather, which affects the accuracy of the measurements of the reflectors for three reasons. First, attenuation can lead to a total loss of signal resulting in missing data. Second, varying attenuation between the reflector-pairs compared differentially is a potential error source. An example is build-up of snow in one of the reflectors, see Figure 12. This will lead to drift in measured range, and unless it is possible to follow the build-up and the melting of the snow, we are unable to unwrap the phase correctly. Third, if the temporal variation in the atmosphere is faster than the measurement rate, it may introduce unwrapping ambiguities leading to uncertainties in the results (see Equation (7)). The variation in radio refractivity results in variation in the radar-to-reflector path length.

Based on the results from over eight years of monitoring of Hegguraksla Mountain, we have observed that the amplitude of the annual cyclic motion exceeds the displacement of the mountain blocks (see Figures 15–17). This is also shown in the results from the extensometers and crackmeters (see Figure 20). Thus, the measurement period must extend annual cyclic geologic movements believed to be caused by annual changes in temperature. This implies that the measurement period must exceed multiple annual cycles before any conclusions can be made with respect to actual mountain block displacements.

Statistical analysis of the radar backscattered energy shows that the triangular corner reflectors with a signal-to-clutter level of approximately 20 dB provide stable point targets for real-time monitoring (see Figure 9). The reflectors ensure that we monitor the unstable mountain blocks on which they are mounted and not the surrounding mountain area. The use of mounted corner reflectors are in our opinion the best way to ensure monitoring of specific points of interest with a minimum of noise.

Corrections for the variation in radio refractivity between the reflectors have been applied on the measured relative path length of the reflectors, and this has been successful to some extent. For Site 1 and Site 2, the correlation between the calculated path length due to radio refractivity and the measured path length is weak, and the effect of applying the refractive correction is low. Local variation in the boundary layer conditions with height is not registered with the single meteorological station at sea level. Another weakness of the meteorological data used for the applied radio refractive correction is the horizontal distance of 8.5 km between the meteorological station and the radar site, which opens for variations in the atmosphere across the fjord. The lack of correlation between the calculated radio refractivity and the measured motion at Sites 1 and 2 is believed to be due to a more complex atmospheric environment than at Site 3. Site 3 is located at the top of the mountain, and there are

no obstructions around the two reflectors, which probably gives a more homogeneous atmosphere. Both Sites 1 and 2 are located at the edge of the mountain and may be influenced by rising or falling air. The rapidly rising or falling air may be very turbulent, which is not taken into account by the radio refractive model. The model assumes linear changes in temperature, pressure, and humidity as a function of height. One possible way to improve the corrections is to have a weather station at each site and one at the radar, reducing the uncertainty in the refractive estimates.

A practical implication of the established radar set-up is the seasonal variations in snow cover during winter, shown in Figure 2. As shown in the measurement results (see Figures 12 and 15), the reference reflector at Site 1 has suffered from snow cover on three occasions during the eight years of monitoring. As we have four reference reflectors in our set-up, we compared the main reflector at Site 1 to the other three reference reflectors. The result indicates that the reference reflector was covered by snow, but by using the other reference reflectors the motion of the main reflector could be followed. This solves the problem, but increases the uncertainty in the results, as the distance to the other reference reflectors is longer. This problem can be solved by protecting the reflectors with snow protection-covers. Snow on the ground is a general problem in real-time monitoring, as the snow will affect the backscatter from the ground. It will result in both attenuation and a variation in path length due to the higher dielectric constant in the snow. Therefore, an uneven snowfall or thaw will appear as measured divergent motion. The use of radar reflectors will improve the measurement results, particularly under these types of measurement conditions.

The measurement uncertainties are assessed relative to typical seasonal geological movement measured by other sensors (see Figures 19 and 20). At Site 2, the results from the seven sensors (three extensometers, three crack meters, and the radar) all show the same seasonal cyclic motion. There is a spread in the results from these sensors, which is mainly believed to be determined by which part of the motion they measure, i.e., how they are mounted with regard to the motion of the mountain block. The annual variation in motion measured by the radar is ± 1 mm. This agrees with the annual variations measured by the extensometers and crack meters, which are between ± 0.3 mm and ± 1.5 mm. The annual cyclic motion measured by the radar and the geotechnical instruments is coherent with the cyclic pattern of meteorological data, which indicates that the observed cyclic motion is due to temperature variations. Disagreement between radar results and the results from the geotechnical instruments is probably a result of the relative motion measured by the geotechnical instrument. At Site 1, the data from the extensometers show no correlation with the seasonal cyclic motion measured by the radar. It is not clear why the extensometers at Site 1 do not show the cyclic motions while both the extensometers at Site 2 and the radar measurements from Site 1 do, as this should be independent from the mounting direction of the extensometers. The spread in the results from the two extensometers at Site 1 makes it hard to compare it directly with the radar measurements. We have compared the results from the main reflectors at Site 1 and Site 2 with all the reference reflectors, and the results show good correlation, supporting the accuracy of the radar results.

The results show that real-time monitoring is challenging in areas occasionally exposed to snow, as the majority of the radar signal fallouts occur is in the winter season (see Figure 8). During periods with heavy snow or sleet, the atmospheric attenuation can interrupt the monitoring. Whenever this happens, we get discontinuities in the data set, which last until an adequate signal level is restored. This is, in our opinion, the largest weakness of the current measurement set-up and the presented results. Based on the Hegguraksla monitoring results, it would be beneficial to apply a snow protection-cover or relocate the reference reflector at Site 1 to a location less exposed to snowdrift.

8. Conclusions

In this paper, we have presented eight years of mountain monitoring with a real-time differential interferometric ground-based radar. We have shown that the radar can produce reliable, long-time, weather-independent output and that results from the radar measurements are as accurate as in situ measurements with geotechnical instruments, making it possible to remotely monitor inaccessible

areas with high accuracy. The eight years of monitoring Site 1 shows a backwards motion between 4.7 mm and 6.1 mm. Based on the geological analysis of the mountain block, this motion is believed to be a geologic motion in which the block moves away from the mountain at the base and against the mountain at the top. Results for Site 2 reveal a sliding motion away from the mountain between 1.2 mm and 6.3 mm. This is also consistent with the geological analysis of the block at Site 2. The data collected show diurnal and annual variation mainly caused by variations in temperature and radio refractivity. The results show that for high accuracy monitoring, differential interferometry is preferable to non-differential interferometry, as it is less susceptible to variations in radio refractivity. We have also shown that variation due to radio refractivity can be reduced by using meteorological data to predict variations in radio refractivity and apply it to the measurements. For stable and predictable long-term surveillance, we recommend using reflectors mounted in the mountain that give a stable point-reflection. For real-time monitoring in changing atmospheric conditions, a high temporal sampling-rate is a prerequisite for interferometric measurements to avoid unambiguity in the unwrapping of the phase.

The results show both diurnal and annual cyclic variations, which means that we need a monitoring period of at least one year before making any conclusions about displacements, unless the displacement is larger than the diurnal and annual variations.

Snow cover of the reflectors causes a phase-tracking challenge if combined with heavy attenuation or loss of the radar signal. Based on the monitoring results, it would be beneficial to relocate the reference reflector at Site 1 to a location less exposed to snowdrift.

Future enhancements to the system should include a higher rate of measurement in order to avoid phase unwrapping ambiguities. There should be at least one local meteorological station close to the radar, preferably two stations, with the second at the base of the mountain. Additionally, there should be meteorological stations at each site due to the difference in height between the three sites, and the meteorological station should have a sampling rate high enough to compensate for rapid weather changes.

Author Contributions: Conceptualization: R.G. and R.N.; data curation: R.G.; formal analysis: R.G.; investigation: R.G.; methodology: R.G., R.N., and C.R.D.; software: R.G.; supervision: R.N. and C.R.D.; visualization: R.G.; writing—original draft: R.G.; writing—review & editing: R.G., R.N., and C.R.D.

Acknowledgments: The work was supported by the Research Council of Norway.

Conflicts of Interest: The authors declare no conflict of interest.

References

1. Banholzer, S.; Kossin, J.; Donner, S. *The Impact of Climate Change on Natural Disasters, Reducing Disaster: Early Warning Systems for Climate Change*; Singh, A., Zommers, Z., Eds.; Springer: Dordrecht, The Netherlands, 2014; pp. 21–49. [CrossRef]
2. Hole, J.; Blikra, L.H.; Anda, E. Scenario and prognoses for mountain avalanches and flodwaves from Åknes and Hegguraksla, Åknes/Tafjord Beredskap. *Stranda*, 2010. (in Norwegian)
3. Oppikofer, T. Detection, Analysis and Monitoring of Slope Movements by High-Resolution Digital Elevation Models. Ph.D. Thesis, Institute of Geomatics and Analysis of Risk, University of Lausanne, Lausanne, Switzerland, 2009.
4. Norland, R.; Gundersen, R. Use of radar for landslide hazard monitoring, Landslides and Avalanches, ICFL 2005 Norway. In Proceedings of the 11th International Conference and Field Trip on Landslides, Norway, 1–10 September 2005.
5. Norland, R. Differential interferometric radar for mountain rock slide hazard monitoring. In Proceedings of the 2006 IEEE International Symposium on Geoscience and Remote Sensing, Denver, CO, USA, 31 July–4 August 2006; pp. 3293–3296. [CrossRef]
6. Rolstad, C.; Norland, R. Ground-based interferometric radar for velocity and calving-rate measurements of the tidewater glacier at Kronebreen, Svalbard. *Ann. Glaciol.* **2009**, *50*, 47–54. [CrossRef]

7. Norland, R. Improving interferometric radar measurement accuracy using local meteorological data. In Proceedings of the Geoscience and Remote Sensing Symposium (IGARSS), Barcelona, Spain, 23–28 July 2007; pp. 3293–3296. [CrossRef]
8. Levanon, N. *Radar Principles*; John Wiley & Sons: Tel-Aviv, Isreal, 1988; ISBN 0471858811.
9. Ferretti, A.; Prati, C.; Rocca, F. Permanent scatterers in SAR interferometry. *IEEE Trans. Geosci. Remote Sens.* **2001**, *39*, 8–20. [CrossRef]
10. Kampes, B.M. *Radar Interferometry, Persistent Scatterer Technique*; Springer: Dordrecht, The Netherlands, 2006; ISBN 140204576-X.
11. Noferini, L.; Pieraccinin, P.; Mecatti, D.; Luzi, C.; Atzeni, C.; Tamburini, A.; Broccolato, M. Permanent scatterers analysis for atmospheric correction in ground-based SAR interferometry. *IEEE Trans. Geosci. Remote Sens.* **2005**, *43*, 1459–1470. [CrossRef]
12. Hooper, A.; Segall, P.; Zebker, H. Persistent scatterer interferometric synthetic aperture radar for crustal deformation analysis, with application to Volcán Alcedo, Galpágos. *J. Geophys. Res.* **2007**, *112*, B07407. [CrossRef]
13. Anda, E.; The Norwegian Water Resources and Energy Directorate, Oslo, Norway. Personal communication, 2018.
14. Lauknes, T.R. (Northern Research Institute, Tromsø, Norway). Personal communication, 2017.

Paper Ⅲ

Monitoring glacier flow and calving events with terrestrial interferometric radar in Ny-Ålesund, Svalbard.

Gundersen R, Norland R, Denby Rolstad C, Polar Research, in review, **2019.**

Monitoring glacier flow in Ny-Ålesund with a high temporal resolution ground-based interferometric phased array radar

Rune Gundersen[1,2], Richard Norland[2], Cecilie Rolstad Denby[1]

[1] Faculty of Science and Technology, Norwegian University of Life Sciences, Ås, Norway
[2] ISPAS AS, Moss, Norway

Correspondence to: Rune Gundersen (rune.gundersen@nmbu.no)

Abstract

Monitoring of glacier flow speed and calving rates are of interest for climate research, global sea-level studies, and for increased Arctic ship traffic. The research station in Ny-Ålesund, Svalbard offers a unique location close to multiple glacier fronts. In this study, we have explored the possibilities of permanent monitoring of glaciers in the Ny-Ålesund area using a ground-based interferometric radar with a significantly higher temporal resolution than what achievable from both satellites and mechanical scanning ground-based radars. Measurements were made from two different locations; Pynten and the Ny-Ålesund research station located 5 km and 15 km from Kronebreen glacier respectively. The temporal resolution of the radar is flexible and in this experiment is limited to five images per minute, providing near real-time data of glacier flow. We calculate a geolocated 2D flow map of the glacier from the radar data, extract glacier speed profiles and identify major calving onsets. This type of near real-time data may well be used with machine learning techniques for more advanced monitoring systems. We also confirm that the radar measurements agree well with previous satellite measurements at lower temporal resolution, the observed mean flow of the Kronebreen glacier front varies across the glacier from around 0.4 m/day at the edges to 3 m/day in the central part. In this paper, we identify and discuss possible improvements to the radar system, and conclude that Ny-Ålesund is a well-suited location for radar monitoring of glacier flow velocities.

Keywords: glacier flow; radar; terrestrial radar interferometry; phased array

1. Introduction

Increased calving is observed in Greenland and Antarctica and is probably due to global warming [1]. The increased calving can reduce the volume of land-based ice, which again leads to a global sea-level rise and increased fresh water input to the ocean [2] [3] [4]. The calving rate of tidewater glaciers increase with ocean temperature [5]. Measurements of the temporal variation in glacier-flow and the variation in calving rates can be a valuable input for studies of glacier dynamics. Direct measurements of the glacier-flow are often associated with high risk due to motion, crevasses, and calving activity especially for ocean terminating glaciers, while remote sensing is a safe solution.

Interferometric radar measurements are an established remote sensing technique in geosciences for measuring surface deformations that utilise the phase of the received radar signal to detect and track displacements. Satellites carrying synthetic aperture radar (SAR) can cover large areas with a relatively high spatial resolution. They have a surface displacement sensitivity in the order of millimetres when compensated for variations in the radio refractivity [6]. Due to the revisiting time (temporal resolution) of the satellite, geometric displacements between measurements can limit the accuracy of the measurements.

For detailed glacier flow studies, high spatial and temporal resolution is beneficial to avoid geometric decorrelation between consecutive measurements. A ground-based radar can achieve this, as a ground-based sensor is flexible when it comes to temporal resolution and instrument location, which in-turn controls the spatial resolution. Studies published on the subject of ground-based radar monitoring of glaciers use either interferometric real-aperture radar (GB-InRAR) [7], ground-based interferometric SAR (GB-InSAR) [8] [9] [10], or ground-based radar interferometer (GB-RI) [11] [12] [13] [14] [15] [16]. The mechanical scanning GB-RI antenna consists of one transmitting antenna and two or more receiving antennas giving elevation as well as azimuth information. Both GB-InSAR and GB-RI systems may provide better temporal and spatial resolutions than satellite borne systems.

A potential disadvantage of GB-SAR and GB-RI systems in monitoring of geologic rapid-moving objects is the mechanical motion of the antennas limiting the temporal resolution, however a way to combine spatial and high temporal resolution is to use an electronic scanning antenna, i.e. a phased array antenna [17]. A typical phased array antenna has the ability to change the angle of the antenna beam a few thousand times per second and achieve a higher effective temporal resolution due to the lower revisit time than a mechanically scanning antenna. Active phased-array antennas have been used in high-performance military and space systems for decades, but civilian use has been limited due to the high cost of development and manufacturing. In recent years, a number of integrated microwave circuits have been introduced simplifying the design and cutting the manufacturing costs making phased arrays radar systems a real alternative to GB-InSAR and GB-RI. A phased array is composed of a number of radiating elements whose phase and amplitude are individually controlled. The antenna beam is formed by shifting the phase of each element, altering the phase-front of the antenna and steering the antenna beam in the desired direction. The high temporal sampling of the radar makes it possible to extract detailed information of an area, which may be of value in the study of glacier dynamics such as instantaneous flow speed and detection of calving activity.

In this paper, we assess Ny-Ålesund as a potential location for permanent monitoring of glacier calving fronts using a ground-based high temporal resolution interferometric phased array radar. Near real-time data from calving fronts may be used for developing more advanced monitoring systems for ship traffic in the Arctic [18]. The main objectives are; to compensate for the variations in radio refractivity and attenuation due to atmospheric variations, finding the spatial resolution achievable with the prototype radar antenna, and to what accuracy can we track the glacier flow? The potential for further optimisation and development of the system is also discussed.

The Ny-Ålesund research facilities are located at Kongsfjorden in the northwest of the Svalbard archipelago, within a short distance of several glacier calving fronts. This research facility may be suited for long-term continuous calving observations by ground-based radar since it is manned all-year-round. To evaluate the pros and cons of Ny-Ålesund as a measurement site we used Pynten as a reference site, which at the time of measurement was the closest safe position to use for measuring Kronebreen. The installation and operation of a permanent ground-based radar in the Arctic region involves costly infrastructure and maintenance. If it is possible to achieve results of the same quality from Ny-Ålesund it will significantly simplify the installation and lower the overall cost of operation and maintenance of the radar system, as it will not require an autonomous radar station. In this paper we present the first results from monitoring the Kronebreen glacier with a high temporal and spatial resolution ground-based radar with a phased-array antenna.

The measurements are of the tidewater glacier Kronebreen that is terminating in Kongsfjorden, Svalbard, Figure 1b. The glacier is about 8 km long and it is fed by the Infantfonna glaciers and Holtedalsfonna, which is the second largest ice cap on Svalbard. Colletthøgda limits the extent of Kronebreen to the North, and Kongsvegen glacier is the limit in the South. Kronebreen is one of the fastest-flowing glaciers in Svalbard [19]. The results from January 2013 reported by [5] show a high flow of approximately 3 m/day in the central part of Kronebreen slowing towards the edges and up-glacier, reaching a flow just below one meter per day. The flow speed of Kronebreen also varies inter-annually and with the seasons of the year [20]. From 1999-2002 [20] reported a mean speed of 1.6 m/day in the centre of the glacier with an inter-annual variability of 16%. Reference [21] reports a summer maximum of 2.1 m/day in June and July 2011, and 3.2 m/day in July and August 2013, both in the central part of the glacier.

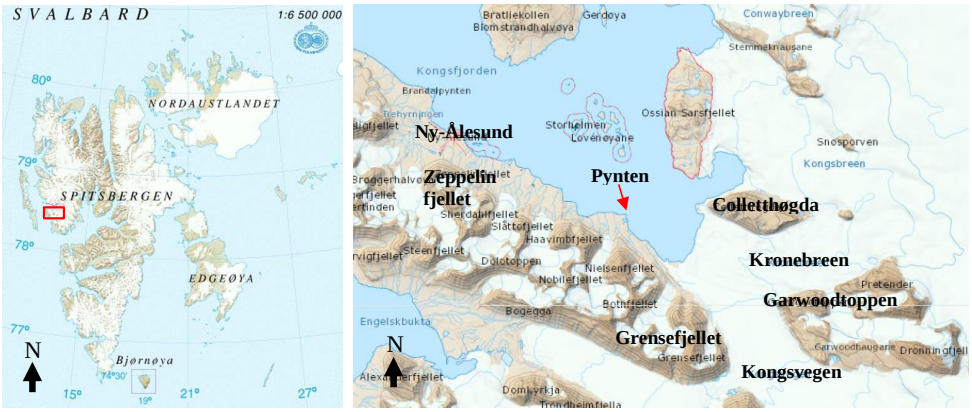

Figure 1 Location of the studied area. The maps are from the Norwegian Polar Institute.

The Norwegian University of Life Sciences (NMBU) and the company ISPAS AS have measured the flow of the Kronebreen glacier with a GB-InRAR yearly between 2007 and 2010 [22]. The measurements in 2007, 2008, and 2010 were conducted from Pynten (78°89'N, 12°34'E) approximately 4 km from the front of Kronebreen and in 2009 from Ny-Ålesund, 13 km from the front of Kronebreen, Figure 1b. The sampling rate of the radar was approximately one measurement per second, giving a high temporal resolution. However, this system does not give spatial data since it provides no cross-range information. During these campaigns, data was only acquired from the central part of the glacier, from the front of the glacier and a few hundred meters up-glacier. The speed of the glacier front was measured to be about 4 m/day slowing to about 1 m/day 400 meters up-glacier.

2. Radar theory and system description

In this section, we introduce some of the properties of the radar system and how the data can be used to extract information of the glacier flow.

2.1. Spatial resolution in range and cross-range

The radar's ability to distinguish two targets in distance depends on the radars range resolution, which is governed by the bandwidth $\boldsymbol{BW}$ of the transmitted radar signal [23]

$$\Delta \boldsymbol{R} = \frac{\boldsymbol{c_0}}{\boldsymbol{2BW}}, \tag{1}$$

where c_0 is the speed of light. The range resolution of the radar ΔR remains constant regardless of the distance from the radar. However, the area of the range-cells increases with distance (see Figure 2).

The cross-range or azimuth resolution of the radar is determined by the physical dimension of the antenna L and the distance R between the radar and the target [23]

$$\Delta R_{cr} = \frac{\lambda}{L} R, \tag{2}$$

where λ is the wavelength of the transmitted radar signal. From eq.2, we note that for a real aperture antenna the cross-range resolution declines linearly with the distance from the radar (see Figure 2).

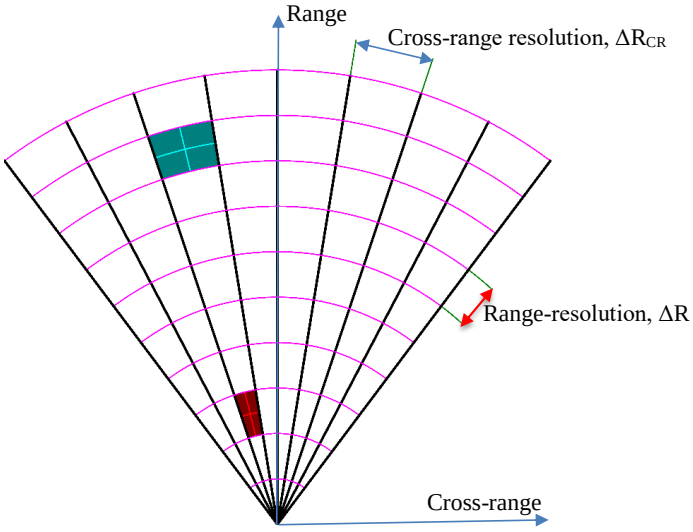

Figure 2 An illustration of the range and cross-range resolution of the radar system used. The range-resolution indicated by the magenta coloured concentric circles, note that the range resolution does not change with distance from the radar. The black lines indicate the cross-range resolution, which decrease linearly with distance from the radar indicated by the red and the cyan coloured squares.

The areas bound by the black and magenta lines in Figure 2 is the smallest area uniquely resolvable by the radar, in the following referenced to as a pixel.

2.2.Interferometric radar measurements

Interferometric radar measurements use the phase φ of the reflected electromagnetic wave to derive information from the reflecting object. The phase is a function of the distance from the radar to the target [24]

$$\varphi = \frac{4\pi}{\lambda} R, \tag{3}$$

φ is the observed relative phase which is ambiguous in the interval [$-\pi$, π] due to this ambiguity, the absolute distance R cannot be determined from φ. Hence, the maximum unambiguous range depends on the wavelength of the radar signal and is

$$|\Delta r_{max}| = \frac{\lambda}{4}, \tag{4}$$

Let the complex representation of the received radar signal be $z = Ae^{i\varphi}$. If we have two reflections represented by the complex numbers $\boldsymbol{z_1}$ and $\boldsymbol{z_2}$, the interferogram is

$$\boldsymbol{z_1 z_2^* = A_1 A_2 e^{i(\varphi_1 - \varphi_2)}} \quad (5)$$

where $\boldsymbol{z_2^*}$ is the complex conjugate of $\boldsymbol{z_2}$. If the two measurements $\boldsymbol{z_1}$ and $\boldsymbol{z_2}$ are of the same target obtained at different times, any change in phase of the target reveals any temporal changes in distance between the radar and the target.

The interferometric phase $\boldsymbol{\varphi}$ is the sum of multiple effects

$$\boldsymbol{\varphi = \varphi_d + \varphi_a + \varphi_n + 2\pi n}, \quad (6)$$

where $\boldsymbol{\varphi_d}$ is the phase due to the displacement of the target, $\boldsymbol{\varphi_a}$ is the phase due to atmospheric delays, $\boldsymbol{\varphi_n}$ is the phase noise due to the radar hardware, and $\boldsymbol{2\pi n}$ is the integer phase ambiguity. To unambiguously unwrap the phase of the interferogram, the right-hand sum in equation 6 must be less than λ/4 (eq. 4). Apart from using a radar with a low internal noise factor, the only parameter we can control to keep the phase shift $\boldsymbol{\varphi}$ below λ/4 is the time between measurements or the pulse repetition interval (PRI) of the radar. As $\boldsymbol{\varphi_d}$ depends on the targets displacement between measurements, reducing the time between measurements linearly reduces the phase shift. Hence, a high PRI is desirable to avoid phase unwrapping ambiguities and make the radar system more noise tolerant.

The maximum unambiguous velocity of a target is

$$|\boldsymbol{v_{max}}| = \frac{\boldsymbol{\lambda}}{\boldsymbol{4 \cdot PRI}}, \quad (7)$$

The propagation speed of electromagnetic waves through the atmosphere varies with humidity, temperature, and pressure. This is a time and spatial variation referred to as the index of refraction $\boldsymbol{\Delta n}$, which affects the interferometric phase [6]

$$\boldsymbol{\varphi_a = \frac{4\pi}{\lambda} \Delta n R}, \quad (8)$$

The variation in the radio refractivity can be estimated from meteorological data or measured by monitoring the temporal variation in distance between the radar and a stationary target in the measurement scene [7]. This can partly eliminate the variation in $\boldsymbol{\varphi_a}$.

2.3.Motion tracking

Interferograms are calculated per pixel for all data images pairs (eq.5). The temporal stability or coherence of the amplitude is used as the selection criterion. The coherency is estimated as a moving average of $\boldsymbol{n}$ observations per pixel as [25]

$$|\boldsymbol{\gamma}| = \left| \frac{\sum_{i=1}^{n} (\boldsymbol{z_1 z_2^*})}{\sqrt{\sum_{i=1}^{n} |\boldsymbol{z_1}|^2 \sum_{i=1}^{n} |\boldsymbol{z_2}|^2}} \right|, \quad (9)$$

Only the pixels with a coherence above a cut-off value are used and their phase is tracked and the displacement is cumulatively added image-by-image. A cut-off value of $\bar{\gamma} > 0.55$ is used as reported by [26] to assure statistical significance of the measured phase. The coherence is calculated using a moving average and depending on the coherence of the pixel, it will be dynamically added or removed from the result. The corrections for variations in the radio refractivity are applied based on the measured temporal phase of a selected fixed point. To track the motion of the glacier the phase from the selected points is unwrapped. If there are any unwrapping errors, i.e. jumps in phase above ±λ/4, the pixel is excluded from the result.

2.4.Organizing of data

The radar data collected is organized in three dimensions. The first dimension is the down-range where data is collected from a minimum to maximum radar-range with a resolution equal to the radar range-resolution (eq.1). The second dimension is the cross-range where data is collected per angle with an angular step resolution set by the radar. The effective cross-range resolution is limited by the 3-dB antenna beamwidth i.e. the physical dimension of the antenna (eq.2). The two dimensions gives us a 2D-array of data in down-range and cross-range, referred to as a data image. The third dimension is the temporal collection of data images. Figure 3 is an illustration of the organization of the collected radar data.

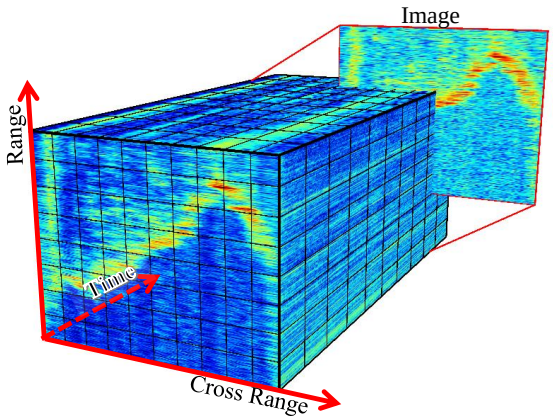

Figure 3 Illustration of how the data collected by the radar is organized. The 2D-array of range and cross-range data makes an image. The time between two images is the revisit time of the radar i.e. the temporal resolution.

2.5.Geometry of the measurements

A reflecting point on the glacier will be visible over an angle at least equal to the beamwidth of the antenna as illustrated in Figure 4. This means that a reflection point will follow the radii equidistant to the radar and not a rectilinear grid. As the radar scans the glacier, the geometry between the radars antenna-beam and the front of the glacier changes as illustrated in Figure 4.

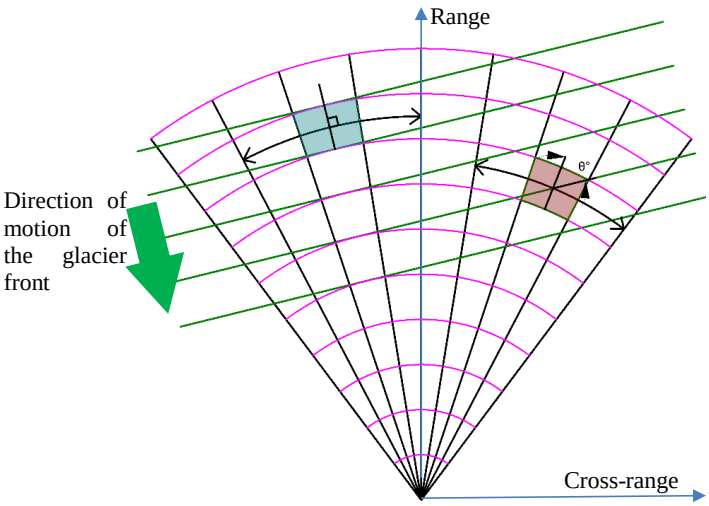

Figure 4. An illustration of the radar-glacier measurement geometry showing how a reflection from the glacier may appear in the radar data. The green arrow indicated the direction of motion of the glacier and the green lines indicate the orientation of the glacier front with respect to the location of the radar. The magenta coloured lines represent the radar range-resolution i.e. constant range from the radar. Two reflection points are illustrated by the blue and red squares. To calculate the actual flow of the glacier the measured speed must be adjusted by the corresponding offset angel between the direction of the radars antenna-beam and the flow direction of the glacier for all scan angles.

The measured glacier flow will be underestimated except from where the flow direction of the glacier is normal to the direction of the radars antenna-beam. All results presented in this paper are compensated for the scan-induced change in geometry.

The major reflections from the glacier are from the front and the many elevation steps at the crevasses are due to glacier flow. Due to the low angle between the incident electromagnetic field and the surface of the glacier few reflections are noticed, see Figure 5.

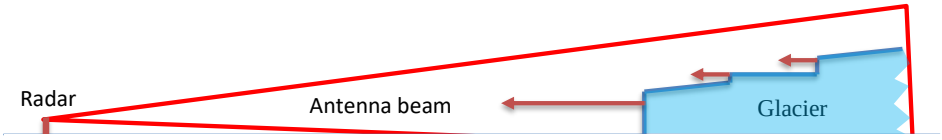

Figure 5 An illustration of the measurement set-up. The radar is located to the left and a schematic view of the glacier is to the right. The major reflections are from the front of the glacier and from the elevation steps at the crevasses.

3. Measurement resolution setup and radar parameters

In this chapter, we present and compare the spatial and temporal resolution of the measurement setup for the two locations used during the campaign. The first measurements were from Ny-Ålesund and the second from the headland Pynten closer to the glacier. We also describe the temporal resolution and the radar parameters.

(a) (b) (c)

Figure 6 Panel (a) shows a map of the Ny-Ålesund area. The red wedges show the measured spatial coverage of the radar from Ny-Ålesund and Pynten. Panel (b) shows an image of the radar on location at Pynten and panel (c) shows an image of the radar on location in Ny-Ålesund. The map is from www.svalbardkartet.npolar.no

3.1.Radar Parameters

The radar used is a coherent radar, which means we measure both amplitude and phase of the reflections. The radar operates at a centre frequency of 15.85 GHz (Ku-band). It has full polarimetric capability i.e. programmable independent transmit and receive polarization. This radar is capable of electronically scanning the antenna-beam in the horizontal plane from -50° to +50° with a pulse repetition frequency of up to 2 kHz giving high temporal and spatial resolution with sub millimetre displacement monitoring capability. Major radar parameters are listed in Table 1.

Table 1 Radar parameters.

Radar parameters	Parameter
Centre Frequency, [GHz]	15.85
Maximum Bandwidth, [MHz]	300
Maximum Pulse Repetition Frequency, [Hz]	2 000
Maximum Horizontal Scan Angle	±50°
Polarization	HH, VV, HV, and HV
Antenna 3 dB Beamwidth	3°
Minimum Scan Step in Azimuth	0.1°
Measurement Uncertainty, [mm]	< 0.1 (2σ)

The cross-range resolution of the radar is 3° (eq.2) and should not be mixed-up with the electronic step-size of the antenna. The angular step-size of 0.1° is analogous to oversampling in this case giving a maximum of 30 samples per real-aperture resolution.

3.2.Measurement Setup

3.2.1. Measurement geometry at Pynten – spatial resolution

Pynten (78.89° N, 12.34° E) is located approximately 9 km ESE of Ny-Ålesund (see Figure 6). The distance from the radar to the front of the glacier was measured by laser and varied from 5 675 m to 6 650 m from the near to the far end of the glacier front. The elevation of the radar was approximately 6 m AMSL. The radar was directed against the centre of the front of

Kronebreen, which gave a varying offset angle between the scan direction of the radar and the front of the glacier. The angle varied from approximately 1° close to Colletthøgda to approximately 31° at the crossing point between Kronebreen and Kongsvegen (see Figure 7). We scanned the full width of the glaciers and recorded data in range 5 to 7 km. Due to the offset angle between the radar and the front of the glacier, the up-glacier range recorded varied from 350 m in the southern end to 1 325 m in the northern end. To cover the full width of the glacier we scanned from -18° to +25° with an angular step size of 0.1°. The cross-range resolution was limited by the 3° beamwidth of the radar antenna, which gives a cross-range resolution of approximately 315 m. We scanned from left to right i.e. from Colletthøgda across Kronebreen and Kongsvegen to Grensefjellet (see Figure 7). Colletthøgda is the mountain north of Kronebreen limiting the glaciers northern extent. An angular step size of 0.1° equals a cross-range step resolution of approximately 10 meters at 5.7 km. The range resolution was 2 meters i.e. a radar bandwidth of 75 MHz. The total measured area was approximately 9 km^2.

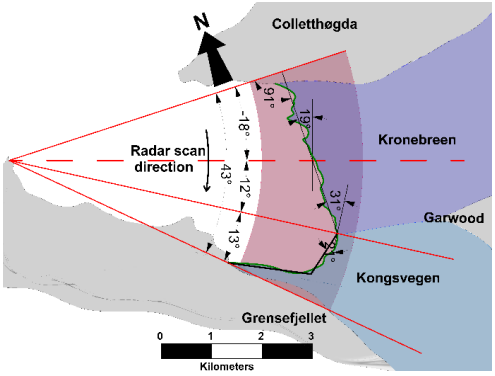

Figure 7 Illustration of the measurement setup at Pynten. The area illuminated by the radar is between the two outermost red lines. Only data within the red coloured annular sector was saved. The black line drawn along the front of Kronebreen is the baseline used to calculate the offset between the direction of the radar waves and the glacier front and is taken to be normal to the flow direction of the glacier. The glacier flows computed from the measurements are compensated by this offset angle. At the right-hand side, the offset is approximately 1° and at the conjoining point between Kronebreen and Kongsvegen the offset is approximately 31°.

3.2.2. Measurement geometry at Ny-Ålesund – spatial resolution

The distance from Ny-Ålesund to the front of Kronebreen was approximately 15 km. The elevation of the radar was approximately 10 m AMSL. The radar was directed against the centre of the front of Kronebreen, which gave a varying offset angle between the scan direction of the radar and the front of the glacier. The angle varied from approximately 14° close to Colletthøgda to approximately 25° at the crossing point between Kronebreen and Kongsvegen (see Figure 8). We scanned from left to right i.e. from Colletthøgda across Kronebreen to Kongsvegen (see Figure 8 for place names and locations). To cover the full width of the glacier we scanned from –4° to +13° with an angle step size of 0.1°. The cross-range resolution was limited by the 3° beamwidth of the radar antenna, which gives a cross-range resolution of approximately 785 m. We scanned the full width of the glaciers and recorded data from 14.5 km to 29.5 km. The range resolution used was 5 meters i.e. a radar bandwidth of 30 MHz. The total measured area was approximately 98 km^2. Figure 6 panel (c) shows an image of the radar on location at Ny-Ålesund.

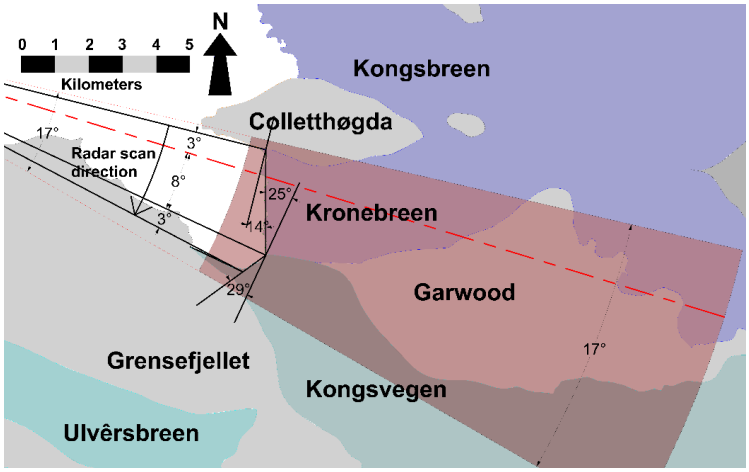

Figure 8 An illustration of the measurement setup at Ny-Ålesund. The area illuminated by the radar is between the two outermost red lines. The red dotted line indicates the zero angle of the radar antenna. Only data within red coloured annular sector was saved. The black line drawn along the front of Kronebreen is the baseline used to calculate the offset between the direction of the radar waves and the glacier front and is taken to be normal to the flow direction of the glacier. The glacier flows computed from the measurements are compensated by this offset angle. At the northern end of Kronebreen the offset angle is approximately 1° and at the conjoining point between Kronebreen and Kongsvegen the offset is approximately 25°.

3.2.3. Temporal resolution

To reduce the amount of data collected we scanned the glacier every twelfth second from Pynten and every eleventh second from Ny-Ålesund, giving a temporal resolution of approximately 5 images per minute. This trade-off between the image rate and the amount of data produced by the radar limits the maximum measurable unambiguous velocity to approximately 27.3 m/day, (eq.7). This should be fast enough to detect the onset of calving events. From previous measurements of Kronebreen [22] the maximum expected ice velocity, excluding frontal calving is ~4 m/day.

A comparison between the two measurement setups is presented in Table 2.

Table 2 Comparison of the two measurement setups.

Location	Height of radar (AMSL)	Angular step size	Radar-glacier distance	Range resolution	Spatial resolution	Area of one pixel / cell	Temporal resolution
Pynten	6 m	0.1°	~6 km	2 m	315 m	628 m^2	12 s
Ny-Ålesund	10 m	0.1°	~15 km	5 m	785 m	3927 m^2	11 s

4. Results

In this section, we present and compare the results from Pynten and the results from Ny-Ålesund.

4.1. Measurements from Pynten

The measurements from Pynten were made from the 15 September 18:30 to the 16 September 2017 08:30. Weather data was collected at the radar site during the measurements. The maximum amplitude of the reflected energy from all the collected images for all range-cells and angles was superimposed on to an image from the Sentinel-2 satellite. The satellite image was acquired four days prior to the measurements and the results show good agreement between the maximum reflection measured by the radar and the outline of the front of the glacier from the satellite image, see Figure 9.

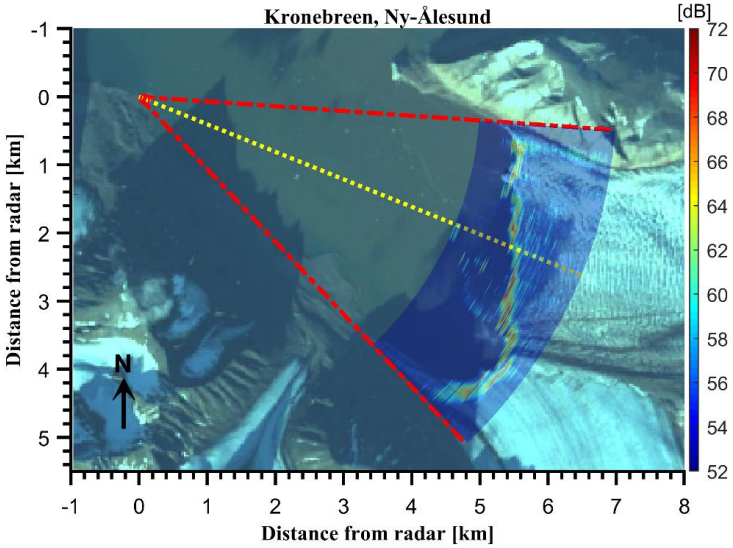

Figure 9. Maximum measured reflected energy from Kronebreen and Kongsvegen glaciers superimposed on a satellite image from the Sentilel-2 satellite. Note that the satellite image is from the 12th of September while the measurements are from the 15th and 16th of September 2017. The yellow line indicates the centre line of the radars look direction. The two red lines indicate the area mapped by the radar. The plot also shows the path of some icebergs floating just south of the centre line. The Sentinel-2 image is from the European Space Agency (ESA).

The front of the glacier is easily detectable from the radar amplitude data in Figure 9. Reflections from the step pattern of the crevassed glacier surface are also clearly visible making it possible to track the motion. The amplitude of the reflected energy from the front of the glacier is approximately 10 dB above the amplitude of the reflected energy from the crevasses. The distance to the front of the glacier determined with the radar measurements correlates well with the distance measured by the laser rangefinder. The outline of the glacier front mapped by the radar is also in good accordance with the glacier front found on the satellite image of the Ny-Ålesund area. This shows that we are able to identify the reflections from the glacier and map the radar data to the physical location on the glacier.

4.1.1. Path Length Variation and Radio Refractivity

To correct for variations in the radio refractivity a fixed point on Colletthøgda with a stable amplitude was used as a reference. This was due to the variation in radio refractivity calculated from the meteorological data showed little resemblance with the measured path-length variation from the fixed-point at Colletthøgda. The variation in path-length between the radar and the fixed point during the measurement reached a maximum of ±6 mm.

4.1.2. Flow speed of the glacier

The maximum flow speed of the glaciers using all collected images was calculated using interferometry. The measured flow is superimposed on to a satellite image from the Sentinel-2 satellite, presented in Figure 10.

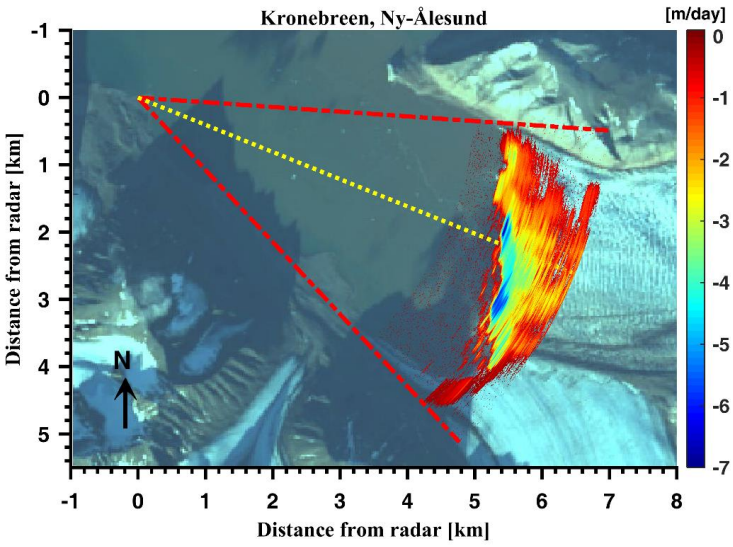

Figure 10 Flow of Kronebreen and Kongsvegen glaciers calculated using interferometry superimposed on to a satellite image from the Sentinel-2 satellite. The data presented is the maximum-recorded flow using all images. The highest flow observed is in the central part of Kronebreen along the front, where the maximum speed recorded is 7 m/day. This could be either a calving onset, a rotational motion of a block of ice, or a crevasse opening. The Sentinel-2 image is from the European Space Agency (ESA).

Figure 10 shows how the speed varies across the glacier. The highest flow observed is along the front in the central part of Kronebreen, decreasing towards the edges and up-glacier, which is in accordance with results from previous measurements [22]. The blue coloured areas indicate high flow rates, which is probably calving onsets or rotational motion of large blocks of ice. Kongsvegen showed little motion during the measurments. Figure 11 shows the accumulated measured flow of Kronebreen in increments of two hours.

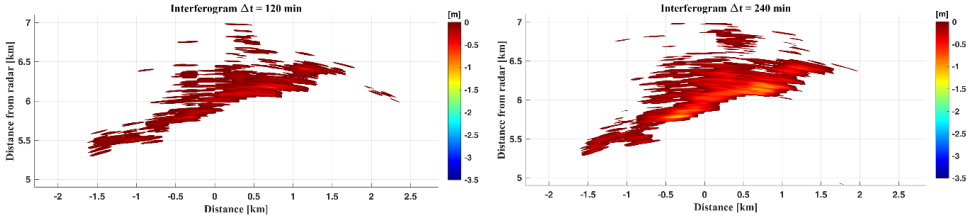

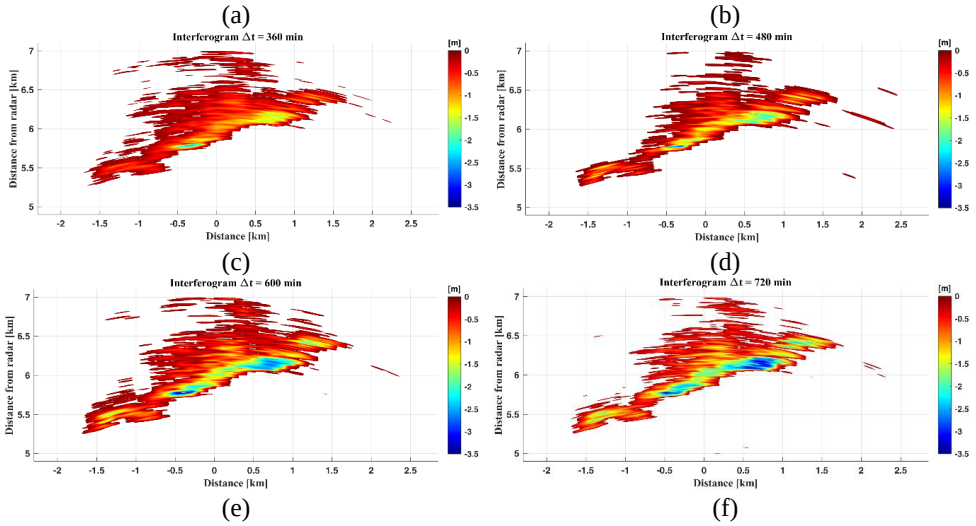

Figure 11 Measured accumulated flow of Kronebreen as a function of time. Elapsed time: (a) 2 h, (b) 4 h, (c) 6 h, (d) 8 h, (e) 10 h, and (f) 12 h.

Figure 11 shows the measured flow of Kronebreen at selected time intervals: (a) 2 h, (b) 4 h, (c) 6 h, (d) 8 h, (e) 10 h, and (f) 12 h. All points are selected based on their temporal stability with a coherence $\gamma = 0.75$.

Due to the high spatial and temporal resolution of the radar, detailed time-displacement profiles and range- displacement information is available for detailed analysis. Figure 12 shows time-displacement profiles for a radar scan angle of -2.1° in 20-meter increments from the front of Kronebreen.

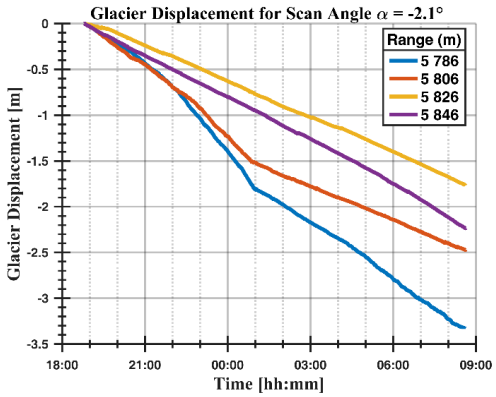

Figure 12. Comparison of the measured displacement of Kronebreen for four different ranges in 20-meter increments. This represents the displacement through one range-cell. The blue line is the front of the glacier 5 786 m from the radar. At this range, we have an increase in the flow speed from 10 p.m. to 1 a.m. then the displacement decreases. The same trend is visible at 5,806 m (red line) while at range 5 826 m (yellow line) and 5 846 m (purple line) the displacement is close to linear during the measurements.

The time- displacement profile in Figure 12 shows the temporal variation recorded for the frontal zone of Kronebreen. The front is at a range of 5 790 m. An increase in the displacement

is observed from the beginning of the measurements until about 01 h and then the displacement decreases. This indicates a calving onset or a rotational motion of a block of ice. Further up-glacier the displacement is relatively linear between.

4.2.Measurements from Ny-Ålesund

Measurements were made from Ny-Ålesund to test the long-distance capability of the radar. The measurements from Ny-Ålesund were made from the 14 September 2017 19:30 to 15 September 2017 09:30. During the measurements, weather data was collected at the Norwegian Polar Institutes (NPI) weather station at Pynten, located approximately 2/3 of the distance from the radar to the glacier front. This data was kindly made available for us by NPI.

4.2.1. Path Length Variation and Radio Refractivity

The radar measurement set-up in Ny-Ålesund covered the range 14.5 to 29.5 km at Kronebreen. The intention was to find one or more stable reflection points on the mountains and use it as a reference to correct the measurements for variations in the radio refractivity. The four mountains covered were Colletthøgda, Garwoodtoppen, Pretender and Dronningfjella (see Figure 6). We found multiple points at Colletthøgda and Garwoodtoppen with stable amplitudes and phases. The variation in path-length between the radar and these stable points during the measurements are shown in Figure 13, along with variations in path-length due to radio refractivity calculated from the metrological data from NPI.

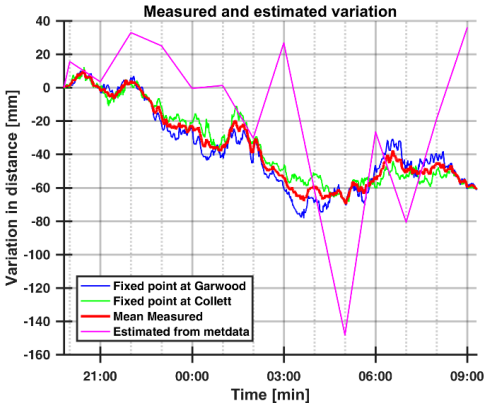

Figure 13 Temporal variation of the path-length between the radar and two fixed points one on Colletthøgda (green line) and one on Garwoodtoppen (blue line) during the measurements as a function of time. The distances between the radar and the fixed points are 14 835 m and 19 185 m. The maximum variation is approximately 82 mm at Colletthøgda, and approximately 88 mm at Garwood. The two fixed points are marked with a red circle (Colletthøgda) and a green circle (Garwood) in Figure 14.

The variation in radio refractivity calculated from the meteorological data showed little resemblance with the measured path-length variation from the two fixed-points. The variation in path-length between the radar and the fixed points during the measurement reach a maximum of approximately 82 mm at Colletthøgda and approximately 88 mm at Garwood. The mean variation in path-length between the radar and these two points were used to correct for the radio refractive induced path-length variation for all data collected.

4.2.2. Flow speed of the glacier

The flow speeds of the glacier were calculated using interferometry and the results are overlaid by a satellite image of the Ny-Ålesund area see Figure 14.

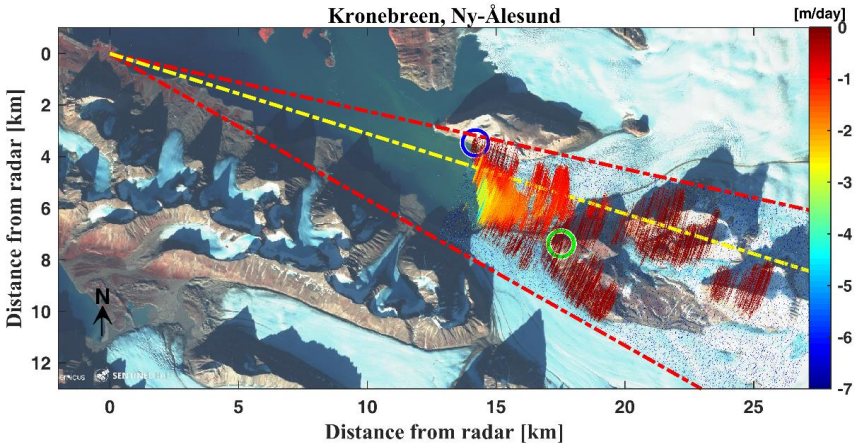

Figure 14 Interferometric calculated flow speed overlaid a satellite image of the scanned area. The blue and green circles indicate the location of the two selected points used to correct for variations in radio refractivity at Colletthøgda and Garwood. The Sentinel-2 image taken on 13 September 2017 is from the European Space Agency (ESA).

Like in the results from Pynten we observe the highest flow at the front and in the middle of the glacier decreasing towards the edges and up-glacier. The selected reference points at Garwoodtoppen and Colletthøgda used for correction of radio refractivity are marked with a red and a green circle in the Figure 14. Figure 15 shows the measured flow of Kronebreen in increments of two hours.

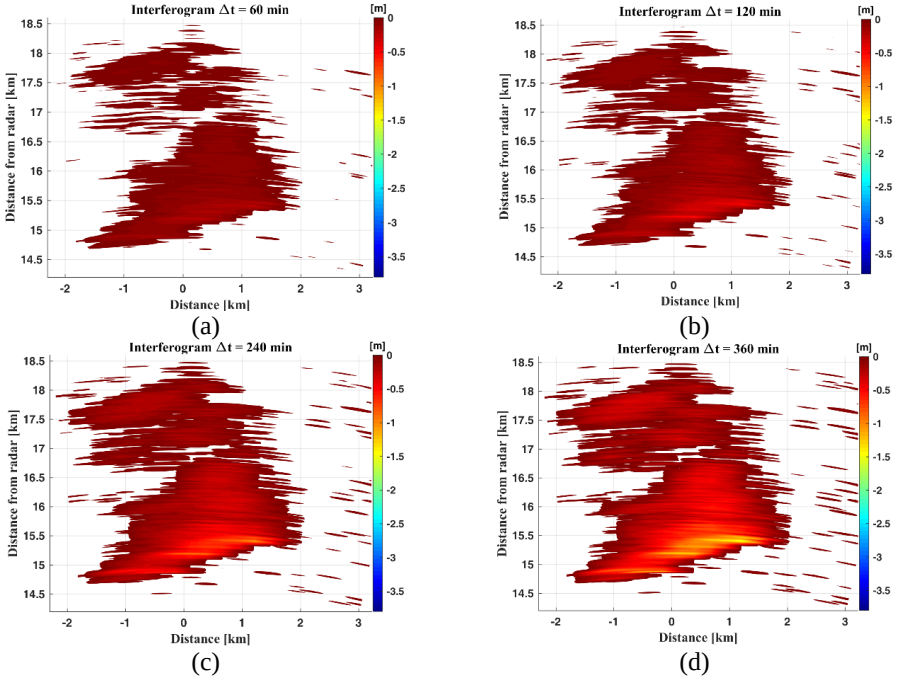

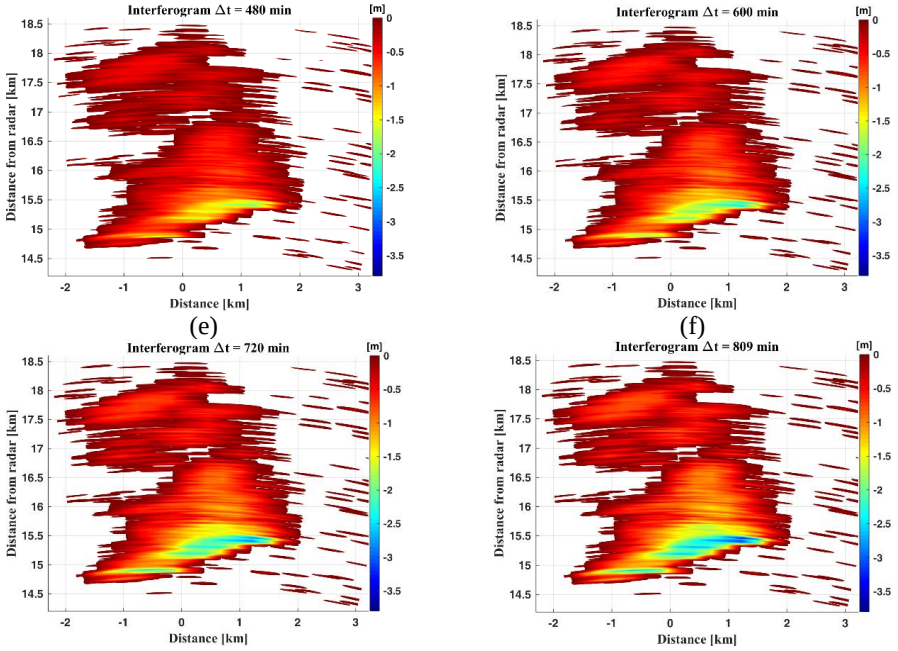

Figure 15 Measured accumulated flow of Kronebreen as a function of time. Elapsed time: (a) 1h, (b) 2h, (c) 4 h, (d) 6h, (e) 8 h, (f) 10h, (g) 12h, and (h) 13h and 29 min.

Figure 16 shows time-displacement profiles for a fixed radar scan-angle of 0° in 20-meter increments from the front of Kronebreen and up-glacier.

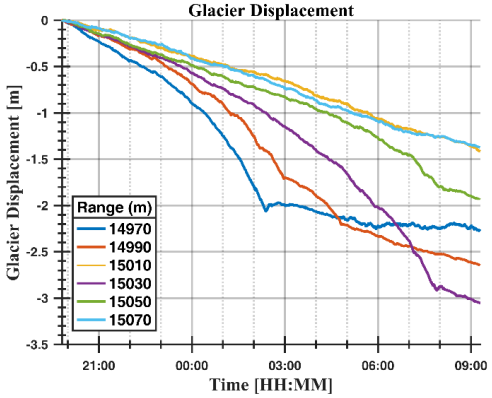

Figure 16 Glacier displacement as a function of time for six different ranges in 20-meter increments for the front of Kronebreen. This represents the displacement through one range-cell. The blue line is the front of the glacier 14 970 m from the radar. For this cell, we have an increase in flow speed from the beginning of the measurements to 2 a.m. The same trend is visible at the other cells except for ranges 15 000 m and 15 010 m, which showed close to linear displacement during the measurements.

Temporal information of the flow through six range-cells from range 14 970 to 15 070 m from the radar is shown in Figure 16. The blue line shows how the flow increases in the hours before an event, which is believed to be a calving onset or rotational motion of a large block of ice. A

second event is detected about 5 hours later at a range of 15 030 m. The second event appears to take place 50 m up-glacier from the first event; however, it is believed to take place at the front of the glacier south of the first event. This is due to a combination of the radar-glacier measurement geometry and the cross-range resolution of the radar. First, the glacier front is not straight, and the glacier front is oblique to the radar line of sight. Second, the 3-dB beamwidth of the antenna equals a cross-range resolution of 785 m at 15 km. This means we cannot distinguish between events more closely spaced than 785 m along the glacier front, consequently we are likely to capture multiple events along the front of the glacier per scan angle.

4.3.Comparison of velocity measurements

In this section the measured flow speed obtained from the two sites are compared. The difference in flow speed between the two locations is highlighted in Figure 17.

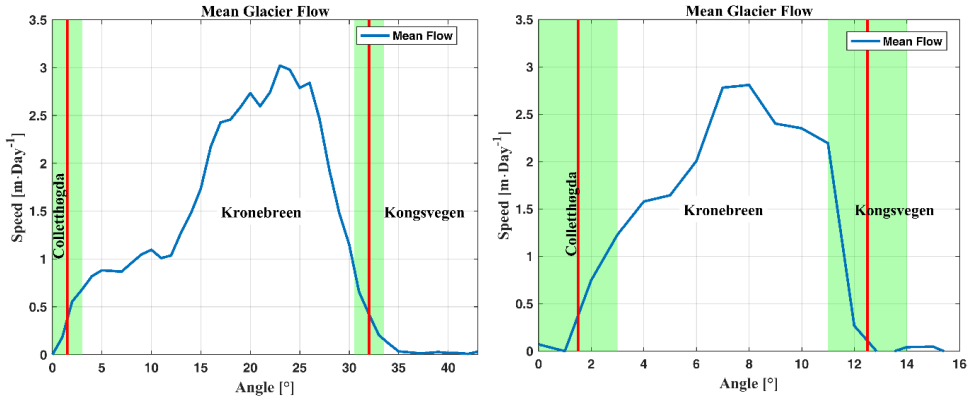

(a) (b)

Figure 17. Determined mean glacier flow as a function of radar scan angle. Note different spatial resolution on the two horizontal axes of the panels. Panel (a) show the mean flow over near 12 h 15 September 2017 from the front and 300 m up-glacier measured from Pynten. Panel (b) show the mean flow over near 13 h at 14 September 2017 measured from Ny-Ålesund. From the left-hand side is Colletthøgda showing no motion. The data presented are mean values measured for all collected data-images from both sites.

Figure 17 shows the measured mean glacier flow from the glacier front and 300 m up-glacier. Measurements from Pynten shows a flow varying from 0.4 m/day to 3 m/day (panel a) and measurements from Ny-Ålesund shows a flow varying from 0.4 m/day to 2.8 m/day (panel b). The flow speed is compensated for the offset in the measurement geometry. The measurements are made in the period from September 14 to 16, 2018, each measurement spanning approximately 12 and 13 hours.

4.4.Comparison with previous radar measurements

We have reprocessed the radar data acquired in 2008 [22] to compare it with the measurements made in 2017. The 2008 measurements were made from Pynten with a GB-RAR operating at C-band with a PRF of approximately 1 Hz. The measurements lasted for 92 hours. For the reprocessing a time span of 13 hours including a calving event was chosen, for comparison to the near 13 hours of measurements in 2017, see Figure 18.

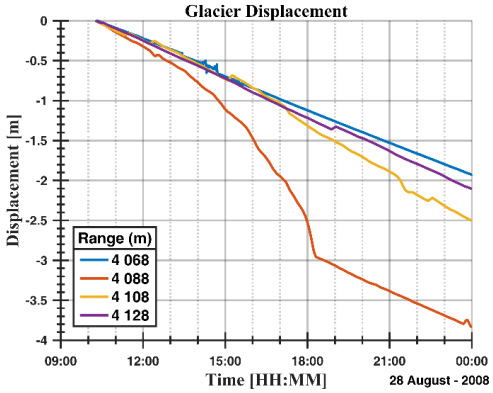

Figure 18 Glacier displacement measured august 2008 from Pynten. The data is comparable with the data given in Figure 12, note that the glacier front has retreated more than 1.5 km from 2008 to 2017.

Continuous visual observations were made of the glacier and all calving events were manually recorded and classified during the 2008 campaign [27]. The visual dataset confirmed a calving event shown in the red line at 18:00 h, see Figure 18.

5. Discussion

The measurement experiment clearly demonstrates the potential of the electronic scanning radar system in achieving a combination of high temporal and spatial resolution data of glacier flow. We were able to establish a detailed map of the glacier flow during a short observation time. With a permanent installation of a monitoring radar the diurnal, seasonal, and inter-annual variations of glacier flow can be revealed. The influence of environmental effects like tide, ocean and air temperature on calving rates may then be analysed. However, some issues must be discussed further to develop an optimal monitoring radar system.

The attenuation of the electromagnetic waves due to hydrometeors is still an unanswered question. The attenuation depends on the rate of precipitation, path-length of the electromagnetic wave through the precipitation and the radars operating frequency [28]. During the measurement campaign there was stable dry weather and variations in attenuation could not be studied. In a study of short-range surveillance radars, the optimum operating frequency for ranges up to 20 km was found to be 15 GHz [29]. Measurement experiments in Ny-Ålesund during varied weather conditions should be conducted.

Coherence between consecutive measurements is required for interferometric calculations, as described in eq.5. High temporal resolution is beneficial for high coherence of sequential measurements. In our measurement experiment, only data from reflection points fulfilling the selection criterion outlined in section 2.3, eq.9 were included or excluded dynamically depending on coherence. In addition, all range-cells returning motion above $\lambda/4$ between two successive measurements were discarded to reduce accumulation of errors. A benefit of high temporal sampling is the simplified phase unwrapping between consecutive images, as both geometrical displacements and atmospheric decorrelation will be small, preferably less than a quarter of a wavelength. It should be investigated further if the cut-off value (eq.9) can be lowered with even higher temporal resolution of the measurement, or if the length of the moving average filter can be increased.

Radio refractivity influences the velocity of the electromagnetic waves and the best practical correction method must be determined and applied to the calculated interferometric glacier flow data. The measured and estimated variation in radio refractivity presented in Figure 13 suggests that meteorological data from a single station is insufficient to make corrections for the variations in radio refractivity. The meteorological model assumes homogeneous atmospheric conditions along the path of the electromagnetic waves. Local katabatic glacier winds [30] may create inhomogeneous conditions, and the spatial distribution of the calculated corrections may be inadequate for path length corrections. Fixed points with stable reflections on the mountains were assessed, as shown in Figure 13, and used to compensate for the variations in the radio refractivity. All results are compensated for atmospheric variation measured at the fixed points. With this method the variation in radio refractivity between the radar and the glacier is eliminated but not the variation across the glacier. The weakness of the applied method is therefore the assumption of a homogeneous atmosphere across the glacier yielding a uniform correction of the data. In the case of a permanent installation or a longer measurement period, it would be beneficial to have a reference reflector close to the glacier, giving a stable reference for corrections of variations in the radio refractivity [7] and a reflector close to the radar for self-monitoring of the radar [31].

Estimates of measurement uncertainty are based on relative observations of the distance to the fixed points on the mountains. We used the measured mean value from the two points to correct for the variation in radio refractivity and the deviation from this mean value to the actual measured value is used as the estimated uncertainty of the calculated flow. From the measurements from Ny-Ålesund, the median deviation was found to be approximately ±12 mm, while the mean flow was between 0.4 to 2.8 m, which represents 0.4% to 3% of the mean glacier flow of the front. For the measurements from Pynten the total variation due to radio refractivity was approximately ±6 mm, while the mean measured flow was between 0.4 to 3.0 m, which represents 0.2% to 1.5% of the flow. The estimated measurements uncertainty thus represents a small portion of the total measured flow.

Calving events can be identified in the high spatial and temporal sampled data set. With the measurement setup used in 2008, the maximum unambiguous velocity was ~1150 m/day. With that setup, calving onsets were identified by the accelerating phase in the hours before failure and, in most cases, calving could be verified by greatly reduced reflection from the range-cell associated with the loss of ice. From the 2008 measurements, we know that the red line in Figure 18 represents a calving event. If we compare this event with the events represented by the blue line in Figure 12 and the blue and purple lines in Figure 16 there is a strong indication that we have captured two calving events in the measurements from Ny-Ålesund and one calving event from Pynten. High temporal sampling of data makes it possible to detect calving events and time series thereof, which are useful for glacier dynamics studies and for warning ship traffic in the Arctic of icebergs.

Glacier flow measurements show as expected the highest velocity in the front of the glacier. This is where the radar measurements with high temporal rate may have recorded rotational movement of ice blocks. The accumulated flow measured from Pynten is presented in Figure 11, and for Ny-Ålesund in Figure 15. The highest flow at the terminus of the glacier is probably due to calving onsets or rotational motion of large portions of ice. We have presented accumulated flow for a period using high temporal resolution data. Our presented terminus velocities may therefore be higher than average values determined by methods with lower temporal resolution, as e.g. satellite systems.

Comparison of our measurements conducted at Pynten and Ny-Ålesund shows some deviation in the spatial distribution on the glacier of the determined mean flow see Figure 17. The measurements from Pynten show a mean glacier flow varying from 0.4 m/day close to Colletthøgda reaching a maximum of 3 m/day in the central area before decreasing to 0.4 m/day along Kongsvegen, while the measurements from Ny-Ålesund show that the glacier flow varies from 0.4 m/day close to Colletthøgda reaching a maximum of 2.8 m/day in the central area before decreasing to 0.2 m/day along Kongsvegen. The mean flow of the first 300 m of the glacier is 1.66 and 1.72 m/day from Pynten and Ny-Ålesund respectively. The differences might be due to short observation time, measurements at two different days, or/and different spatial resolution. The glacier cross-range resolution when measuring from Ny-Ålesund is 780 m, and 315 m from Pynten, and the range-resolution is 5 m in the measurements from Ny-Ålesund and 2 m from Pynten. This results in a radar footprint of 3 900 m^2 when measuring from Ny-Ålesund and 628 m^2 when measuring from Pynten, thus the mean values are calculated over different spatial scales. The mean flow calculated from the measurements at Pynten and Ny-Ålesund corresponds well despite the short observation time and different measurement set-up.

With knowledge of the height profile of the glacier, the determined velocities can be used to make an estimate of the calving volume of Kronebreen. The mean estimated flow of the first 300 m of the glacier can be used to make a rough estimate of the area lost by calving per day; the width of Kronebreen is approximately 3.1 km, resulting in a loss between 1.55 to 1.60 km^2/day. These calving volume estimates can be conducted on varying timescales, in this experiment they are down to 11 s.

A near real-time monitoring system can be optimised for glacier calving studies. An advantage of radars with an electronically steered antenna is its ability to change the angle of view dynamically from pulse-to-pulse. If we detect accelerating flow, it might be the onset of a calving event and the antenna can be electronically directed to this area for higher temporal mapping. Machine learning algorithms or statistical signal processing can help automate the identification of calving-onsets by recognising the behaviour prior to a calving event, similar to what is performed on time-lapse imagery [32]. Steering the antenna towards calving events may be combined with radar monitoring of the whole glacier, but this will cause a trade-off between the temporal rate needed to follow the motion of the calving and the resources needed for continuous monitoring the rest of the glacier. In this study, we used a prototype radar with a 32 cm antenna giving a cross-range resolution of 3°. After these experiments, ISPAS has produced a new series of radars with 96 cm antennas, which give a 1° cross-range resolution. This radar would give three times the spatial resolution compared to the prototype radar. The temporal resolution during the measurements was also limited to reduce the size of the radar data acquired because the radar data had to be process off-line after the measurements. In the new production model, radar data is processed on-line in a dedicated field programmable gate array (FPGA). Using a full-scale antenna and an angular step-size of half the cross-range resolution (0.5°) this would require 42 steps from Pynten and 24 steps from Ny-Ålesund to map the Kronebreen glacier. The temporal resolution would be 83 and 47 images per second from Ny-Ålesund and Pynten respectively. A further developed and matured radar system with high temporal sampling rate should be useful for both glacier flow and calving dynamics studies and for iceberg warnings for ship traffic.

The location of the radar determines the size of the covered measurement area, and the spatial resolution. The major returned radar reflections in the measurement scene are from the glacier front. This is due to the shallow angle between the radar-waves and the surface of the glacier, see Figure 5. This applies to both Ny-Ålesund and Pynten but is most evident in the measurements from Pynten where there are little or no reflections in the area close to

Colletthøgda see Figure 9. One way to increase the illumination of the shaded areas of the glacier is to elevate the radar. This might not be practically feasible in the area around Pynten, but in Ny-Ålesund, there is infrastructure on the Zeppelin Mountain just south of the settlement. Locating the radar at the Zeppelin Mountain at a height of approximately 480 m AMSL, as opposed to 10 m AMSL in Ny-Ålesund, would increase the radars grazing angle from ~0.04° to ~1.8°. Elevating the radar will improve the reflections from the up-glacier surface. We have inspected the facilities on the Zeppelin Mountain and found it suitable for a permanent radar installation. Locating the radar here would facilitate monitoring of the calving fronts of four glaciers; Blomstrandbreen, Conwaybreen, Kronebreen, and Kongsvegen. This would make it possible to compare inter-glacial variation in flow speed.

6. Conclusion

We have made a suitability study of Ny-Ålesund as a site for permanent installation of a glacier monitoring terrestrial radar. We have successfully used a coherent high-temporal resolution ground-based interferometric radar with an electronically steered antenna for measuring the Kronebreen glacier. Measurement results show that the radar can map the flow of the glacier with a high temporal and spatial sampling rate and laterally position major calving onsets. The high temporal sampling rate of the radar makes it possible to extract detailed information of the glacier flow and calving onsets.

The measurements were corrected for variations in the radio refractivity by monitoring the variation in distance to fixed points on the mountains Colletthøgda and Garwood. By adjusting the radar measurements for the variation in radio refractivity the maximum uncertainty of the glacier flow was estimated to be 1.2% of the measured flow.

Detailed surface velocity maps created for Kronebreen shows a spatial variation in flow with the highest flow in the central part of the front of the glacier slowing down towards the edges and up-glacier. The cross-range resolution was limited due to the 3° antenna beamwidth of the prototype radar. The determined velocity field agrees well with previous published measurements by others.

We have measured the glacier from two locations: Pynten 5 km from the glacier front and Ny-Ålesund 15 km from the glacier front. The main difference in the results from the two locations is the cross-range resolution, which is linked to the distance. The distance from Ny-Ålesund to the front of Kronebreen is three times the distance from Pynten to Kronebreen and the resulting cross-range resolution is then one third. Using a physically larger antenna when measuring from Ny-Ålesund can compensate this. In this case, an antenna with one-third beamwidth would give equal resolution as the measurements made from Pynten.

Selected data acquired from Pynten and Ny-Ålesund is compared to a known calving event recorded in 2008. The flow-pattern and registered phase development in the hours before calving show similarities in the two data sets, which strongly suggests that we are able to detect calving onsets with the radar. Based on the calculated mean glacier flow and the width of the glacier a rough estimate of the daily area of ice lost is between 1.55 and 1.60 km^2/day.

Changes in radar parameters and temporal rate should be investigated further in connection to coherence and attenuation to improve interferometric calculations and accuracy of the glacier velocity. The measurements show that the tested technology is suited for real-time monitoring with detection of calving onsets and detailed flow information. The system should be optimised and developed further in regard to real-time data processing and antenna steering.

Being able to measure from Ny-Ålesund, preferably Zeppelin Mountain is beneficial for a permanent installation of a glacier monitoring system, as all necessary infrastructure present in Ny-Ålesund significantly simplifies the installation and maintenance. Another benefit is the number of glacier-fronts visible from the Zeppelin Mountain, allowing one radar to monitor the flow of the four glaciers Kongsbreen, Kronebreen, Conwaybreen, and Blomstrandbreen.

Acknowledgements

The work was supported by the Research Council of Norway. The fieldwork was made possible through Svalbard Science Forum (RiS ID 10878, 2D Velocity Mapping of Glaciers), the Norwegian Polar Institute and Kings Bay AS.

Bibliography

[1] Scambos, Bell, Alley, Anandakrishnan, Bromwich, Brunt, Christianson, Creyts, Das, DeConto, Dutrieux, Fricker, Holland, MacGregor, Medley, Nicolas, Pollard, Siegfried, Smith, Steig, Trusel, Vaughan and Yager, "How much, how fast?: A science review and outlook for research on the instability of Antarctica's Thwaites Glacier in the 21st century," *Global and Planetary Change,* vol. 153, pp. 16-34, 2017.

[2] J. L. Bamber, R. M. Westaway, B. Marzeion and B. Wouters, "The land ice contribution to sea level during the satellite era," *Environmental Research Letters,* vol. 13, no. 6, p. 063008, June 2018.

[3] J. E. Box, T. C. Colgan, B. Wouters, D. O. Burgess, S. O'Neel, L. I. Thomson and J. S. Haugaard Mernild, "Global sea-level contribution from Arctic land ice: 1971 to 2017.," *Environmental Research Letters,* vol. 13, no. 12, p. 125012, 2018.

[4] T. Moon, A. Ahlstrøm, H. Goelzer, W. Lipscomb and S. Nowicki, "Rising Oceans Guaranteed: Arctic Land Ice Loss and Sea Level Rise," *Current Climate Change Reports,* vol. 4, no. 3, pp. 211-222, 2018.

[5] A. Luckman, D. I. Benn, F. Cottier, S. Bevan, F. Nilsen and M. Inall, "Calving rates at tidewater glaciers vary strongly with ocean temperature.," *Nature Communications,* vol. 6, p. 6:8566 doi: 10.1038/ncomms9566, 2015.

[6] H. Zebker, P. Rosen and S. Hensley, "Atmospheric effects in interferometric synthetic aperture radar surface deformation and topographic maps," *Journal of Geophysical Research,* vol. 102, pp. 7547-7563, 1997.

[7] R. Gundersen, R. Norland and C. Rolstad Denby, "Ground-based differential interferometric radar monitoring of unstable mountain blocks in coastal environment," *Remote Sensing,* 2018.

[8] N. Dematteis, G. Luzi, D. Giordan, F. Zucca and P. Allasia, "Monitoring Alpine glacier surface deformations," *Remote Sensing Letters,* vol. 8, no. 10, pp. 947-956, 2017.

[9] J. López-Moreno, E. Alonso-González, O. Monserrat, L. Del Río, J. Otero, J. Lapazaran, G. Luzi, N. Dematteis, A. Serreta, I.-C. Rico, M. Bartolomé, A. Moreneo, S. Buisan and J. Revuelto, "Ground-based remote-sensing techniques for diagnosis of the current state and recent evolution of the Monte Perdido Glacier, Spanish Pyrenees," *Journal of Glaciology,* pp. 1-16, 2018.

[10] E. Rignot, B. Hallet and A. Fountain, “Rock glacier surface motion in Beacon Valley, Antarctica, from synthetic-aperture radar interferometry,” *Geophysical Research Letters,* vol. 29, no. 12, pp. 48-1 48-4, 2002.

[11] C. Werner, T. Strozzi, A. Wiesmann and U. Wegmüller, “A Real-Aperture Radar for Ground-Based Differential Interferometry,” in *IGARSS 2008 - 2008 IEEE International Geoscience and Remote Sensing Symposium*, 2008.

[12] T. Strozzi, C. Werner, A. Wiesmann and U. Wegmüller, “Topography Mapping With a Portable Real-Aperture Radar Interferometer,” *IEEE Geoscience and Remote Sensing Letters,* vol. 9, no. 2, pp. 277-281, 2012.

[13] L. Noferini, D. Mecatti, G. Macaluso, M. Pieraccini and C. Atzeni, “Monitoring of Belvedere Glacier using a wide angle GB-SAR interferometer,” *Journal of Applied Geophysics,* vol. 68, no. 2, pp. 289-293, 2009.

[14] D. Voytenko, T. Dixon, C. Werner, N. Gourmelen, I. Howat, P. Tinder and A. Hooper, “Monitoring a glacier in southeastern Iceland with the portable Terrestrial Radar Interferometer,” in *2012 IEEE International Geoscience and Remote Sensing Symposium*, 2012.

[15] S. Xie, T. Dixon, D. Voytenko, F. Deng and D. Holland, “Grounding line migration through the calving season at Jakobshavn Isbræ, Greenland, observed with terrestrial radar interferometry,” *The Cryosphere,* vol. 12, pp. 1387-1400, 2018.

[16] D. Voytenko, T. H. Dixon, D. M. Holland, R. Cassotto, I. Howat, M. A. Fahnestock, M. Truffer and S. de la Peña, “Acquisition of a 3 min, two-dimensional glacier velocity field with terrestrial radar interferometry,” *Journal of Glaciology,* vol. 63, no. 240, pp. 629-636, 2017.

[17] P. L. Heinselman and S. M. Torres, “High-Temporal-Resolution Capabilities of the National Weather Radar Testbed Phased-Array Radar,” *Journal of Applied Meteorology and Climatology,* vol. 50, no. 3, pp. 579-593, 2011.

[18] D. Notz and J. Stroeve, “The Trajectory Towards a Seasonally Ice-Free Arctic Ocean,” *Current Climate Change Reports,* vol. 4, no. 4, pp. 407-416, 2018.

[19] B. Lefauconnier, J. O. Hagen and J. P. Rudant, “Flow speed and calving rate of Kongsbreen glacier, Svalbard, using SPOT images,” *Polar Research,* vol. 13, no. 1, pp. 59-65, 1994.

[20] A. Kääb, B. Lefauconnier and K. Melvold, “Flow field of Kronebreen, Svalbard, using repeated Landsat 7 and ASTER data,” *Annals of Glaciology,* vol. 42, pp. 7-13, 2005.

[21] T. Schellenberger, A. Dunse, A. Kääb, J. Kohler and C. Reijmer, “Surface speed and frontal ablation of Kronebreen and Kongsbreen, NW Svalbard, from SAR offset tracking,” *The Cryosphere,* no. 9, pp. 2339-2355, 2015.

[22] C. Rolstad Denby and R. Norland, “Ground-based interferometric radar for velocity and calving-rate measurements of the tidewater glacier at Kronebreen, Svalbard,,” *Annals of Glaciology,* vol. 50, no. 50, pp. 47-54, 2009.

[23] N. Levanon, Radar Principles, Tel-Aviv: John Wiley & Sons, 1988.

[24] C. Chen and H. A. Zebker, “Phase unwrapping for large SAR interferograms: statistical segmentation and generalized network models.,” *IEEE Transactions of Geoscience and RemoteSensing,* vol. 40, no. 8, pp. 1709-1719, 2002.

[25] R. Hanssen, Radar Interferometry: Data Interpretation and Error Analysis., Dordrecht: Kluwer Academic Publishers, 2002.

[26] P. Berardino, G. Fornaro, R. Lanari and E. Sansosti, “A New Algorithm for Surface Deformation Monitoring Based on Small Baseline Differential SAR Interferograms.,” *IEEE Transactions on Geoscience and Remote Sensing,* vol. 40, no. 11, pp. 2375-2383, 2002.

[27] A. Chapuis, C. Rolstad and R. Norland, “Interpretation of amplitude data from a ground-based radar in combination with terrestrial photogrammetry and visual observations for calving monitoring of Kronebreen, Svalbard,” *Annals of Glaciology,* vol. 51, no. 55, pp. 34-40, 2010.

[28] P. Karamakar, Microwave Propagation and Remote Sensing, Atmospheric Influences with Models and Applications, 1 ed., CRC Press, 2011, p. 257.

[29] C. Baker and B. Trimmer, “Short-range surveillance radar systems,” *Electronics and Communication Engineering Journal,* vol. 12, no. 4, pp. 181-191, 2000.

[30] V. Kotlyakov and M. Grosswald, Eds.“Chapter 10: Effect on individual glaciers on climate,” *Polar Geography and Geology*, pp. 217-240, 2008.

[31] R. Gundersen, R. Norland and C. Rolstad Denby, “Geometric, Environmental and Hardware Error Sources of a Ground-Based Interferometric Real-Aperture FMCW Radar System,” *Remote Sensing,* vol. 10, no. 12, 2018.

[32] D. Vallot, S. Adinugroho, R. Strand, P. How, R. Pettersson, D. I. Benn and N. R. J. Hulton, “Automatic detection of calving events from time-lapse imagery at Tunabreen, Svalbard,” *Geoscientific Instrumentation, Methodes and Data Systems,* vol. in review, 2018.

ISBN: 978-82-575-1615-4
ISSN: 1894-6402

Norwegian University
of Life Sciences

Postboks 5003
NO-1432 Ås, Norway
+47 67 23 00 00
www.nmbu.no

104238 / ANDVORDGRAFISK.NO